JYVÄSKYLÄ STUDIES IN COMPUTING
230

Tuomas Turpeinen

Analysis of Microtomographic Images of Porous Heterogeneous Materials

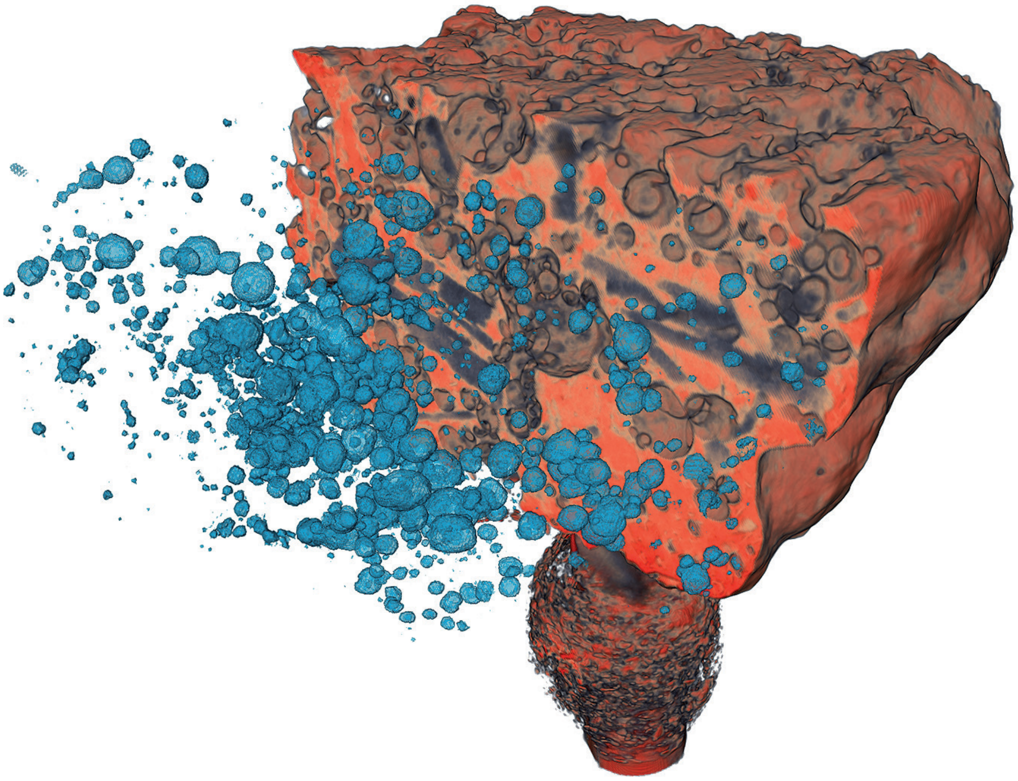

JYVÄSKYLÄN YLIOPISTO

JYVÄSKYLÄ STUDIES IN COMPUTING 230

Tuomas Turpeinen

Analysis of Microtomographic Images of Porous Heterogeneous Materials

Esitetään Jyväskylän yliopiston informaatioteknologian tiedekunnan suostumuksella
julkisesti tarkastettavaksi yliopiston Agora-rakennuksen Gamma-salissa
joulukuun 16. päivänä 2015 kello 12.

Academic dissertation to be publicly discussed, by permission of
the Faculty of Information Technology of the University of Jyväskylä,
in building Agora, Gamma hall, on December 16, 2015 at 12 o'clock noon.

UNIVERSITY OF JYVÄSKYLÄ

JYVÄSKYLÄ 2015

Analysis of Microtomographic Images of Porous Heterogeneous Materials

JYVÄSKYLÄ STUDIES IN COMPUTING 230

Tuomas Turpeinen

Analysis of Microtomographic Images of Porous Heterogeneous Materials

UNIVERSITY OF JYVÄSKYLÄ

JYVÄSKYLÄ 2015

Editors
Timo Männikkö
Department of Mathematical Information Technology, University of Jyväskylä
Pekka Olsbo, Ville Korkiakangas
Publishing Unit, University Library of Jyväskylä

URN:ISBN:978-951-39-6446-7
ISBN 978-951-39-6446-7 (PDF)

ISBN 978-951-39-6445-0 (nid.)
ISSN 1456-5390

Jyväskylä University Printing House, Jyväskylä 2015

ABSTRACT

Turpeinen, Tuomas
Analysis of microtomographic images of porous heterogeneous materials
Jyväskylä: University of Jyväskylä, 2015, 164 p.
(Jyväskylä Studies in Computing
ISSN 1456-5390; 230)
ISBN 978-951-39-6445-0 (nid.)
ISBN 978-951-39-6446-7 (PDF)
Finnish summary
Diss.

In this work, we study the phases of image processing chain of microtomographic imaging in order to obtain reliable results while optimizing the time spent on denoising and segmentation. We consider that the decisions made at the early phases of the processing chain are most important and the selection made there essentially determine the overall quality of imaging process. We also compare here various denoising method qualitatively, however, we think that the pure noise removal ability is not the only requirement for noise removal in microtomographic images. By proper denoising we can affect selection of segmentation methods and, thus, also the quality of the analysis. Additionally, at the end, we also review the image segmentation and analysis methods commonly used in microtomographic imaging.

Keywords: 3D image processing, X-ray tomography, denoising, segmentation, image analysis

Author
Tuomas Turpeinen
Department of Mathematical Information Technology
University of Jyväskylä
Finland

Supervisors
Professor Tommi Kärkkäinen
Department of Mathematical Information Technology
University of Jyväskylä
Finland

Professor Jussi Timonen
Department of Physics
University of Jyväskylä
Finland

Doctor Kirsi Valjus
Department of Mathematical Information Technology
University of Jyväskylä
Finland

Reviewers
Assistant Professor Tapio Pahikkala
Department of Information Technology
University of Turku
Finland

Professor Amir Averbuch
School of Computer Science
Tel Aviv University
Israel

Opponent
Professor Jussi Parkkinen
School of Computing
University of Eastern Finland, Joensuu Campus
Finland

ACKNOWLEDGEMENTS

The work reviewed in this thesis has been carried out during the years 2004-2015 in the Department of Physics and the Department of Mathematical Information Technology at the University of Jyväskylä. The financial support from the International Doctoral Programme in Bioproducts Technology (PaPSaT) and University of Jyväskylä is gratefully acknowledged.

First I would like to thank my supervisors Prof. Tommi Kärkkäinen, Prof. Jussi Timonen, and Dr. Kirsi Valjus for their excellent guidance during these years. I would like to express my deepest gratitude to Prof. Jussi Timonen, whose motivation and encouragement during the years had a significant effect on the progress. In addition, I would like to thank Prof. Tommi Kärkkäinen for his patient and inspiring attitude during this long and challenging project.

I would also like to thank my co-workers Jari Hyväluoma, Viivi Koivu, Lasse Miettinen, Arttu Miettinen, Keijo Mattila, Jarno Alaraudanjoki, Joni Parkkonen and Pekka Kekäläinen for their contribution to my work and for fruitful collaboration in all the projects we have had during these years. Special thanks are due to Markko Myllys and Axel Ekman for their help on details of physics in this work and for Einari Periäinen for various technical support.

I am grateful to the whole staff of the department of physics for the pleasant working atmosphere. Especially the current and former people (and frequent visitors) of FL348. The good times with our mölkky sessions and MC $\frac{E}{C}$ have all been important parts of my work well-being.

Also, I want to thank all my friends for their empathy and understanding during this project. This is to everyone who wonders if I'm writing about them. I am.

Finally, I thank my parents and my sister for their support and encouragement.

ACRONYMS

2D	Two-dimensional
3D	Three-dimensional
AD	Anisotropic diffusion
BF	Bilateral filter
CCD	Charge coupled device
CPU	Central processing unit
(μ)CT	(Micro) Computed tomography
DCT	Discrete cosine transform
DT	Distance transform
EDT	Euclidean distance transform
ESRF	European synchrotron radiation facility
EM	Expectation maximization
EW	Edwards-Wilkinson equation
(F)FT	(Fast) Fourier transform
FBP	Filtered back projection
GPU	Graphics processing unit
GMM	Gaussian mixture model
LB	Lattice-Boltzmann
MH	Mardia and Hainsworth
MIP	Mercury intrusion porosimetry
MS	Mean shift
MRI	Magnetic resonance imaging
PDE	Partial differential equation
Pixel	A picture element
RAM	Random access memory
SDCT	Sliding discrete cosine transform
SPH	Smoothed particle hydrodynamics
SVD	Singular value decomposition
VaWe	Variance weighted mean filter
Voxel	Volumetric pixel (3D pixel)
XμCT	X-ray micro computed tomography

NOTATIONS

∇a	Gradient of image a
$\Delta^{x}_{[h1,h2]} a[\mathbf{v}]$	Finite difference approximation of partial derivative along x-axis for image a at voxel $\mathbf{v}$. h_1 and h_2 denote the spacing for forward and backward steps, respectively.
$\|\| \cdot \|\|_p$	l_p norm
$a[i,j,k]$	Value of image a at pixel index i,j,k. Sometimes the $a[\mathbf{v}]$ -form is used to simplify the notation, $\mathbf{v} = [i,j,k]$.
$a(x,y,z)$	Value of an image a at real valued coordinate x,y,z.
$\text{Ave}(V)$	Mean value of pixels in voxel set V
$a'[\mathbf{v}]$	Discrete derivative of image a
$B_{\text{out}}(V)/B_{\text{out}}(V)$	Inner / outer border of voxel set V. See equation (7) and equation (8) for more details.
$\mathcal{C}_n[\mathbf{v}]$	n-connected neighbours of voxel $\mathbf{v}$ in 3D; n is usually 6, 18 or 26.
$\mathcal{N}^{p}_{r}[\mathbf{v}]$	Voxel neighbourhood of $\mathbf{v}$, r is the radius and p defines the distance norm. The simplified notion $\mathcal{N}[\mathbf{v}]$ can also be used if radius and norm are readily fixed.
$T(a,\tau)$	Threshold operation performed for image a with threshold value τ resulting a binary image.
$T_t(a)$	Translation of image a by vector t
$\text{Var}(V)$	Variance of pixels in voxel set V
$\mathbf{v}$,$\mathbf{q}$	Notations used of a single voxel. A subscript i,j or k can be used to indicate pixel indexes and x,y or z for real valued coordinates
V	Notation used of a set of voxels.

LIST OF FIGURES

LIST OF TABLES

CONTENTS

1 INTRODUCTION

Computerized tomography (CT) is a method for obtaining digitalized, three dimensional (3D) representation of, virtually, any kind of a sample. The word *tomo* comes from the Greek word meaning “cut” or “section,” and *graphy* comes from the Greek word meaning “to write.” Tomography can be considered imaging by sectioning. The method produces a collection of “cross-sectional” images with certain thicknesses through the given sample, thus, forming a digital 3D representation of the sample. Microtomography (μCT) is a version of CT in which the detail detectability is in the range of a micron. In μCT, X-rays are the most common illumination source which is why the method is identified as X-ray microtomography (XμCT).

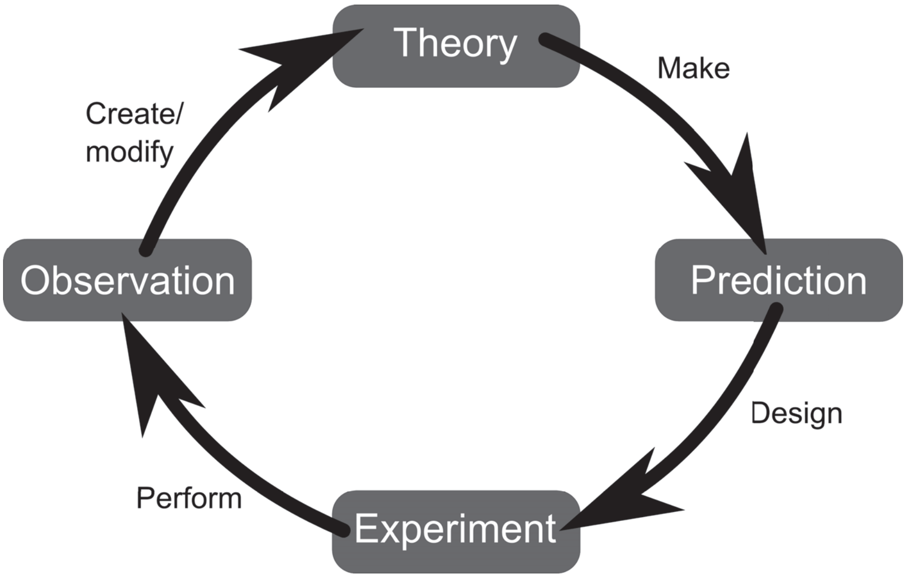

FIGURE 1 A schematic image of Scientific model from Encyclopædia Britannica [102].

For scientists, XμCT offers a non-destructive method to study matter and observe various material related phenomena. figure 1 explains roughly how the scientific process works: theories are proven by making observations either on natural phenomena or by performing planned experiments. XμCT is an excellent tool for making these observations. XμCT allows one to obtain an accurate geometrical model of a large range of materials, exposing not only the shape but also the internal material composition of the sample in a non-destructive manner. This makes it possible to look inside materials that are non-reachable due to their value or fragile structure. This tools also makes it possible to look inside materials that have a tendency to suffer from manipulation with mechanical tools. This is an exciting possibility for material researchers, opening a whole new field to explore. The method allows researchers, for example, to match the physical models with results observed from the 3D geometry of the real sample, to find new structural characteristics for a material, and to design experiments to validate predictions in the 3D behaviour of the material.

However, as with any complicated observation method, the XμCT imaging process requires quite an amount of work. The device itself needs periodical maintenance as parts wear out or loose their calibration. The imaging procedure produces a huge amount of data and the storage systems need to be organized properly. Preparing samples and mounting them on a sample holder firmly can be a laborious task. Finally, image processing is often the most complicated task. After the image has been obtained, it consists of a data matrix containing numbers. To transform any structural information into a numerical form, some sort of a processing need to be done. For example, an image of cheese can be visualized and seen by the eye, but if information about the amount of holes in the cheese is required it has to be determined either manually or computationally. It is often not feasible to complete manual work in a reasonable time and proper image processing tools need to be developed to cope with the task. In essence, tomography is a tool used by people interested in properties of material or objects, yet the skills required to comprehensively use the device requires an understanding of computers, mechanics, X-ray physics, and image processing. Currently, the basic behaviour of X-rays (found in 1896 [197]) is well established knowledge, but computerized image processing is a much newer field (Charge-coupled device (CCD) invented in 1969 [35]) that is constantly being developed as computers themselves develop.

1.1 Background

X-rays were discovered by Wilhelm Röntgen in 1896 [197]. William Coolidge designed the modern X-ray tube in 1913 [48]. The mathematical foundation of reconstructing a 3D image from a collection of projection images around the sample was developed in 1917 by Johann Radon [189]. In 1963, Allan McLeod Cormack first discussed the use of X-ray tomography in practice [49], and in the early 1970s, Godfrey Hounsfield developed the first commercial CT system for medical scanning [108]. Takuso Sato [207] developed the first laboratory based micro-tomographic system in 1981 with a voxel size of 6.1 μm. Similarly, high intensity microfocus X-ray sources were developed, achieving smaller spot sizes and high X-ray flux.

Detecting the X-rays long relayed on photographic plates that were sensitive to X-rays [232]. The development of the digital semiconductor made it possible to use image plates to record digital X-ray shadowgrams. These detectors were large, had pixel sizes of 10 - 100 μm and were mostly used on medical devices [61]. Within XμCT, the imaging area was much smaller and, thus, image plate detectors were not suitable. By the end of the 1980s, the development of CCD detectors allowed them to be utilized in tomographic imaging, enabling low-cost and high efficiency detection of X-rays with small pixel size.

Finally in the beginning of 1990, scientific CT devices for scanning small objects (2–50 mm) at high resolution (1–10 μm) (i.e., μCT scanners) first became available with applications to bone [192]. In 1994, with the introduction of the first commercially available bone μCT scanner [192, 200], this technique became a standard in bone research. At the end of 1990, a new type of X-ray tomography device was introduced (Skyscan, today known as Bruker microCT, claims to be the manufacturer of the first commercial microtomograph, build in 1996 [37]). These new devices, capable of obtaining images of small samples with resolutions less than 1 μm in all dimensions, marked the era of XμCT. XμCT made it possible to digitally analyse the original complex 3D structure of many small samples that were non-reachable in the past. These devices were developed for material research and introduced new possibilities to researchers. Since the development of the first commercial scanners the evolution of technology has concentrated on improving the resolution (with the best resolution being close to 10 nm at the moment [93]), finding better X-ray sources, developing energy sensitive scanners, and generating better algorithms for imaging and image processing, the latter being driven by the rapid development in computing capabilities.

1.2 The Possibilities of XμCT

Tomographic imaging is primarily based on the reconstruction algorithm. The algorithm reconstructs the 3D image from a series of transmission images. The images are collected by illuminating the sample with radiation that partially attenuates the sample while travelling through it. The attenuation is different for the various materials in the sample, and that makes it possible to distinguish them from each other at the resulting image. Many types of radiation can be used, including X-rays, gamma rays [85], electrons [162], and ions [128] to mention a few. In this work, we use X-rays, which is the most conventional approach. The contrast between the materials is roughly obtained due to the X-ray attenuation caused by density differences in the material.

The spatial resolution of the system is determined by the scanning geometry (spot size and geometrical magnification) and the detector resolution. In medical X-ray tomography, the voxels are non-uniform in size, with spatial resolution around 0.5–1 mm in x-y -plane. With the XμCT devices, the resolution is typically same in all dimensions, which makes these images very usable for material research, allowing one to easily analyse the 3D structure of the sample. Moreno-Atanasia [167] identify the following main limitations of the method:

- Spatial resolution and sample size: Often, the highest resolution is obtained only at the expense of a small sample size or a small scanned area.

- Temporal resolution: XμCT requires that the structure of the sample remains unchanged during the scan (which can last anywhere from a few minutes to many hours with laboratory devices). This limits XμCT's ability to look at fast dynamic behaviour. However, with synchrotron X-ray sources, very quick scans can be completed.

- Image contrast: XμCT distinguishes components of different materials by the difference in their absorption coefficient. If a sample contains components of similar attenuation (absorption) coefficients, XμCT cannot distinguish the components from one others.

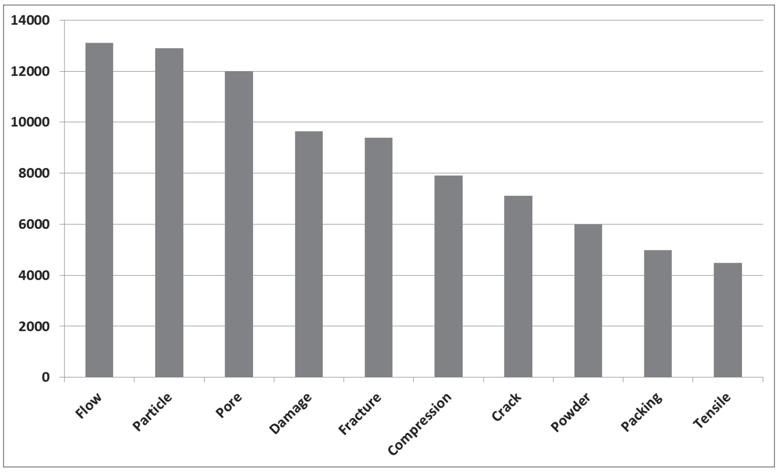

FIGURE 2 Number of publications on various structural types or analysed properties (top 10) analysed by μCT. Note that the same publication can be in more than one bar. The information was obtained from Google Scholar by using search phrases *microtomography* and *μCT*, as well as the keyword. (30.10.2015). The list of the keywords was obtained from the previous analyses of μCT usage.

XμCT can be utilized in research in many ways. It is often sufficient to to look at the images and visually explore the internal details. For example, in fault analysis, it is enough to visually inspect the samples and to use projection to determine the results. On the other hand, computational image analysis allows for the full potential the material analysis to be reached. Quantitative microtomography [208] combines XμCT with quantitative 3D image analysis. The aim of quantitative microtomography is to expand the analysis of tomographic images beyond simple visualization. This allows for detailed analysis of particle structures, orientations, true 3D connectivity, etc. figure 2 lists some of popular material types analysed in XμCT, the figure also shoes on what kind of analyses can be done within the method.

There are several phases when performing a complete XμCT image analysis for an arbitrary sample. See figure 3 for schematic view.
To clarify the terms the scheme can be thought of as follows ([271]):

- Image acquisition: Sample in → image out

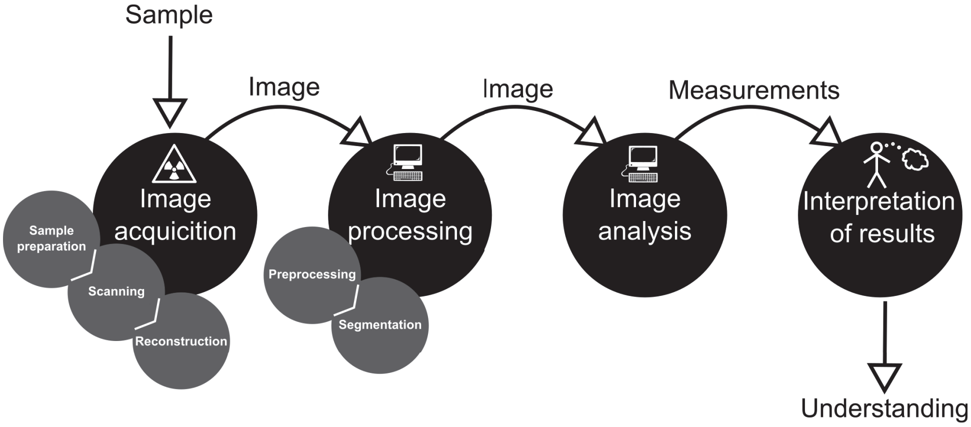

FIGURE 3 XμCT analysis process flow.

- Image processing: Image in → image out
- Image analysis: Image in → measurements out
- Image interpretation: Measurements in → understanding out

The XμCT image analysis continuum starts with image acquisition. Image acquisition part involves the sample preparation, imaging and reconstruction. The success of image acquisition has a significant impact on the effort required and the quality of the analysis. As it will be later shown, an optimal quality image will provide the most reliable results. The amount of work required depends on the sample; for some materials, it is easy to get contrast, but in the case that the material components are very similar in their density or their detail size is close to the spatial resolution, it can require a long imaging time to get adequate contrast. In some cases, the sample itself can be manipulated to enhance the contrast.

In the image processing phase, we modify the image into a form suitable for extracting information from it. At the preprocessing part we convert the data into form where it is most convenient to work with. We reduce the size of the data and remove the noise and other artefacts if possible. Reduction of the noise and the artefacts are one of the biggest challenges in the process. The imaging devices often produce some sort of artefacts and noise to the image. The noise causes the gray value ranges of different materials to overlap and thus hinders further processing. By efficient denoising methods the processing can be eased.

The properties analysed are often related to certain components in the sample material. To be able to analyse those structures digitally we need to differentiate those components from each other at the image. Image segmentation refers to a process where the interesting components of the image are separated. It is splitting the image into structurally meaningful parts that are analysed further at the next step. An example of segmentation is separation of paper fibres from paper coating as shown in figure 4. The result of a segmentation process is called a labelled image, or if only two components are differentiated from each other a binary image. In binary/labelled image each voxel of the image is given an individual label that refers to the component the voxel is assigned to. Binary/labelled

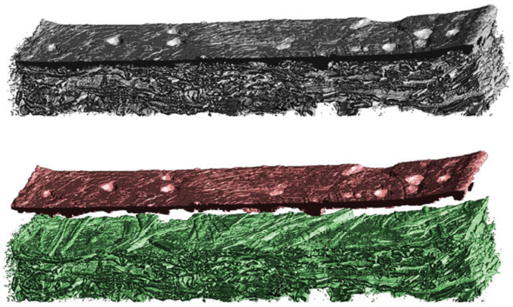

FIGURE 4 Visualisation of base paper and paper coating separated from each other for further analysis.

images have certain benefits that we don't have in gray value images; labelled image explicitly defines which voxels are inside the material we are interested in and where is the edge. This makes it possible to determine structural properties like size, volume, shape, center, orientation and distances for the object.

The challenge in segmentation is noise and artefacts. Wildenschild [260] lists three ways to handle the noise:

1. Noise reduction before binarisation
2. Morphological noise reduction from binarised image
3. Usage of some noise tolerant segmentation method

Option 1 is preferred over option 2 as the noise reduction of gray value image provides more possibilities than filtering the binary image [260]. Option 3 is also popular, but can complicate the segmentation algorithms (but also giving the possibility to use the gray values more effectively for the segmentation too). In practice, a combination of options 1 and 2 are most often used, as the denoising methods rarely can remove the noise perfectly. However, at the end, segmentation is a difficult and non-trivial task, and there is no single segmentation method that works on every image. Instead there is a variety of denoising and segmentation methods that work within certain image-related assumptions.

This entire process aims to improve understanding the sample properties. This means that numerical information is extracted from the image, which can then be interpreted within the given context. In the image analysis phase, the image data is converted into numerical results. For example, we can analyse the pore size distribution of a rock sample or the fibres orientation and connectivity of a paper or cardboard sample.

The last part of the continuum includes understanding the analysis results, and this is often manual work. The interpretation of analysis results needs to be done by a person that know the original problem we are observing with the XµCT (see figure 1). For example, we can consider the effect of the pore size distribution on the liquid transport property, or the effect of fibre contacts on the strength of a fibrous sample.

1.3 Literature

The first scientific papers discussing XμCT were published in the beginning of the 1980', and since then, the publication speed has steadily increased. The number of publications related to microtomography and image analysis started to increase as commercial microtomography devices become available. In figure 5, the number of publications related to tomography and image analysis are shown.

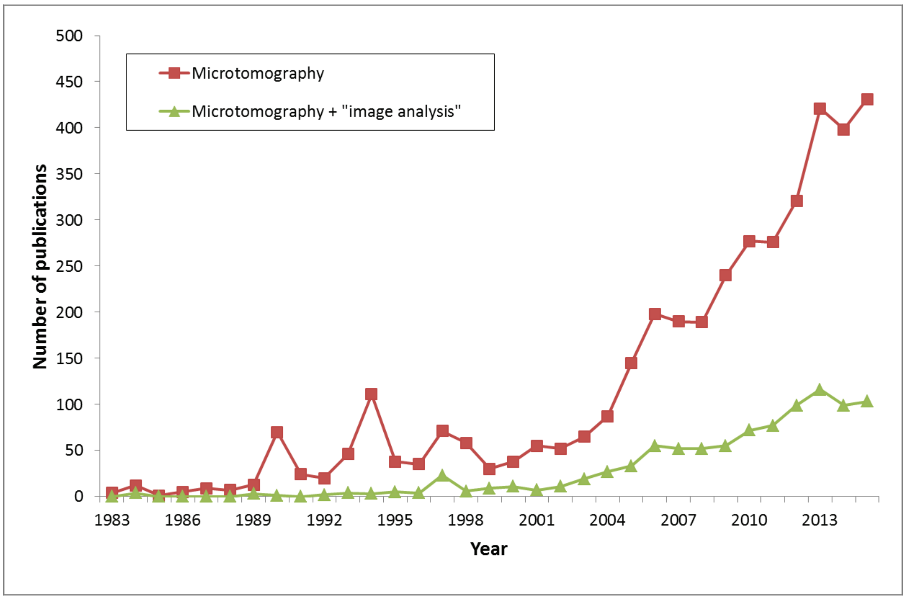

FIGURE 5 Number of publications on μCT obtained from ScienceDirect by searching for articles containing words *microtomography* or *μCT* (21.9.2015).

The articles about XμCT can be roughly divided into two categories: those that develop the imaging method and those that use imaging device for their applications. The researchers that develop the method are mostly mathematicians, physicists, or computer scientists, discussing the reconstruction, hardware, and image processing methods, respectively. figure 6 contains a list of the most frequently occurring materials and the number of publications related to those materials found in Google Scholar. As the figure shows, the range of materials suitable for XμCT analysis is wide and the method is used in many fields of science; biology and physics are the fields in which the method is most actively used. Some applications for XμCT analysis involve structural analysis of historical samples, such as insects in amber [131], rock and soil analysis [130], paper and paper making fabrics [243], bone [151], and fluid flow simulations with realistic complicated sample geometries [242]. For biologists, the method allows for the study of organs (usually ex vivo) with notably higher resolution than hospital CT devices (although the sample size is limited).

From a material science point of view, the method allows researchers to obtain 3D digitalization of most materials while leaving the material itself intact; the material is usable also for further studies. References [206] and [227] provide detailed information on material research using XμCT. The properties commonly analysed by XμCT are related to the structural properties of the material. The structure is often parametrized into numerical values (e.g., porosity, thickness, and tortuosity). These numerical values are usually compared with some measured behaviour of the sample material. The sample can also be manipulated (e.g., compressed, stretched, frozen, heated). The structural changes resulting from this manipulation can then be identified. A common analysis theme for material researchers is porosity and pore property analysis, as demonstrated in [251]. By inverting the notion of a pore into solid, we get particle analysis as demonstrated in references [74] and [247]. The properties commonly analysed from pore/particle samples are volume, surface area, orientation, connectivity number, shape, etc. Tortuosity and autocorrelation are often related to pore space measures [54, 187]. For biologists a typical material to analyse is bone (see [200, 174] for examples), which as dense material is very suitable for XμCT analysis. In bone research, properties that are typically analysed ([24, 89]) include tissue volume (TV), bone volume (BV), tissue surface area (TS), bone surface area (BS), BV/TV, BS/BV, BS/TV, trabecular bone thickness (Tb.Th = 2BV/BS), determined number per unit length (Tb.N) and preset separation (Tb.Sp = 1/(Tb.N-Tb.Th)). In addition, shape parameters are used to determine the plate/rod likeness of the trabecular elements [57]. For fibrous samples, the orientation, length and connectivity of the fibres are analysed [56]. For rigid samples, the material can be mechanically altered between the scans allowing for analysis of, e.g., the propagation of a crack [17, 137]. In [153] and [158], in situ tensile testing is combined with tomography to see how the material is deformed when subjected to tensile loading. In the food industry, microtomography offers a way to study end products in their true 3D form; for example, in [71] the structure of Chocolate of Modica was studied. In addition to structural analysis, microtomographic images are used as sample geometry for various kinds of simulations. For fluid flow simulation, the voxel data can be used as a simulation geometry as is or or by converting it into a vector format, this method has been used for various types of materials [31, 242, 139, 98]. The geometry can be used as a source data for finite element methods (FEM)/ discrete element method (DEM) simulations [235, 175]. A less published way of using μCT is analysis of historical samples; microtomography is a way to obtain a digital 3D representation of the historical samples without manipulating them using mechanical tools. Tafforeau et al. [231] have written a descriptive article about imaging historical samples. Solidification of metal is an example of a process that is very hard to follow with any other means; there are special XμCT devices capable of capturing a 3D image of a sample in few seconds making it possible to generate a 3D time series of such a process [97, 138]. Many industrial companies also make use of XμCT in their quality control and failure analysis processes.

1.4 Scientific Focus

This thesis will focus on image processing and numerical analysis of tomographic images. The main focus is on dealing with noise and other artefacts and on selecting the proper

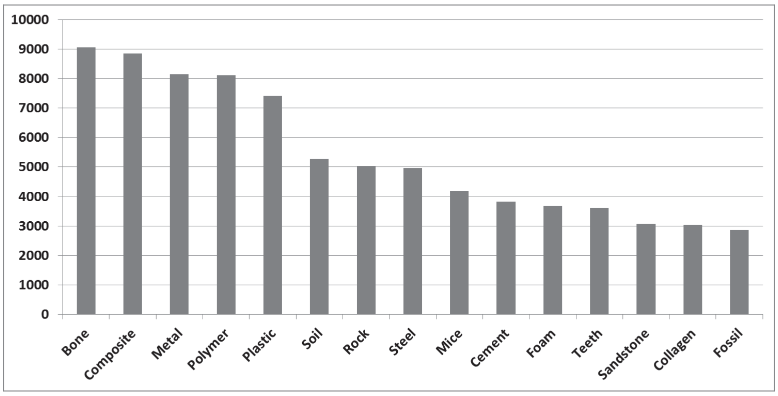

FIGURE 6 Number of publications on various materials (top 15) analysed by µCT. Note that the same publication can be in more than one bar. The information was obtained from Google Scholar by using search phrases *microtomography* and *µCT*, as well as the name of the material. (30.10.2015). The list of the materials was taken from the previous analyses of µCT usage.

tools for the denoising, segmentation, and analysis phases. In practice and after image acquisition, denoising and segmentation has been found to be the most critical parts in the analysis continuum. Due to the range of material and analysis problems, the algorithms here are quite general. We limit the methods discussed to analysis of porous heterogeneous materials according to their structural properties. The analysis methods used in this work tend to be easily assimilated and efficient to calculate but are still able to target the given problem efficiently. Most of the methods applied in this research have already been implemented in 2D image analysis; here we introduce them for 3D image analysis and provide examples of their potential use. Some of the connecting factors for the algorithms implemented during the research area as follows:

- Efficient memory consumption: Modern desktop computers can have memory in tens of gigabytes, which is sufficient for many image processing tasks including large images. However, the file size of a typical image is usually measured in gigabytes and certain algorithms require memory that is much greater than the size of the sample, causing certain limits on memory usage.

- It should be possible to perform the calculation on a modern desktop computer in a reasonable time. For certain problems, a computer clusters or supercomputer can be used, but such facilities are not available for everyone on a regular basis.

- The method needs to have a high degree of usability. As the analyses are usually performed by person who is not an expert on image processing, the method should be easy to understand and easy to use.

In addition, as with every imaging based system, the image quality is an important factor that impacts on the difficulty of image processing. To this end, it is important to know the physical background and the mechanical properties of the system, thus making it possible to minimize the system based artefacts.

To reflect the authors contributions for XμCT in figure 3, we present the following list:

1. *Image acquisition:* As being not directly working on this field, publications on this subject have not been submitted. However, author has been actively using Skyscan 1172 device (starting 2005), Xradia MicroXCT-400 and Xradia NanoXCT100 (also maintenance, starting 2009). Author has also visited ESRF, id19, (several times) and Swiss light source for synchrotron XμCT imaging.
2. *Image processing* The author has been collaborating in following articles:
   (a) [240], author implemented methods on how to study the coating layer of a paper in 3D using XμCT, presented in 22nd coating symposium.
   (b) [217], (co-author) author implemented the denoising system applied to the rock analysis, presented in MRS Symposium in 2007
   (c) [121], (co-author) the author implemented a method for segmenting paper-making-fabrics from tomographic images taking into account the thickness of the yarns of the felt.
   (d) [122] (co-author) the author implemented a method for segmenting paper from tomographic images.
   (e) [242] the author implemented a method for denoising and segmenting fibre-based material from tomographic images. The liquid transport properties were also simulated in similar method than in [244].
   (f) [151] (co-author) the author implemented a method for separating the trabecular and cortical bone.
   (g) [129] (co-author) the author implemented a method for determining the surface of porous rock samples.
3. *Image analysis* The author has been collaborating in following articles:
   (a) [99] (co-author) The author implemented a system to obtain information on pore space that allows us to simulate mercury intrusion porosimetry process within the sample.
   (b) [244] The author further developed a system described in [99].
   (c) [119] (co-author) The author developed a method to 3D segment and to obtain geometrical information from individual pores and pore throats.
   (d) [164] (co-author) The author developed a 3D method to separate individual spherical metal particles from sintered sheet. These individual particles were further analysed to produce a simulation graph for thermal conductivity simulations.
   (e) [59] (co-author) The author implemented a method for measuring the distances through a fibrous sample.
   (f) [241] The author implemented a developed a method for detecting planar, tubular and spherical interfaces from discrete 3D images.

Despite the “sufficient” number of articles we considered monograph to provide a more complete view of the work done. In addition we consider that this kind of a work, that rounds-up the current state of the XμCT image processing, would be more useful for the XμCT community.

The work in this thesis has been carried out by the SoftStat group of the Department of Physics in the University of Jyväskylä. This group receives funding from industrial sources, as well as from academic projects. The group aims to use tomography in research of porous heterogeneous material. Porous heterogeneous material includes a large variety of material. The scope of the group is relatively wide in both material and scientific sense. "The author have been assigned to support the group with all image processing related problems. For this reason, this work does not concentrate on some certain subjects or materials, but instead presents various methods that are suitable for image processing challenges related to XμCT. However, the work is not comprehensive in terms of algorithm coverage and and many good image processing methods exist that are not mentioned in this work. We have aimed here to study methods that are essential for XμCT imaging.

1.5 Structure of the work

The physical backgrounds of the image acquisition, artefacts, reconstruction, and visualization are given in chapter 2. Image processing definitions and a collection of general purpose algorithms are given in chapter 3. In chapter 4, several commonly used and new (for XμCT) denoising methods are introduced, and compared in terms of denoising quality, processing time, and usability. In chapter 5 few commonly used segmentation algorithms, as well as one new algorithm, are described and studied. The results of the denoising chapter are also considered together with the segmentation. Chapter 6 describes a list of analysis methods used to analyse the typical problems with porous heterogeneous materials. Finally chapter 7 provides the conclusion of the work.

2 ACQUIRING XμCT IMAGES

In this chapter the physical background of XμCT systems is formed and the image acquisition system and its artefact are introduced. CT imaging is based on a computational reconstruction of the local attenuation coefficients of a sample from a series of 2D transmission images collected by measuring the attenuation of a radiation (e.g. X-rays) travelling through the sample. A rotational series of transmission images (see figure 7), of the sample is collected using a special device (see section 2.4) and a mathematical reconstruction algorithm (see section 2.5) is used to calculate the 3D attenuation coefficient map (such that the conditions given by the transmission information are fulfilled). The series of transmission images is obtained by exposing the sample with radiation from various angles (typically) around the sample's z-axis as in figure 7 and measuring the attenuation map at each position. A 180 or 360 degrees rotation is used with small rotational step. Tomogram, or tomographic scanner, is a device designed for obtaining such a set of transmission images.

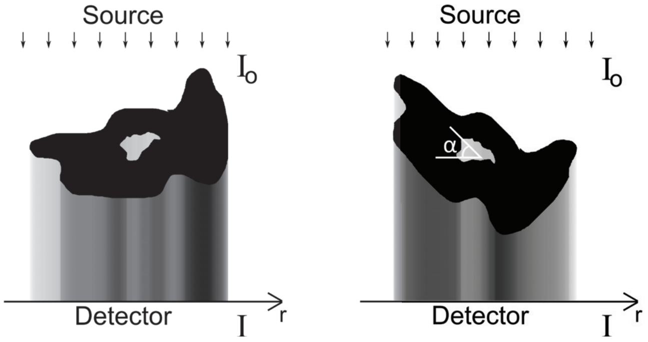

FIGURE 7 The principle of collecting XμCT projection images. The source emits X-rays that traverse through the sample, and the projected intensity is measured. The process is repeated for multiple (known) sample rotation angles. These data are computationally reconstructed to a digital representation of the 3D attenuation coefficients.

The end product of an X-ray CT scan is a 3D data matrix containing the X-ray attenuation coefficients inside the reconstructable volume of the sample (volume of interest, VOI). The X-ray attenuation coefficient is dependent on the atomic number of a sample. The atomic number is roughly equivalent to the density of a sample.

2.1 X-rays

X-rays are electromagnetic waves having a wavelength in range of 10 to 0.01 nanometres. They are generated by manipulating a beam of high energy charged particles, such as electrons, so that it bends or collides with a metal target. The energy E of an X-ray is determined by its wavelength λ, being in range from 120 eV to 120 keV as determined by the equation:

$$E = \frac{hc}{\lambda},$$

where h is Planck's constant and c is the speed of light.

There are few terms commonly used in X-ray terminology. *Photon flux* is the amount of photons passing through a given area perpendicular to the direction of radiation in a given unit time: $\phi = N/(A \cdot t)$, where N is number of photons, A is the surface area of detector and t is the detection time. *Intensity* is the sum of energy of the photons passing through a given area perpendicular to the direction of radiation in a given unit time: $I = \sum_{i=0}^{N} \frac{hc}{\lambda_i} / (A \cdot t)$, where λ_i is the wavelength of the ith photon. *Brilliance* is a term used for measure of the flux and directionality of an X-ray beam, determining the smallest spot upon which the X-ray beam can be focused: $b = \frac{\phi}{\alpha}$, where α is the angular divergence of the X-ray beam.

The energy of the X-rays defines what kind and how thick it penetrates, and therefore, the characteristics of the X-ray source are an important factor in X-ray imaging. X-rays in the energy range of 0.12 to 12 keV are considered as soft X-rays, suitable for imaging light and small objects. Especially so-called water window, 0.28 - 0.53 keV, gives optimal conditions for imaging biological specimens. Water is transparent for these X-rays, while objects containing nitrogen and carbon are attenuating well. Hard X-rays are in the range of about 12 to 120 keV and have good penetrating properties in dense materials.

X-ray generation

There are two main techniques for generating the X-rays: a anode-cathode type of systems or synchrotron [48]. Anode-cathode systems are cheap, compact in size and easy to fit into laboratory scale XμCT devices. Synchrotrons are large-scale facilities producing highly tunable and high flux X-ray beams allowing better contrast and fast scans.

In anode-cathode systems, the X-rays are produced by heating a filament with an electric current; see figure 8. The filament emits thermal electrons that are accelerated to the anode by a voltage potential difference. When electrons hit the anode, X-rays are generated. Two processes create the X-rays: X-ray fluorescence happens when an electron knocks out an electron from the inner electron shell of a metal atom. Electrons from higher energy levels fill the vacancy of the lower level and emit X-rays.

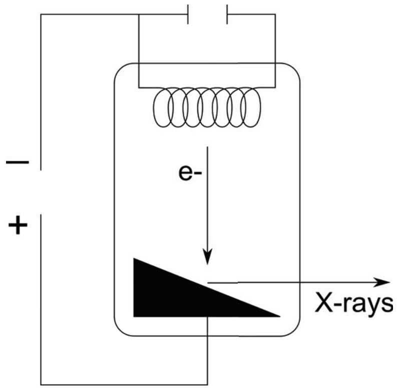

FIGURE 8 The principle of an X-ray tube. The filament is heated to make it emit electrons. A high voltage accelerates the electrons to the anode that emits X-rays.

The X-rays produced by fluorescence have few discrete energies depending on the target material and, therefore, generates so-called characteristic peaks to the emission spectrum. Bremsstrahlung radiation is produced by scatter of the electrons due to strong electric fields near atom nuclei. The Bremsstrahlung spectrum is continuous with a sharp cut-off at low wavelength. The overall resulting spectrum is a sum of the continuous Bremsstrahlung spectrum and the characteristic peaks caused by the fluorescence of the anode metal. See figure 9 for a schematic illustration of X-ray output of an X-ray tube.

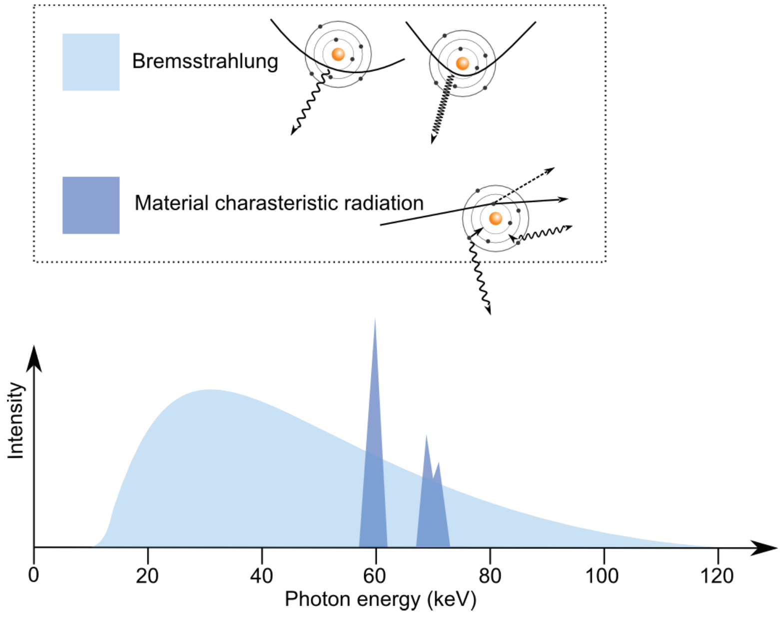

FIGURE 9 The output of an X-ray tubes is a continuous spectrum with characteristic peaks defined by the target material.

An X-ray tube is a typical anode-cathode system. An X-ray tube is a vacuum tube that uses a high voltage to accelerate electrons from a hot cathode to collide with a target (anode). The target material can be, e.q, tungsten, rhenium tungsten alloy or copper. The maximum X-ray energy of an X-ray tube is limited by its acceleration voltage; a tube with a 100 kV acceleration voltage produces X-rays with maximum energy of 100 keV. The efficiency of an X-ray tube is low; only about 1 percent of energy is converted into X-rays [171], as most of the input energy is distributed as heat. X-ray tubes are typically used in laboratories producing X-rays commonly in the range of 10–200 keV (although systems capable of producing X-ray in energy of 800keV exists). There are two basic types of X-ray tubes used in XµCT systems, namely solid anode and metal-jet-anode [88] microfocus X-ray tubes. Metal-jet-anode micro focus X-ray tubes are currently the state-of-the-art X-ray tubes providing the highest intensity (30-60W) with high spot quality (e.q. stability, shape). The focal *spot size* (the diameter of the area on the anode surface, which receives the beam of electrons from the cathode) for microfocus X-ray tubes is typically in range of 5-20 µm. Also, high intensity microfocus rotating anode X-ray generators are being used in some nanoCT systems. These provide a very high intensity (1-2 kW) for laboratory scale devices while the spot size is larger (around 100 µm) [227].

Particle accelerators, such as synchrotron, can also be used to generate radiation. Synchrotron consists of a particle accelerator and of a (large) electron storage ring. The electrons are first accelerated to almost the speed of light at the accelerator part. The electron beam is then injected into the storage ring where bending magnets are used to turn the electrons into a round trajectory. The ring is actually a polygon and at each corner bending magnets or wigglers or undulators are used to rotate the electron beam. While the electrons turn they emit X-rays. Beam-lines are placed at the corners of the synchrotron to utilize the X-ray radiation in various applications like X-ray imaging. Before the experimental end station the beam is manipulated using a collection of optical elements such as slits, attenuators, monochromators and mirrors to shape the physical beam and its spectrum into the desired shape and energy. Synchrotron radiation is an analogue to Bremsstrahlung, differing in that the force which accelerates the electron is a macroscopic (large-scale) magnetic field. The synchrotron radiation has a wide spectrum, high intensity (many orders of magnitude more than with X-ray tubes; see [84] for information of typical microfocus X-ray tubes), excellent collimation and linear polarization. The high intensity makes it possible to use a monochromator to select only a narrow wavelength range yet still have significantly more energy than an X-ray tube. A synchrotron source like the ESRF has a brilliance that is more than 10^9 times higher than a laboratory source. The high intensity of the synchrotron beam allows faster scanning times. The high intensity allows faster scanning times, the fastest less than few seconds. This makes it possible to have almost real-time imaging. However, the X-rays interact with the material by moving the electrons inside it and, thus, possibly causing radiation damage [46] if intensity is very high.

Properties of X-ray tubes

X-ray tubes are common XµCT X-ray sources. They are cheap and easy to obtain, but have few characteristics that make them more challenging to use than synchrotron radiation.

Figure 10 shows an example of an X-ray spectrum of an X-ray tube with various

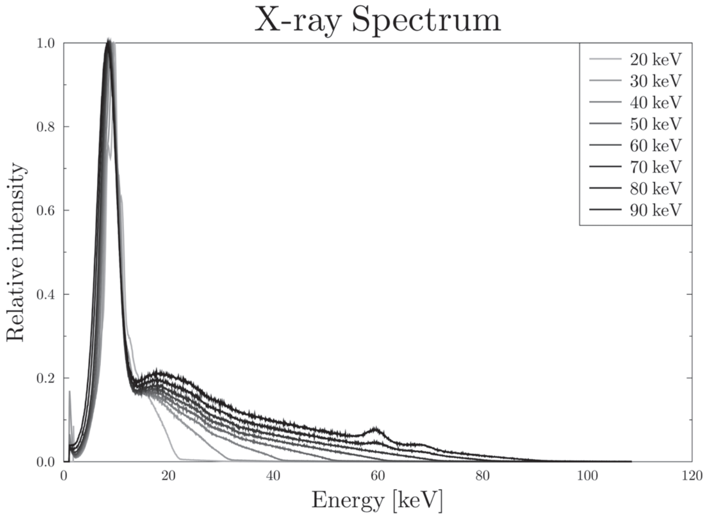

FIGURE 10 Spectrum of an X-ray tube at the function of acceleration voltage. Obtained with Amptek XR-100T-CdTe spectrometer.

acceleration voltages. At the lower energies, only the main characteristic peak is visible, and at the high energy smaller peaks appear. Due to the low intensity and high divergence of an X-ray tube monochromators are usually not applicable. With X-ray tubes, filters are used to shape the X-ray spectrum [15]. Filters can be made of different materials, like aluminium, glass, copper and plastic, and at varying thicknesses. The purpose of the filter is to cut down the low energy photons that have virtually no chance of penetrating the sample, thus sharpening the spectrum. This reduces certain artefacts from the final reconstructions.

The size of the spot is the main factor reducing the resolution (detail detectability) of an X-ray tube system causing blurring of the 2D projection images. A common microfocus X-ray tube has a spot size of around 5 μm. If we have a sample at a distance of d_{SS} from the source with focal spot size of h_{FS} and detector at a distance of d_{SD} from the sample the size of the half shadow h_{HS} is:

$$h_{\mathrm{HS}} = h_{\mathrm{FS}} \frac{d_{\mathrm{SD}}}{d_{\mathrm{SS}}}; \tag{1}$$

see figure 11. The spot size and location is not constant but depends on the both the power and temperature of the source [225, 72]. In addition, the spot has an intensity profile (see ref. [22]) due to X-ray tube structure.

The intensity profile of the X-ray spot also varies. The intensity profile might change shape when the source warms up or when the parameters of the X-ray beam are changed.

Thus we can see that the factors affecting the final point spread function of the image are the spot size, the power of the X-ray source and the drifting of the spot. The

XμCT scanner manufacturers recommend a certain warm-up time for the scanners before to start the scan in order to stabilize the beam (in addition to the normal warm-up time recommended by X-ray source manufacturers). Additionally, when the X-ray source is turned on, it produces a lot of heat that causes the parts of the scanner to expand, and this expansion should be allowed to stabilize as well.

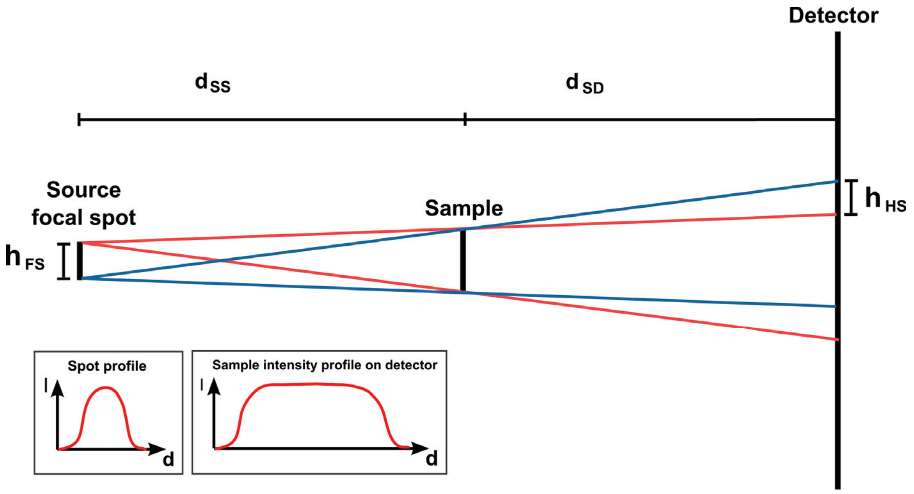

FIGURE 11 The half shadow effect caused by the limited spot size of an X-ray tube based source. In addition to geometrical lack of sharpness the spot has a profile that will blur the final image.

2.2 X-ray interaction with material

X-ray imaging is due to the fact that X-rays *attenuate* when they travel through a material. The transmission images record the attenuation into a form of 2D attenuation maps. The attenuation is caused mainly by photoelectronic absorption and Compton scattering; see figure 12. For single wavelength X-rays the attenuation can be described by Beer-Lambert law:

$$I = I_0 \mathrm{e}^{-\mu x}, \tag{2}$$

and for polychromatic beam the equation (2) becomes

$$I = \int I_0(E) \mathrm{e}^{-\mu(E) x} dE, \tag{3}$$

where I is the transmitted X-ray intensity, I_0 is the initial X-ray intensity, μ linear attenuation coefficient and x is the thickness of the material. In equation (3), E describes the energy and the integral is calculated over the given spectrum. Coefficient μ correlates with the material density and thus the overall transmitted X-ray intensity depends on material thickness and density. Often the linear attenuation coefficient is normalized with the density of the material resulting a mass attenuation coefficient $\frac{\mu}{\rho}$. The attenuation function becomes $\frac{I}{I_0} = e^{[\frac{-\mu}{\rho} mx]}$, where mx is the mass thickness of the material (i.e. thickness multiplied by density). The mass attenuation coefficient is energy-dependent and is determined individually for each material. See figure 13 for an example of a linear attenuation coefficient graph. This coefficient graph can be used to find an optimal beam energy if the material and thickness is known. Then equation (2) can be written as:

$$\frac{\mu}{\rho} = -\frac{ln\frac{I}{I_0}}{x}.$$

Within this equation, the mass attenuation coefficient can be determined for the desired attenuation factor and the corresponding beam energy can be read from the coefficient graph.

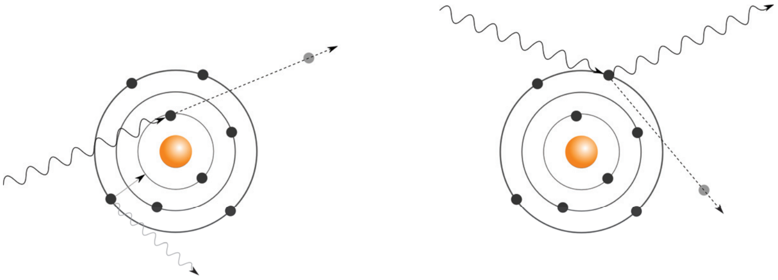

FIGURE 12 Two attenuation mechanisms of X-ray photon. On the left photoelectronic absorption (photons are removed from the beam) and on the right Compton scattering (the direction of the photons is changed).

For mixtures and compounds the mass attenuation coefficient is determined as

$$\frac{\mu}{\rho} = \Sigma_i w_i \cdot (\frac{\mu}{\rho})_i,$$

where, w_i is the fraction by weight of the ith atomic constituent and $(\frac{\mu}{\rho})_i$ is the corresponding mass attenuation coefficient.

The wave-like behaviour of X-rays cause *Rayleigh scattering*, resulting a phase shift to the X-ray waves. When X-rays travel through the material the interaction causes a phase-shift in the X-ray waves according to the material's refractive index. This also means small angular deflection between the interfaces. The probability for the phase shift to happen is much higher than that for absorption, which makes it much more sensitive to the sample structure.

2.3 X-ray imaging

In XμCT Charge-Coupled Device (CCD) detectors are used to record the shadowgrams. CCDs themselves are, in principle, able to detect low energy X-rays, but are sensitive to radiation and may suffer damage if exposed to direct X-ray beams [232]. *Scintillators*,

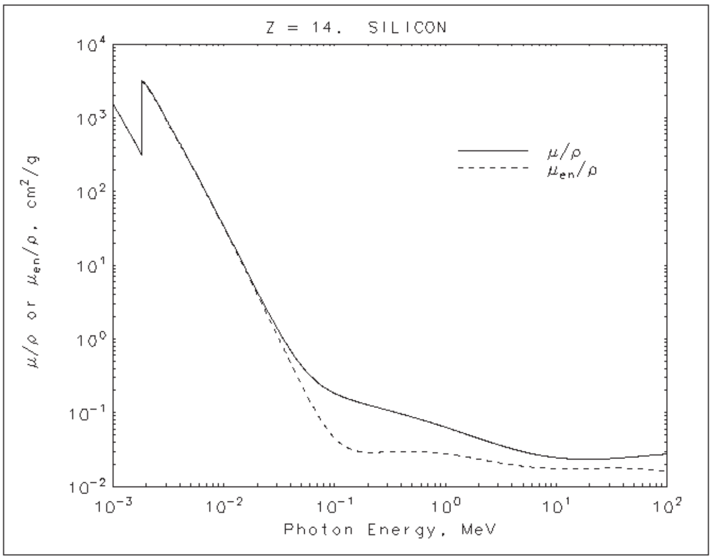

FIGURE 13 X-ray attenuation coefficient for silicon. Obtained from NIST database (http://physics.nist.gov/PhysRefData/XrayMassCoef/ElemTab/z14.html).

devices that convert X-rays into visible light, are used when recording the shadowgrams using normal CCDs. Scintillators also provide protection against radiation damage for the CCD. The light can be transferred to camera using mirror systems or fibre optic bundles.

The scintillators are plates made of material that is sensitive to X-rays. There are many types and materials used in scintillators [227] depending on requirements. Most common scintillator materials in XμCT are, according to ref [227], inorganic crystals such as NaI(Tl) (sodium iodide doped with thallium), CsI(Tl), CsI(Na) and CsI(pure). But a wide range of materials can be used depending on needs. The scintillator and CCD camera are coupled together using some kind of optical system to allow the image to be scaled to the size of the CCD chip. A few types of geometries used [227] are shown in figure 14.

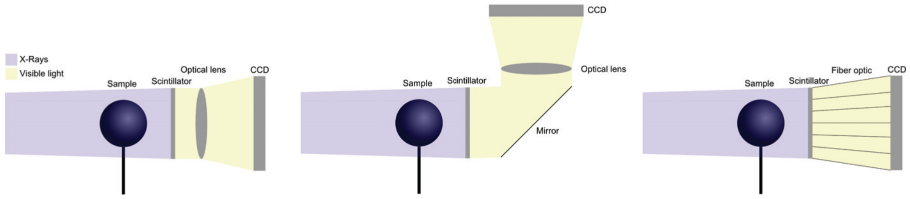

FIGURE 14 Scintillator-optics-CCD geometries used in XμCT systems. The system on the right and on the left is often used in laboratory scale system. In synchrotron laboratories more protection for the CCD chip is required and the system in the center is common.

CCDs used in XμCT are usually 12-16 bit devices capable of recording one channel (gray-scale) images. CCD chips are sensitive to photons and have almost a linear sensitivity [26]. The CCD chip itself consists of millions of small picture elements, pixels or bins, that respond to photons by storing a tiny charge of electricity. This charge in a pixel is proportional to the number of photons that struct into that pixel during the exposure and can be read by shifting the charges toward one edge and then occupying an analogue to digital converter to transform the charge information into a number. Before the voltage is read it is usually pre-amplified.

CCD Noise

As with all analogue to digital converters, CCDs present noise to signal. Healey [87] describes the following model for a single pixel recorded using a CCD camera:

$$a = g(i + N_D + N_P + N_R) + N_Q,$$

where a is the resulting image, i is the true intensity and the noise signals are following [26, 263]:

1. N_D (dark noise) is due to the thermal properties of the CCD. Dark current occurs on a CCD all the time, generating electrons into pixels. The dark current can be cleared before the exposure, but it will still generate during the exposure. The rate of the generation is dependent upon the device temperature and follows Poisson statistics. Cooling the device reduces the thermal noise. Some of this noise can be reduced by subtracting a so-called dark frame. The dark frame is an average of multiple exposures with same exposure time as the image was taken, but with no light allowed to come to the CCD.

2. N_P (photon noise) is due to the statistical variations of arrival rate of the photons. The photon counting happening in a CCD is fundamentally a Poisson process, meaning that the standard deviation of the noise is equal to the square root of the amount of photons collected by a CCD bin.

3. N_R (readout noise) is a combination of many technology-related noise sources of the CCD-chip itself. This noise is independent of exposure time and can not be removed via calibration. This noise has a Gaussian distribution.

4. N_Q (quantization noise) is caused by the complicated electronic system used to read and process the values from the CCD pixels. The sources are many and they are often uncorrelated and random. Also periodic noise can occur. In high quality cameras the off-chip noise is minimized.

In addition, there might exist variance in pixel sensitivity, the optics might cause artefacts like vignetting, dust particles may block the light for some of the pixels, the illumination might not be uniform etc. These artefacts could be reduced using flat field images. A flat field is an average of multiple exposures of the illuminated screen without the sample. An equation to the corrections is the following [26]:

$$I_c = \frac{(I_o - I_b)m}{(I_f - I_b)}, \tag{4}$$

where I_c is the calibrated image, I_o is the original non-calibrated image, I_b is the dark frame, I_f is the flat field image, and m is is the average of pixel values of $(I_f - I_b)$ (flat field corrected with dark frame). Note that the dark frame contains both the dark noise and read noise (bias frame). The dark frame is an image taken with no light allowed to the detector. Dark frames are usually taken automatically by the system; flat field images are taken manually.

To reduce the noise there are commonly two hardware-related options: to increase the exposure time or to average multiple shorter-exposure frames. In practice, with high quality CCD-cameras, both methods provide a similar result.

2.4 X μCT scanner

An XμCT scanner is a device for obtaining the transmission images needed for the reconstruction. The device consists of X-ray source, sample stage, and a detector, with either rotating sample stage or the X-ray source and the detector rotating around the sample.

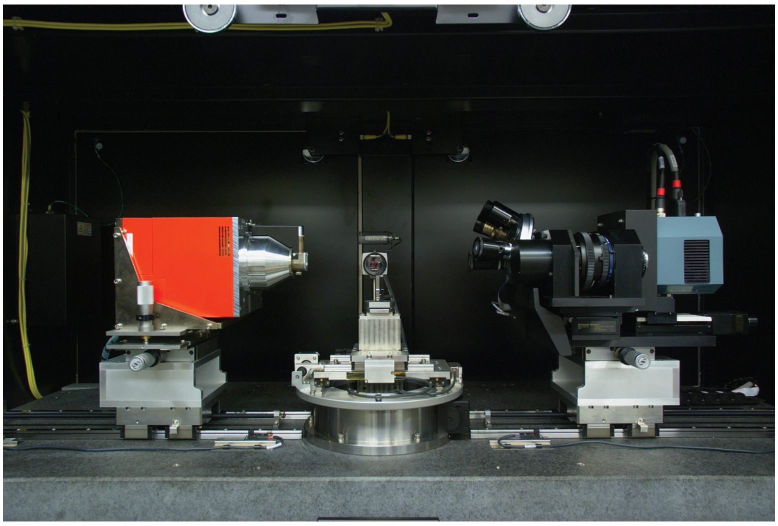

FIGURE 15 The interior of an XμCT scanner. On the left there is a X-ray source; on right there is a camera; in the middle there is a rotating sample stage. Behind the sample stage is a video camera to follow the progress of the scan.

figure 15 shows a typical construction of an XμCT device. The source is a microfocus X-ray tube; the sample stage rotates, and the camera is coupled with a scintillator and magnifying objectives. The space around the sample stage allows usage of different sample manipulation stages, e.g., humidity and compression testing stages. In some devices there can also be an automatic sample changing system to automatize the image acquisition in case multiple samples are imaged.

There are three main objects to be adjusted: X-ray tube (voltage and current), acquisition (exposure time, camera binning, rotation step) and geometry (distance of source, detector, objectives, etc.). Tube voltage is selected according to the sample material such that we get the recommended transmission (in practice transmission of 0.14-0.20 is desired [83] to obtain good image quality). The current effects to the X-ray intensity and should be maximized in order to have shorter exposure times. However, the current also affects the X-ray energy, causing the spot size to enlarge. The exposure time is chosen such that we get the photon count recommended by the scanner manufacturer (in range of 5% to 80% of CCD chip's maximum count). The rotation step is selected to suit the desired scanning time, a theoretical value is $\frac{\pi}{2} \cdot$ ccd-width, which fulfils the condition that one rotation step causes worst case of one pixel difference at the edge of the VOI in 3D. The rotation range is usually a half circle (+cone angle [188]). But sometimes certain artefacts can be reduced if full rotation is used. The optical magnification of a cone beam system is determined by the location of the sample in respect to the focal spot and the detector panel. Naturally the parts of the device need to be calibrated such that all the parts lie on the same optical axis and the rotation axis is exactly perpendicular to the optical axis as shown in figure 16.

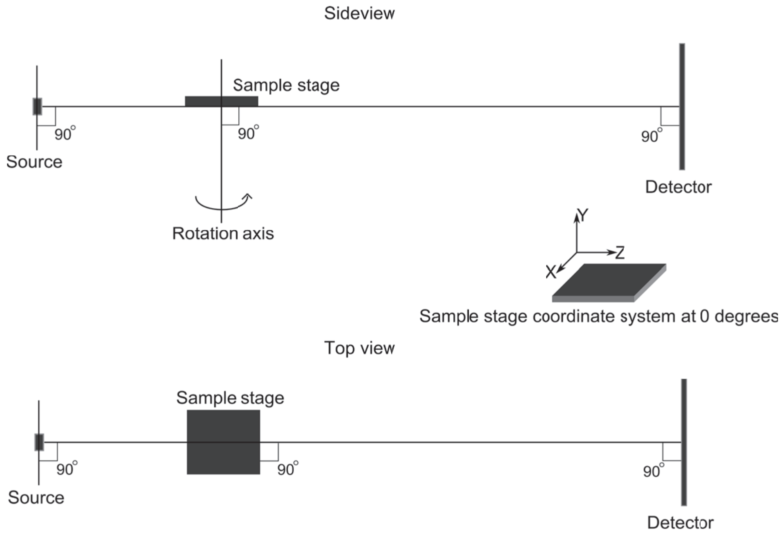

FIGURE 16 A geometry of a typical scanner. The camera and the X-ray source are pointing each others, and in between them is the optical axis. The reconstruction software assumes the rotational axis of sample stage to be perpendicular to the optical axis. Usually there is a x-y table on top of the sample holder allowing to move the sample such that the VOI is placed on the optical axis.

If less resolution and/or faster scan is needed, so-called camera binning can be used. Camera binning means that multiple pixels are combined as one: Binning 2 combines 2x2 pixels area as one pixel, binning 4 combines 4x4 pixels and so on. While it reduces resolution it also shortens the required exposure time and enlarges the rotation step size. This has significant affect to the scanning time and amount of data the scanner produces.

Beam geometries

Currently, there are two main types of beam geometries used in XμCT for X-ray absorption imaging. With X-ray tubes the beam leaves from a single point and spreads conically; see figure 17. The sample is placed in a suitable spot in between the detector and the source, determined by the size of the sample and desired geometrical magnification. In synchrotron, the beam can travel a long distance before being utilized in the μCT device, and at that point the beam is nearly parallel; see figure 17. The spatial resolution results from the optics of the system and effective pixel size of the detector [101]. In addition, there are some less common geometries like fan beam and pencil beam geometry [108].

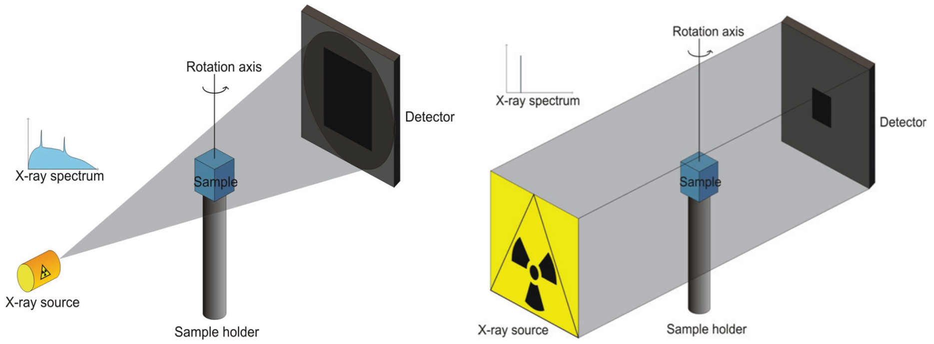

FIGURE 17 The principle of cone beam geometry (on the left) and parallel beam geometry (on the right).

The *detail detectability* of a typical XμCT system is determined by the geometry, spot size and the pixel size of the detector. With this kind of a system the best detail detectability is typically in the range of 500–1000 nm. To achieve a higher detail detectability, advanced X-ray optics are used. These systems use an imaging geometry relying in X-ray optics to shape the beam into magnifying system [94]. See figure 18 for a schematic image of the system. This system produces similar images to “naked” beam geometries. Due to the small field of view a small sample size is required and, thus, a low energy is needed in order to obtain suitable transmission. The X-ray optics used in the systems are quite inefficient and require a high intensity X-ray source.

Phase contrast imaging

In case of low attenuation samples, phase contrast imaging can be used. Phase contrast imaging [233, 185] exploits the Rayleigh scattering and the different refractive indices of different structures. Phase contrast imaging is sensitive to edges in the sample and is suited for samples with low X-ray absorption. There are several techniques for phase contrast imaging. One way is to measure the deflection angle by moving the detector farther away from the sample, which is called propagation-based phase contrast. Moving the detector far away from the sample enlarges the spatial deflection and makes it more visible without the need for high resolution detector. This is possible with even a polychromatic X-ray tube as shown by Wilkinson et al. [261]. Another method is to use diffraction

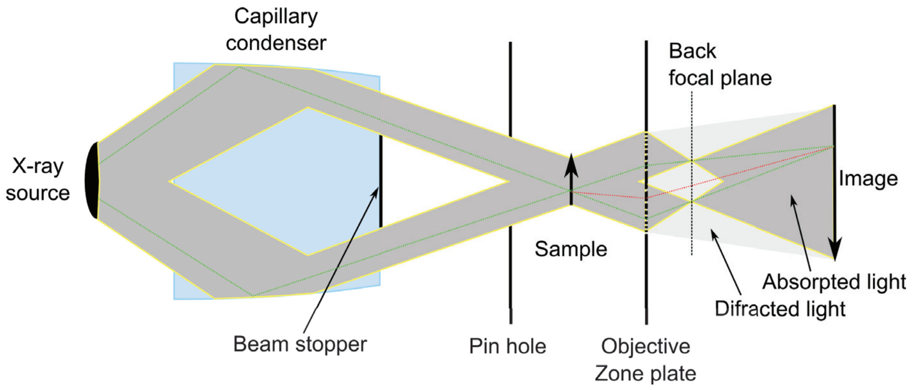

FIGURE 18 A schematic image of a X-ray nanoCT system. The system uses an X-ray condenser to focus the X-rays into the sample and then the objective zone plate to direct the X-rays into the imaging plate. Other methods for condensing the X-rays are also used. An additional benefit of the system is that diffraction imaging is possible by blocking the absorption information with a phase ring set to the back focal plane.

gratings on the beam line, as in ref [124].

2.5 Reconstruction

Reconstruction is the process whereby a collection of shadowgrams is converted into a collection of cross-sectional images. The information required to reconstruct one cross-sectional image is the horizontal lines in the shadowgrams corresponding to the level of that cross-sectional image. The collection of these lines ordered by their acquisition angle is called sinogram [108] (see figure 19 for an example). This is equivalent to the result of Radon transform.

Radon transform [189] is a cross-sectional line integral of a 2D function $f(\mathbf{x}) = f(x,y)$ along straight lines $L \in \mathbb{R}$:

$$Rf(L) = \int_L f(\mathbf{x})\,|d\mathbf{x}|. \tag{5}$$

The lines L can be parametrized with the angle of its normal vector (to the x-axis) α and distance d from the origin such that $(x(t), y(t)) = ([t\sin\alpha + d\cos\alpha], [-t\cos\alpha + d\sin\alpha])$. Thus equation (5) becomes

$$Rf(\alpha,d) = \int_{-\infty}^{\infty} f([t\sin\alpha + d\cos\alpha], [-t\cos\alpha + d\sin\alpha])\,dt. \tag{6}$$

These parameters α and d form the coordinate system of the output of the radon transform (sinogram). The radon transform is a mathematical equivalent of taking X-ray transmission images of some sample over various rotation angles. Figure 19 shows an example of a radon transform.

Now with a mathematical description of the image acquisition the reconstruction is simply the inverse of a radon transform. Reconstruction is the method that converts

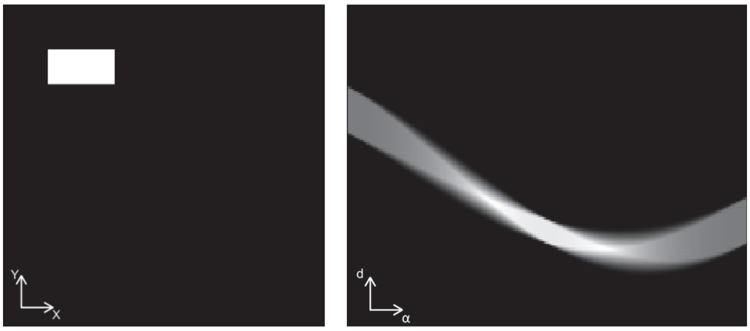

FIGURE 19 Original image $f(x,y)$ (on the left) and its sinogram $Rf(\alpha,f)$ (on the right).

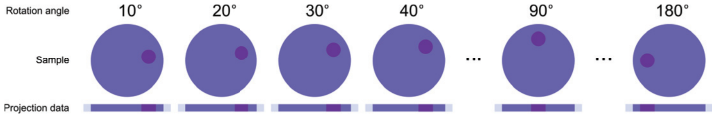

FIGURE 20 Micro tomographic scanner obtains the projection images of the sample from various angles by rotating the sample.

the measured integral of attenuation coefficients (projection data; see figure 20) into cross-sectional attenuation coefficients. There are few algorithms available for reconstruction; filtered back projection [190, 108] being the quickest and most often used, algebraic reconstruction [108] offering more possibilities, but also being more calculation-demanding. The algorithms can reconstruct the image from any number of projections, but the quality of the back projection depends on the number of projections taken. The effect of the number of projections is demonstrated in figure 23. The number of projections affects to the signal-to-noise ratio of the final image and the detail detectability of the imaging system. One theoretical number for the required number of projections is defined as $\pi \times N/2$ [267] or as $\sqrt{2} \times N$ [202], where N is the number of pixels in one horizontal row at the detector. Those provide enough information to reconstruct the 3D image in a resolution determined by the detector pixel size also at the edges of the image. The sample does not always fill the full field of view, and those values can be interpreted as the upper limit.

Here we present the basics of the filtered back projection and algebraic reconstruction algorithms, but for readers with a mathematical background and deep interest in these methods Kak & Slaney [108], Natterer [169], and Turbell [239] provide information in more depth.

Algebraic reconstruction

Algebraic reconstruction was first introduced for image reconstruction in [81]. A cross-sectional image can be considered as the matrix (sampling grid) of values and the measured projection values are integrates (sums of pixels) over the cross-sectional image to a direction of a. Thus we can write $\Sigma_{j=1}^{N} w_{ij} f_j = p_i, i = 1, 2, 3, ..., M$, where p_i is the integrated intensity value along "X-ray" i, f_j is the intensity value in pixel j and w_{ij} is a weight factor for pixel j in beam i. In practice, w_{ij} is the cross-sectional area of the beam i and the cell j (note that $w > 0$ only for pixels that lay along the beam's path). N is the total amount of pixels and M is the number of detector pixels multiplied by the number of projections. See figure 21 for more details. This formulation allows us to create a series of equations for the unknown values f_j for each rotation step:

$$\begin{cases} w_{11}f_1 + w_{12}f_2 + w_{13}f_3 + \cdots + w_{1N}f_N & = p_1 \\ w_{21}f_1 + w_{22}f_2 + w_{23}f_3 + \cdots + w_{2N}f_N & = p_2 \\ \vdots \\ w_{M1}f_1 + w_{M2}f_2 + w_{M3}f_3 + \cdots + w_{MN}f_N & = p_M \end{cases}$$

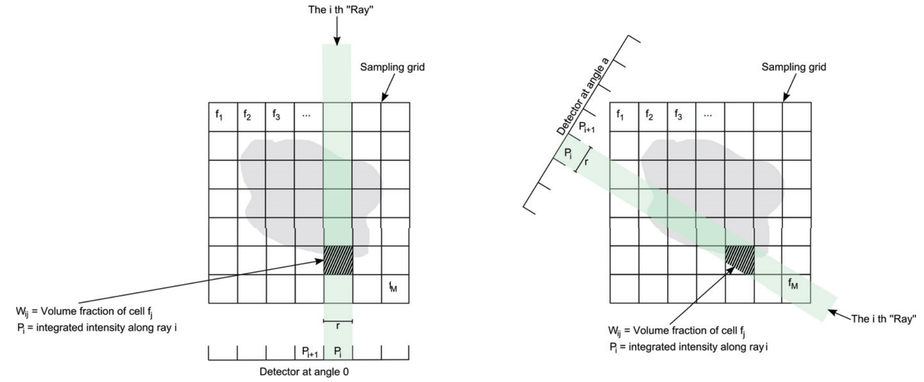

FIGURE 21 The principle of algebraic reconstruction.

Due to a huge number of equations and noise present in projection data, this can not be solved by using traditional methods like Gaussian elimination, thus, iterative solvers are used. Those require an initial guess that is iteratively enhanced. The iterative enhancement is based on function:

$$\Delta f_j^{(i)} = f_j^{(i)} - f_j^{(i-1)} = \frac{p_i - q_i}{\Sigma_{k=1}^{N} w_{ik}^2} w_{ij},$$

where q_i is p_i equivalent projection value from the $i - 1$ solution of the reconstruction.

The benefits of the iterative reconstruction is insensitivity to both reconstruction artefacts and noise, and the possibility to reconstruct high quality images from incomplete data [272, 73]. The downside is that the iterative methods are relatively slow and computationally demanding.

Filtered back projection

Back projection [108, 169] refers to a method where the projection signal is smeared back to the image plane perpendicular to the direction of the beam. That is, the transmission images are projected back into the image space as shown in figure 22.

As seen in figure 23, the result of plain back projection is smoothed at the edges of the material. The reason for the blurring is that each back projection also adds extra

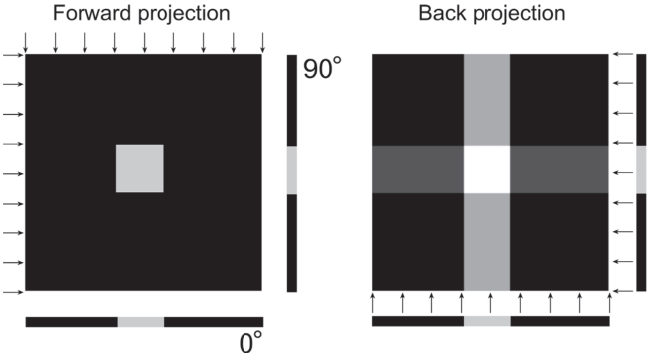

FIGURE 22 On the left a schematic image of the forward projection process at two projection angles. On the right the same projection images back projected into cross-sectional image plane.

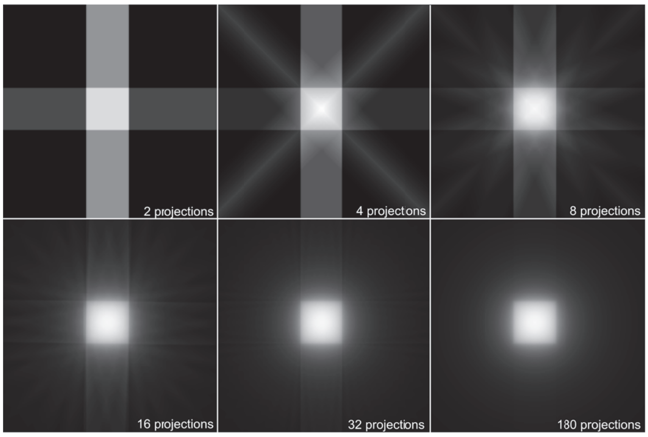

FIGURE 23 The effect of the number of projections on the final reconstructed cross-sectional image for unfiltered back projection.

information, “a tail”, along the projection angle. Filtered back projection (FBP) method avoids the blurring by high pass filtering the projection data such that the blurring effect at the resulting image is cancelled. Commonly used high pass filters are Ramp, Shepp-Logan, Cosine, Hamming and Hann. The effect of different filters is demonstrated in figure 24. The filtering is usually done in Fourier space; when combined with the Fourier slice theorem we get efficient reconstruction algorithm, allowing the high pass filtering to be done for the 1-D line projection. The Fourier slice theorem states that the result of the following two calculations are equal:

1. Take a two-dimensional function, project it onto a (one-dimensional) line and perform a 1D Fourier transform (FT) of that projection.
2. Take that same function, do a two-dimensional Fourier transform first and then slice it through its origin, which is parallel to the projection line.

The reconstruction procedure using the Fourier slice theorem follows:

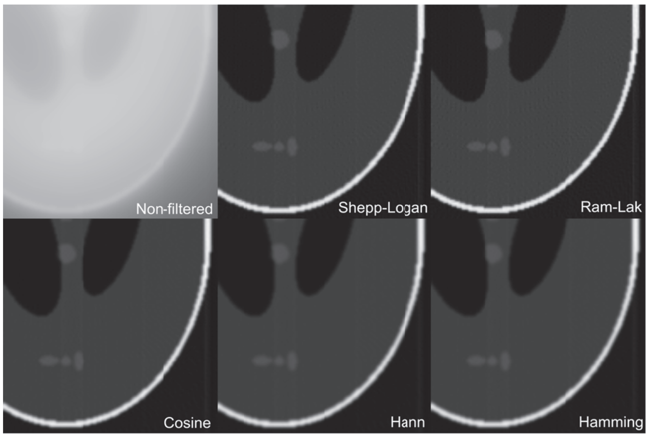

FIGURE 24 The effect of the different filters used in Filtered Back Projection algorithm. The result is often a compromise between noise and sharpness.

1. Calculate the 1D FT of the projection data collected at angle θ and high pass filter it.
2. Arrange the 1D FT to 2D grid to θ angle.
3. Interpolate the data to the rectangular 2D grid.
4. Perform the inverse transform for the 2D grid.

The main disadvantage of this method is the interpolation step that often requires complicated interpolation processes. However, the FBP is robust and the most efficient reconstruction algorithm. The GPU-based algorithms can reconstruct even large stacks in minutes.

2.6 Artefacts

The imaging method and reconstruction can cause certain artefacts to the resulting image. Barrett and Keat [19] have diligently described the artefacts that occur in medical CT imaging. They divided artefacts into four classes: physics based, object based, scanner based and reconstruction based. We will here review these artefacts in the viewpoint of XμCT.

Scanner based artefacts

Ring artefacts are dominant scanner-based artefact that can disturb the segmentation; see figure 25. Ring artefacts appear as complete or partial circular strikes in the image. They are caused by a sensitivity difference in the CCD pixels [14, 6]. They appear especially on planar horizontal interfaces between materials having notably different density. Ring artefacts can be reduced by using random movement of the sample or CCD during the scan;

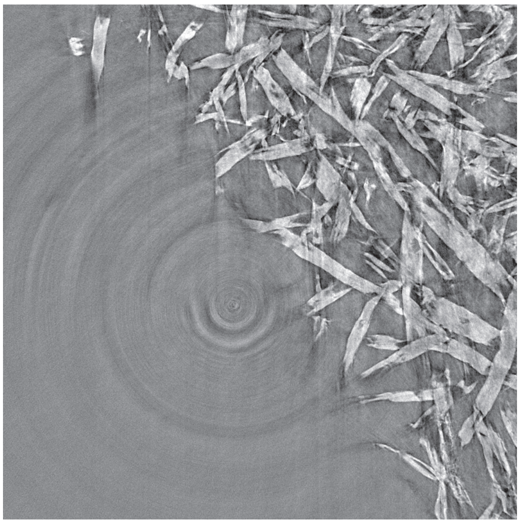

FIGURE 25 Ring artefacts on a paper sample.

the sample is moved small random distances in x-y direction between the acquisition of each shadow image. These movements are recorded and reduced before the reconstruction. This effectively prevents the defective pixels of the detector from causing the rings. Algorithmical approaches for ring artefact reduction also exist [218, 32, 14].

Lack of sharpness at the edges is another visible artefact of the table-top XμCT scanners. The scanners use X-ray tubes to produce the radiation and those sources have a spot size limiting the maximal spatial resolution of these systems. This effectively requires the system to have a point spread function, causing blurring of the edges on the resulting image.

Under sampling occurs when the rotation step of the scanner is too large. It can cause stripe-like structures appearing around the object and along the edges of the objects.

Finally, when scanning, the inaccuracy in mechanics can cause misalignment of shadowgrams. This misalignment has to be taken into account in the reconstruction. If this is done improperly the edges of the images have discontinuation at certain angle, see figure 28.

Physics based artefacts

Beam hardening is a property of an X-ray tube that it is not possible to completely remove. This is because low energy X-rays absorb more rapidly than high energy ones when travelling through material, causing the beam to “harden”. It means that the average beam energy (intensity in final images) increases when the X-rays pass through the object. Beam hardening causes two kinds of artefacts:

1. A cupping effect, where the edges of an object appear brighter than the center. See figure 26.

2. Streaks and dark bands that appear in between dense objects. This happens when X-rays pass through dense objects that are oriented in the direction of the beam. The

beam is hardened more when it passes through the two objects than when passing only one. See figure 26.

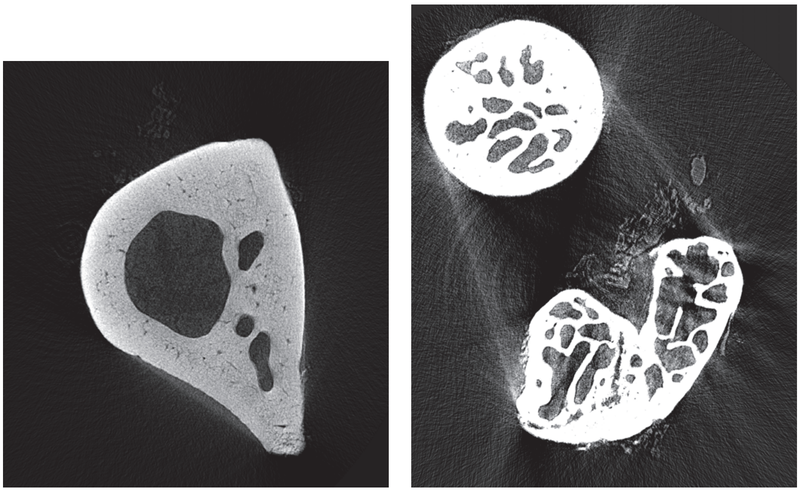

FIGURE 26 On the left: The effect of beam hardening on bone sample. The edges of the bone appear brighter than the inner material. On the right: Streaks and shadows in a bone sample.

Beam hardening can be reduced by cutting unnecessary energies from the spectrum using a filter at the X-ray beam line. Furthermore, methods have been implemented for reconstruction software to correct the beam hardening computationally [248, 127]. The beam hardening compensation algorithms are different depending on number of material phases the sample contains [270].

Photon starvation is due to a reason similar than beam hardening; it happens when some parts or some positions of an object are absorbing X-rays such that an insufficient amount of X-rays reach the detector for these parts / positions. The effect of photon starvation is very visible streaking. For example, small pieces of high density material, like metal, inside an object can cause strong streaking artefacts; see figure 27. The density of metal is usually notably higher than surrounding material, causing photon starvation. This is best avoided by choosing suitable samples or removing the metallic parts. There are also some algorithms to correct these artefacts [104, 143].

Object-based artefacts

One of the most common object based artefacts is the movement of the object during the scanning. It can happen if the object is not planted properly, or if the object itself is not stable (sloppy objects, statically charged particles, etc.). The movement can cause blurring, soft edges, stripes, etc. In XμCT, object can usually be mounted tightly to the sample holder, but elastic objects or objects containing liquids can move during the scanning. On most cases there are no algorithmical remedies for these effects, instead one needs to consider different sample holders. In cases of systematic movement caused by

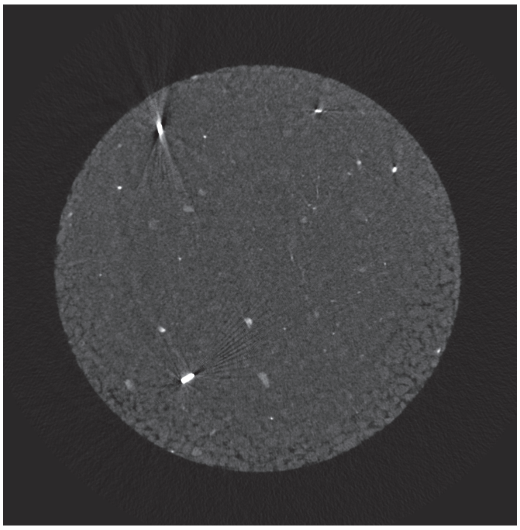

FIGURE 27 Metal artefacts inside a bentonite sample.

thermal expansion of the mechanics, few algorithms have been done to avoid the problem [205]. If the movement is rigid translation, an image correlation can be used to align the shadowgrams.

An other sometimes unavoidable artefact is caused by scanning a sample that is larger than the volume of interest. It causes blurring of details and shadows into the reconstruction. This is especially noticeable if the parts that do not fit into the volume of interest are significantly denser. However, in some cases it is necessary to scan only some area inside the sample; to reduce the artefacts it is recommended to increase the number of shadowgrams taken

Partial volume effect is a common artefact when analysing porous materials. It happens when a sample contains details that are smaller than the voxel size. If one voxel contains a mixture of material phases the overall absorption value might not reflect any of the materials inside the voxel. In the case of porous material, the pores that fill a voxel only partially will decrease the intensity of the voxel.

Reconstruction based artefacts

The most commonly used reconstruction algorithm in cone-beam geometries, filtered back-projection, is a non-exact algorithm [210]. Due to the non-exactness, an approximation of data is used on areas that are not at the mid-slice, causing artefacts to appear [245, 239]. The artefacts causes blurring of details and it is more prominent further we move from the mid-slice.

Noise

Noise is an unwanted random signal alteration in image, providing no additional information over the original signal. It is generally considered as pollution caused by analogous components of the imaging machine (see section 2.3 for more details). On XμCT

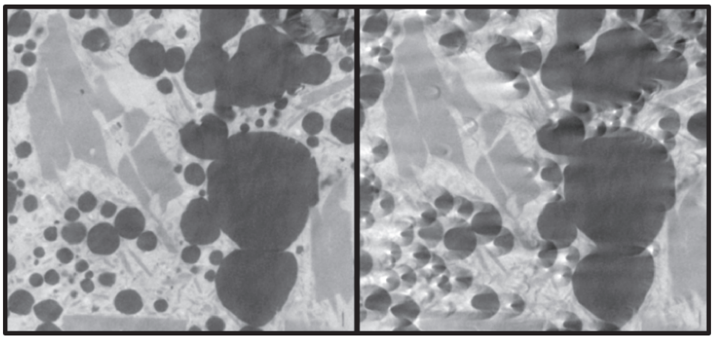

FIGURE 28 Properly aligned (on left) and misaligned reconstruction (on right) of igneous rock.

scanners the most noise comes A/D conversation when X-ray intensity information is converted into a image within CCD-chip and from Poisson-type process of X-rays.

To reduce the noise in the image averaging multiple images or having longer exposure time will help. However, it is impossible to remove the noise fully and therefore computational denoising algorithms are needed.

Sample preparation

Depending on sample, the sample preparation can be easy of hard. Large blocks of solid materials are easy to plant on top of capillary tube by glue. However, XμCT is suitable for imaging virtually any kind of samples and not all of the behave well; fragile materials, thin materials, fibres, particles, humidity sensitive materials, and so on, can require a specific tools for cutting them and also specific sample holder to support them firmly. Preparing those samples can require imagination and practicality.

Tools used for preparing the samples include, e.g., cutting devices, various types of sample holders, glues, microscopes, and micro-manipulators. For cutting, a precision diamond blade saw is suitable for hard materials like metals, stone, bone, and glass. The device uses water to reduce the friction. For more sensitive samples a diamond wire saw causes less mechanical damage to the surface. Razor blade, scalpel and scissors are good for various softer materials, like paper, composites, wood and wools, but only if the sample size is rather large, 2-20 mm. Otherwise the internal structure may break.

For non mechanical cutting devices there are few options. Laser micro machining can be used various sample materials when the sample size is in the range of 50μm to 1–2 mm. Laser is able to cut hard and soft material with little damage to the outside of the cutting zone. The cutting ability is dependent on the power and wavelength of the laser. For light organic material, 355 nm is good. For harder materials 532 nm or 1064 nm is sufficient. The method does heat up the material close to the cutting area, but it is usually in very short range. Focused ion beam (FIB) is suitable for very small samples, sizes ranging in 1-20μm. FIB is able to cut through any material, and it is based on bombarding material with heavy ions that will break the atomic structure of the target material. The samples, however, need to be coated with some electrically conductive material, and the process is done in a vacuum. The method does heat up the material and may also cause FIB artefacts [7] where lighter atoms are removed more efficiently than

TABLE 1 The average gray value inside a sample when using beam hardening filtering (both hardware and software) and no beam hardening correction.

Sample	No BHC	BHC
2x4 mm	34582	44531
1x4 mm	37409	44770
2x2 mm	40118	45559

heavier ones.

For porous materials, a low viscous glue can absorb into the material. A more viscous glue or a post-it paper (glued on top of a sample holder) is more suitable. For fragile and soft samples, a cup like sample holder will support it better than plain sample holder tube. A plastic is easy to process and has low absorption coefficient. Usually the cup can be segmented out from the final images. Powdery samples can be put into a straw. During the scanning the movement might shake the samples causing them to compress. To avoid this the sample should be pre-shaked. Also some kind of a support material, like plastic, can be used but it might reduce the contrast.

2.7 Repeatability

A common problem in analysis of XμCT images is comparison of results of multiple scans. Especially the are the gray values comparable. A easy solution to this problem is to fit all the samples into a single scan, but this is not always possible.

Naturally, to ensure that the images are comparable together, the same scanning and reconstruction parameters need to be used. However, there are also other factors (artefacts) affecting the final gray value of the material. Especially partial volume effect caused by different porosity of the materials, and the intensity variation due to beam hardening if the sample size is not the same.

To this end we analysed three aluminium blocks of varying size using Xradia MicroXCT-400. The sample were first imaged without any X-ray filtering or software beam hardening correction (No BHC) and then with both X-ray filter and software beam hardening correction (BHC), with the same parameters for all scans. The results are shown in table 1. Obviously, if the beam hardening is not taken into control the sample shape does affect the gray values of the sample even though the parameters were otherwise the same. With X-ray filtering and software beam hardening correction the results were comparable.

In table 2 the effect of various scanner parameters are tested. The change of rotation angle had a major effect on the gray value (for unknown reason). The distance between sample and source or detector affects slightly, probably because X-rays absorb into the air. The exposure time change also had a small effect. These naturally might be scanner- (or reconstruction software-) dependent.

We can conclude that if the scanner parameters are kept the same, especially the rotation angle and the internal distances, the sample size is approximately the same, and the beam hardening is taken into account the samples imaged with separated scans are

TABLE 2 The effect of scanner parameters to the gray value of the resulting image.

Description	Average intensity
Normal conditions	45559
0.5 times smaller rotation angle	53646
1.5 times exposure time	43345
Source sample distance 0.25 times longer	43964

comparable. An another aspect are the environmental factors affecting to the sample. Temperature and humidity changes can alter the sample structure or the sample holder.

Often the sample imaged with an XμCT system is a small piece of a larger sample. If the size of the sample is very small (because the interesting structural properties are small) the sample itself might not be representative for the whole material. Term representative elementary volume (REV) [23] is used of the smallest possible sample that represents the material in such a way that the analysed parameters are independent of the size of the sample. Often REV is found by studying convergence properties of the analysis parameter or some other closely related parameter [3]. In tomography REV can be found by analysing the parameter (for example, porosity) as a function of volume of interest and multiple scans.

2.8 Visualization

3D visualization is a tool that can be used to show the tomographic reconstructions in 3D form. In XμCT imaging, the voxels are usually uniform in size (they have the same dimensions to all directions) and, thus, the visualization is straightforward. For 3D voxel data there are two main visualization methods: volumetric visualization and iso-surface visualization.

In volumetric visualization each voxel in the image is coupled with color and opacity information using transfer functions. The opacity transfer function can be used to give each gray value an opacity value. In CT images the color represents the density of the sample and thus the transparency function can be used to remove materials according to their density; see figure 29 for examples of using the opacity transfer function. Colour transfer function are used to map each gray value with a color; see example in figure 29. The actual volumetric visualization is performed usually using the GPU texture mapping allowing real time interaction with the sample. The user can rotate and cut the sample in any way. There are also other visualization methods for volumetric data that allow usage of lightning and shadows.

In iso-surface rendering the surfaces of the image are detected and only the surfaces are visualized rendering them as meshes. The standard way to detect the surfaces is the marching cubes algorithm [145]. The iso-surface rendering is especially useful when some structure inside another structure is visualized. The shape of the structure can be visualized as an iso-surface with reduced opacity while the inner structure can be volume visualized with full opacity.

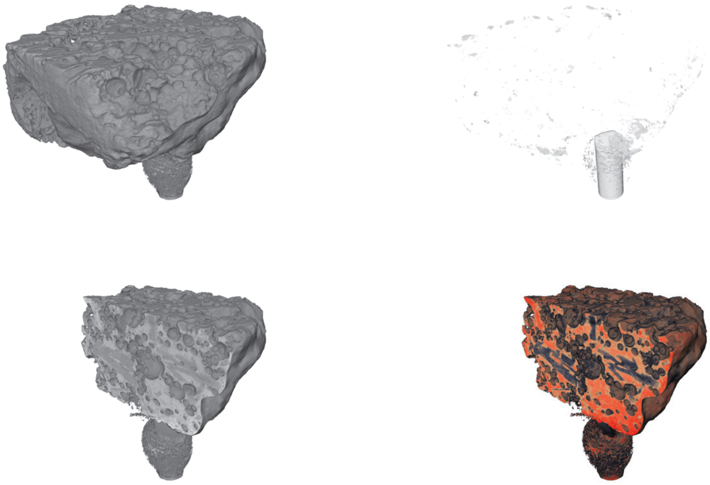

FIGURE 29 Visualization effects demonstrated on volcanic stone sample. On top left, normal visualization; on top right, only the more dense parts (sample holder and some spots inside the sample) are visible. On bottom left, part of the sample is cut away; and on bottom right, a color map is applied to emphasize the different minerals.

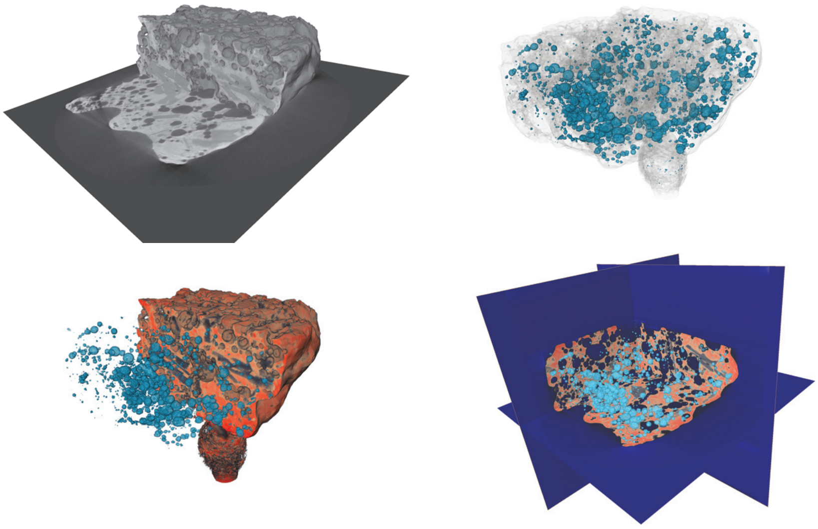

FIGURE 30 On the top left a cross-sectional image as a part of the whole image. At top right, the outline of the sample is produced as partially transparent surface rendering with pores at blue inside. On the bottom right, the original image with a part of it cut away and pores included into that space. On the bottom left, orthonormal slices of the sample and some pores in blue as volume rendering.

The ways of visualization

Visualization of XμCT images is a combination of art and science with an aim to show interesting structure or to emphasize certain property of the sample. Sometimes it is only necessary to get a visually pleasant image of the sample. The means for getting good visualization include the following: opacity transfer function, color transfer function, pose of the sample, shadows and lightning, surface material (for example specularity can be used to give a plastic look), cuts (see figure 30), cross-sectional images (see figure 30), combining multiple images with different opacity/color, etc. properties (see figure 30)

Many of the visualization programs allow you to create a videos. Some programs allow only simple rotation of the sample, but more sophisticated ones allow one to adjust all imaging parameters during the video and edit the camera route around or inside the sample.

3 ON IMAGE PROCESSING ALGORITHMS

The image processing phase of the XμCT continuum (figure 3) aims at extraction of numerical data from the image. There is no specific routine that works on any data, instead, given the image and problem, manual work is required to build up an appropriate processing scheme from collection of image processing methods. The selections made to build the scheme affect on how repeatable and automatic the process is. This is important as often many similar kind of images are analysed and it is beneficial if the scheme can be automatically repeated for another image.

In practice there exists a huge number of image processing algorithms. Even for a simple task there are various implementations and improvements. Thus, it is impossible to cover the image processing field even close to extensively. Instead the aim of this chapter is to provide an overview of general methods and definitions related especially on XμCT image analysis, concentrating on algorithms that are simple, fast and do not require an excessive amount of memory. Noise reduction, segmentation and image analysis are discussed in their own chapters.

3.1 Algorithmical requirements

There are certain requirements when considering the algorithms used for processing of the XμCT images. These requirements come from the end-users and the type of the data the XμCT devices produce.

Basically there are two distinct roles involved in image processing: method user and method developer [16, 86]. Their primary domains of interest can be described as problem domain (images) and solution domain (algorithms). The challenge for those who develop methods is to keep the imaging process continuum (i.e. transform from problems to solutions and back) smooth and approachable for the user. The amount of data, the quality of the result and the fact that the end users are not experts in image processing emphasize certain criteria that need to be taken into account in the method development.

An algorithm should handle data in a reasonable time; if there are bottlenecks in the image processing continuum the overall process will be disturbed. The algorithm should have high usability. There are different studies of usability of a system, like Nielsen [172] and Shackel [214]. These studies can also be partially applied to algorithms and as users are not experts on algorithm details, the high usability is desired. In the case of algorithms the user interaction is done with the parameters. The parameter set of an algorithm can be analysed in a sense of learnability, efficiency, flexibility, memorability, etc. [172]. An optimal algorithm would be a black box that immediately outputs the perfect result for any input image without any user interaction. In other words high learnability, flexibility, efficiency to use, and ease of memorizing. Usually, however, some interaction is needed in a form of parameters. There are few aspects that affect the learnability of parameters:

- How explicitly can the effect of a parameter be explained?
- How exactly can the value of the parameter be determined?
- How well is the domain of definition of the parameter given?

The effect of a parameter is best described in terms from the problem domain. This increases the learnability and memorability of the parameter. It will also make them more understandable for the end users who are experts in the problem domain but not in algorithmical details. In addition it can save time as the end user does not need any extra burden to test alternative parameters. The domain of definition of parameters is important with algorithms that have multiple parameters. Each parameter should affect a certain property of the result, but not a property that is to be controlled by some other parameter. Non-overlapping domains of parameter effect increase the flexibility of an algorithm by excluding intrinsic dependencies on the parameter set. Despite the simplicity and speed, the algorithms should also be efficient. For example, a denoising algorithm should remove the undesirable effects but leave relevant features untouched.

Memory consumption problems arise easily when implementing the algorithms for large images. There are various factors affecting the memory consumption. Some algorithms need several copies of the original data (or equivalent amount of “work space”), considering the data type, the size difference between byte (256 gray values) and double ($\pm 1.7^{\pm 308}$ gray values) is big and selection of the data type used in processing can significantly affect to the memory consumption. And it is also important to realize that in some programming languages boolean type (1-bit) data is often stored in other variables having a size larger than 1 bit, the smallest possibility often 8-bit images [258]. It should also be noted that not all the calculation operations performed on different data types are as fast. Some more details on these issues can be found in Appendix 1.

3.2 Definitions

Here we define the mathematical notation used in the rest of the thesis.

3.2.1 Image

Digital image is a discrete approximation (both in spatial and intensity range) of a continuous 2D/3D intensity signal. A digital image is an array of picture elements, that each cover a certain area of the original continuous space and has a value relative to the intensity in that space. The picture elements are *discrete points* called pixels in 2D and *voxels* in 3D. Pixels have a surface area while voxels have a volume.

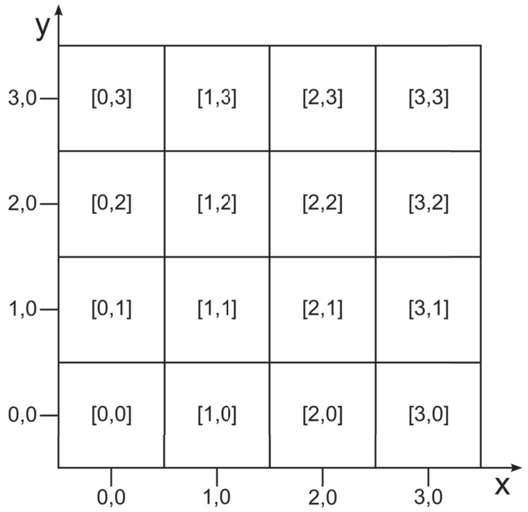

FIGURE 31 The pixel indexing in $\mathbb{Z}$ (in black) and $\mathbb{R}$ -axes (in blue) of a imaging system in 2D. The values inside parentheses are pixel indexes and the black dots are the centres of pixels.

We define a 3D image as function $a : \Omega \rightarrow Y$, where Ω is a coordinate system in the image and Y defines the gray value intensity at those coordinates, hence dom(a) = Ω and ran(a) = Y. The coordinate system of a digital image typically refers to pixels/voxels using indexes that are integers. Real value coordinate systems can also be used; real value coordinates refer to a (exact) point in the image. In this work, we use the coordinate system shown in figure 31; the origo of real value coordinates is at the center of pixel with index (0,0) (There is no common rule for the location of the pixel center; instead various schemes exist, for example, in directX [161]). When referring to the voxel indexes a notation $a[\mathbf{v}] = a[i,j,k]$, $i,j,k \in \mathbb{N}$ is used. When referring to a point in a continuous coordinate system a notation $a(\mathbf{v}) = a(x,y,z)$, $x,y,z \in \mathbb{R}$ is used.

For spherical coordinates in $\mathbb{R}^3$ the Cartesian x, y and z are transformed into r, ϕ, θ coordinates. Here r is the distance from the origo, ϕ is the angle between the positive x-axis and the line from the origin to the (x,y,z)-point projected onto the xy-plane and θ is the angle between the positive z-axis and the line formed between the origin and point (x,y,z). The cylindrical coordinate transform is realized by transforming x and y coordinates to the polar coordinate system and leaving the z coordinate to its original meaning. In the polar coordinate system the Cartesian x and y coordinates are transformed into an angle θ and distance r system:

The type of codomain Y depends on the bit-depth of the image, that is the number of distinct gray levels in the image. Usually the bit-depth is, due to technical reasons, a power of 2. Some of the typical bit depths are as follows:

- 8-bit (a byte) unsigned images: $Y \subset \mathbb{Z}, Y = [0,255]$

- 16-bit unsigned images: $Y \subset \mathbb{Z}, Y = [0, 65536]$
- 32-bit float images: $Y \subset \mathbb{R}, Y = [-3.4 \times 10^{38}, 3.4 \times 10^{38}]$
- 8-bit (a byte) signed images: $Y \subset \mathbb{Z}, Y = [-128, 127]$
- 16-bit signed images: $Y \subset \mathbb{Z}, Y = [-32768, 32767]$

Basic arithmetic operations (subtraction, addition, multiplication, division) between two images are performed voxelwise. Translation $T_t(a)$ of image a by vector t creates a new image b with dom(b) = dom(a) + t.

A *binary image* is an image containing only values 1 and 0 often called foreground and background respectively. We define few boolean operations for binary images. Let a and b be binary images and $\mathbf{v}$ a voxel in the image:

$\hat{a}$	Inverse image:	$\hat{a}[\mathbf{v}] = \neg a[\mathbf{v}]$
$a \cup b$	Union of images:	$(a \cup b)[\mathbf{v}] = a[\mathbf{v}] \vee b[\mathbf{v}]$
$a \cap b$	Intersection of images:	$(a \cap b)[\mathbf{v}] = a[\mathbf{v}] \wedge b[\mathbf{v}]$

In addition we define a *masking operation* between a gray value image a and binary image b as following: $a \cup b = a[\mathbf{v}] * b[\mathbf{v}]$. As b has values 0 and 1 masking operation will zero all values of a outside the solid phase of b. In practice it means that the operations are only performed at the mask area.

3.2.2 Voxel neighbourhoods

Let $\mathbf{v} = [i, j, k]$ be a voxel index. We define a *voxel connectivity* operator $\mathcal{C}_n[\mathbf{v}]$ as a group of voxels containing n voxels connected to $\mathbf{v}$. In 3D there exist three commonly used voxel connectivities: 6-, 18-, and 26-connected. In 6-connectivity the voxels are face connected: $[i \pm 1, j, k]$, $[i, j \pm 1, k]$, $[i, j, k \pm 1]$ to voxel $[i, j, k]$. In 18-connectivity the voxels are face and edge connected: $[i \pm 1, j \pm 1, k]$, $[i \pm 1, j, k \pm 1]$, or $[i, j \pm 1, k \pm 1]$ to voxel $[i, j, k]$). In 26-connectivity face, edge and corner are connected: $[i \pm 1, j \pm 1, k \pm 1]$ to the voxel $[i, j, k]$. See figure 32 for visualization. The selection of n can affect to the results and should be chosen according to the algorithm or left for the user to select.

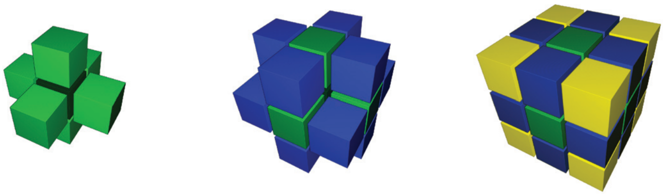

FIGURE 32 Voxel neighbourhoods: on the left 6-connected, at center 18-connected, and on the right 26-connected.

A *voxel neighbourhood* is a collection of voxels surrounding $\mathbf{v}$ but not necessarily directly touching it. The shape of the neighbourhood is typically square or round, but can be basically of any shape. We define the neighbourhood as:

$$\mathcal{N}_r^p[\mathbf{v}] = \{\mathbf{q} : ||\mathbf{v} - \mathbf{q}||_p < r\},$$

where r is the radius and p is the distance norm that determines the shape of the neighbourhood. For the square neighbourhood l_1-norm is used, and for the spherical neighbourhood the l_2-norm. In case the norm and radius are not essential for expressional ability of the equation, the notation can be shortened to $\mathcal{N}[\mathbf{v}]$. We use $\mathrm{Ave}(\mathcal{N}[\mathbf{v}])$ for mean value and $\mathrm{Var}(\mathcal{N}[\mathbf{v}])$ for variance of the neighbourhood $\mathcal{N}[\mathbf{v}]$.

For set V of voxels, we can define two borders: inner border $B_{\mathrm{in}}(V)$, and outer border $B_{\mathrm{out}}(V)$. For $V \subset \mathrm{dom}(a)$ the inner border reads as

$$B_{\mathrm{in}}(V) = \{\mathbf{v} \in V | \exists \mathbf{q} \in \mathcal{C}_n[\mathbf{v}] \text{ such that } \mathbf{q} \notin V\}. \tag{7}$$

and similarly, the outer border is defined as

$$B_{\mathrm{out}}(V) = \{\mathbf{v} \notin V | \exists \mathbf{q} \in \mathcal{C}_n[\mathbf{v}] \text{ such that } \mathbf{q} \in V\}. \tag{8}$$

3.2.3 Discrete derivatives

The derivatives are approximated using so-called *finite difference methods* (explained in more detail for example in [220]). The general equation for a discrete derivative in 1-D is as follows:

$$f'[i] \approx \frac{f[i+h_1] - f[i-h_2]}{h_1 + h_2}, \tag{9}$$

Usually h_1 and h_2 are 0 or 1. If $h_2 = 0$ and $h_1 > 0$ the system is called forward difference, $h_2 > 0$ and $h_1 = 0$ backward difference and $h_1 = h_2$ central difference. For digital image a we, thus, mark the general finite difference approximations of partial derivatives as

$$a_x[i,j,k] = \Delta^x_{[h1,h2]} a[i,j,k] = \frac{\partial a}{\partial x} \approx \frac{a[i+h_1,j,k] - a[i-h_2,j,k]}{h_1 + h_2}, \tag{10}$$

$$a_y[i,j,k] = \Delta^y_{[h1,h2]} a[i,j,k] = \frac{\partial a}{\partial y} \approx \frac{a[i,j+h_1,k] - a[i,j-h_2,k]}{h_1 + h_2}, \tag{11}$$

$$a_z[i,j,k] = \Delta^z_{[h1,h2]} a[i,j,k] = \frac{\partial a}{\partial z} \approx \frac{a[i,j,k+h_1] - a[i,j,k-h_2]}{h_1 + h_2}. \tag{12}$$

The second order (central) derivative can be similarly calculated using

$$f''[i] = f'[f'[i]] \approx \frac{f[i+h] - 2f[i] + f[i-h]}{h^2}, \tag{13}$$

and Laplacian is

$$\nabla^2 a = a_{xx} + a_{yy} + a_{zz}. \tag{14}$$

The mixed derivatives can be approximated using the following equation:

$$\frac{\partial^2 a}{\partial x \partial y} = \frac{\partial a}{\partial x}\left(\frac{\partial a}{\partial y}\right). \tag{15}$$

In 3D the gradient for image a is defined as:

$$\nabla a = \left[\frac{\partial a}{\partial x}, \frac{\partial a}{\partial y}, \frac{\partial a}{\partial z}\right].$$

3.3 Standard image processing operations

Certain operations are more general in image processing and are often used as a building block for larger image processing methods. In this section we describe some basic image processing operations that are often used as a part of a more complicated method. The operations can typically be classified into three categories:

- Point: The output of the operation at pixel index $[i, j, k]$ depends only on the input at the same coordinate.
- Local: The output of the operation at pixel index $[i, j, k]$ depends only on the input values of the neighbouring voxels.
- Global: The output of the operation at pixel index $[i, j, k]$ depends on all values in the image.

3.3.1 Statistical operations

Statistical operations are some simple operations based on statistical processing of the image data.

Histogram

Histogram is a graphical representation of any data in a form of a discrete distribution, introduced first by Pearson [180], who called them frequency curves. Usually the x-axis represents the studied variable and the y-axis represents the frequency of that particular variable. The x-axis is represented in discrete intervals called bins.

A typical histogram in image processing is the gray value histogram of the image where the x-axis represents the gray value and the y-axis represents the amount of voxels having that gray value. If our image is $a : \Omega \to Y \in \mathbb{Z}_+$ having intensity values $Y \in [y_0, y_n]$, histogram is a discrete function:

$$H[T] = \sum_{[\mathbf{v}] \in \Omega} I[\mathbf{v}], \tag{16}$$

where

$$\begin{cases} I[\mathbf{v}] = 1 \text{ if } a[\mathbf{v}] = T, \\ I[\mathbf{v}] = 0 \text{ else.} \end{cases}$$

Where the bin size is 1 and intensity values are assumed to be integer valued. Value $T \in [y_0, y_n]$ represents the bin label. With real valued images, the bins are considered as intervals.

$$H[T] = \sum_{[\mathbf{v}] \in \Omega} I[\mathbf{v}], \tag{17}$$

where

$$\begin{cases} I[\mathbf{v}] = 1 \text{ if } a[\mathbf{v}] \in [T - \frac{1}{2}w, T + \frac{1}{2}w[, \\ I[\mathbf{v}] = 0 \text{ else.} \end{cases}$$

where the bin labelling is done at w intervals: $a = \left\{ y_0 + \frac{1}{2}w, y_0 + 1\frac{1}{2}w, y_0 + 2\frac{1}{2}w ... \right\}$. A cumulative histogram is a function that counts the cumulative representation of samples up to the specified bin $H_c[T] = \sum_{j=y_0}^{T} H[j]$.

Image moments

Image moment [80] is an intensity-weighted average of the voxel coordinates of the whole image or a certain area (i.e. a particle) in the image. In continuous form for three dimensional function f, the moment of order $(p + q + r)$ is:

$$M_{pqr} = \int_{\infty}^{\infty} \int_{\infty}^{\infty} \int_{\infty}^{\infty} x^p y^q z^r f(x, y, z) \mathrm{d}x \mathrm{d}y \mathrm{d}z. \tag{18}$$

For a discrete image its moment can be used to calculate shape-related features like volume, center of mass and orientation information. Let a be an image; the discrete image moments of order of (α, β, γ) are defined as:

$$M_{\alpha\beta\gamma}(a) = \sum_i \sum_j \sum_k x^\alpha y^\beta z^\gamma a[i, j, k]). \tag{19}$$

Zero order moment M_{000} is the volume, mass, or intensity sum of the area. The center of mass $[x_c, y_c, z_c]$ is:

$$x_c = M_{100}/M_{000}, \quad y_c = M_{010}/M_{000}, \quad z_c = M_{001}/M_{000}. \tag{20}$$

The orientation of the object can be approximated using the second order image moments. The method will give three orientation vectors that are perpendicular to each other. The longest one is the main orientation. To calculate the orientation we need to use translation invariant central moments, which are defined as

$$\mu_{\alpha\beta\gamma}(a) = \sum_i \sum_j \sum_k (i - x_c)^\alpha (j - y_c)^\beta (k - z_c)^\gamma a[i, j, k].$$

From these moments a covariance matrix is constructed:

$$cov(p) = \begin{bmatrix} \mu'_{200} & \mu'_{110} & \mu'_{101} \\ \mu'_{110} & \mu'_{020} & \mu'_{011} \\ \mu'_{101} & \mu'_{011} & \mu'_{002} \end{bmatrix}, \tag{21}$$

where $\mu'_{ijk} = \frac{\mu_{ijk}}{\mu_{000}}$. The eigenvectors of $cov(p)$ are the orientation vectors. The corresponding eigenvalues define the strength of the orientation; the largest value is associated with the main orientation. The eigenvalue can also be used to approximate the shape of an object:

- If all eigenvalues are close to each others the shape is spherical.
- If one eigenvalue is large and two other are close to each other, the shape is tubular.
- If one eigenvalue is small compared to the other two, the shape is sheet-like.

3.3.2 Binary image operations

Morphology is a technique for the analysis and processing of geometric structures. It is based on a few basic operations. We present the morphological operations in general form that work for binary and gray value images. Let a be an image and b a binary image called a structuring element. For the sake of simplicity we assume the origo of b to be at the center of the it (and not in the corner as shown in figure 31). $a \cup b$ denotes the mask operation (see section 3.2.1). The dilation and erosion are performed for every pixel in the image; the operations are expressed as:

- Dilation of a with b: $a \oplus b$ every voxel $[i, j, k]$ is replaced with maximum value of the voxels of $a \cup T_t(b)$ where translation vector $t = [i, j, k]$.
- Erosion: $a \ominus b$ every voxel $[i, j, k]$ is replaced with the minimum value of the voxels of $a \cup T_t(b)$ where translation vector $t = [i, j, k]$.
- Opening: $a \circ b = (a \ominus b) \oplus b$. Opening is an erosion followed by dilation.
- Closing: $a \bullet b = (a \oplus b) \ominus b$. Closing is a dilation followed by erosion.

The dilation/erosion is the maximum/minimum value of $a[i, j, k]$ in a region coincident with the b when the origo of the b is at $[i, j, k]$; this is applicable to both binary and gray value images. In addition to standard operations, we define a top-hat transform:

- White top-hat: $a - (a \circ b)$
- Black top-hat: $(a \bullet b) - a$

The white *top-hat transform* produces an image containing those areas of a that are "smaller" than b and brighter than its surroundings. The black top-hat transform produces an image containing those areas of a that are "smaller" than b and darker than its surroundings.

The effect of erosion is to shrink the object by one layer defined by the structuring element and the effect of dilation is to enlarge the object. If an object in the image is smaller or same size than structuring element it will disappear when eroded. Dilation is associative and commutative while erosion is not. The size of the structuring element or the number of times the operation is performed in succession affect the operation. An example of using the morphological operations would be extraction of borders of the image $B_{\text{in}}(a) = a - (a \ominus b)$.

Distance transform

Distance transform (DT) is a binary image operation that determines the distance for all the solid voxels to the closest void voxel, and replaces the voxel value with the distance; see figure 33 for an example. The end result is called distance map. To perform distance transform the voxels in image a are divided into two classes: object O and background B. Consider two 3D points $\mathbf{v}$ and $\mathbf{q}$. Each object voxel is labelled with the distance between the voxel and the nearest background pixel:

$$a[\mathbf{v}] = \begin{cases} 0 & \text{if } \mathbf{v} \in \{B\}, \\ \min(\mathbf{q} \in \{B\} ||\mathbf{v} - \mathbf{q}||_p) & \text{if } \mathbf{v} \in \{O\}, \end{cases}$$

where distance norm can be selected as:

- Euclidean l_2-norm.
- City block, or Manhattan metric uses l_1-norm norm; the distance is the sum of axis-oriented pixels between the points. This over-estimates the distance as the diagonal distances are calculated as sums of steps.
- Chessboard metric is defined as $||[i,j,k] - [i_2, j_2, k_2]||_\infty = \max(|i - i_2|, |j - j_2|, |k - k_2|)$. This metric underestimates the diagonal steps as they are approximated as 1.
- Many other metrics exist, as one example a hybrid meter aims to combine the city block and chessboard by averaging them: $||\mathbf{v} - \mathbf{q}||_{\text{hybrid}} = \frac{1}{2}(||\mathbf{v} - \mathbf{q}||_1 + ||\mathbf{v} - \mathbf{q}||_\infty)$.
- A weighted distance transform [20, 230] uses a weight window, called a Chamfer mask, to propagate the approximate of distances to cover the whole object.

There are various fast algorithms for distance transform. Some of them are approximations and some of them are exact euclidean distances. Two pass algorithm [33] walks through the voxels two times and along its way propagates the distance information from the previously calculated known distances to the new voxels by weighting the distances according to their direction. The result is an approximation of the euclidean distance, and it works in linear time. Vector propagation algorithm [51] propagates distances, starting from the edge, until the whole object space is covered. The result is euclidean distance map but might contain some miscalculations in certain voxel configurations; method works in linear time.

For exact euclidean distance transform (EDT), the vector propagation method is efficient for large 3D data sets [51]. The vector propagation algorithm is presented in Algorithm 1.

FIGURE 33 A binary image of a leaf (on the left) and its distance transform (on the right). The darker colors depict longer distances.

Algorithm 1 Vector propagation distance transform

```
Initialization: Set the void space to have infinitum distance to solid. Find border voxels $V = B_{\text{out}}(B)$.
For each $\mathbf{v} \in V$ find the neighbouring void voxels $V_N = \{\mathbf{q} \in \mathcal{C}_n[\mathbf{v}] \mid \mathbf{q} \in B\}$ and associate these voxels with the information of the closest border voxel.
while $V_N$ is not empty do
Take $\mathbf{v} \in V_N$, for each $\{\mathbf{q} \in \mathcal{C}_n[\mathbf{v}] \mid \mathbf{q} \in B\}$
    Calculate the distance between neighbouring voxel $\mathbf{q}$ and the border voxel associated with $\mathbf{v}$.
    If the distance is smaller than the already existing value in $\mathbf{q}$, replace the value with the smaller one and add $\mathbf{q}$ to $V_N$.
end while
```

Skeleton

The skeleton is a one-pixel-thick representation of a shape that follows the center line of the shape (that is equidistant at the borders of the shape). The skeleton can be made for binary / labelled image. For 2D objects the skeleton is a one dimensional line. For 3D objects the skeleton is either a surface (surface skeleton) or a single line (a curve skeleton is also in some cases called *medial axis*). They tend to preserve the geometrical and topological (connectivity, length, direction) properties of the shape.

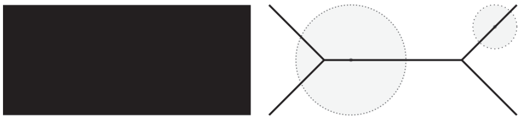

FIGURE 34 A square object (on left) and its skeleton (dark line) with few maximum balls shown.

The aim of the skeletonisation is to provide a simpler presentation of the object in the image, which still contains the geometry and topology of the original object.

The most common procedure for creating a skeleton is thinning, which is erosion, layer by layer, until only the skeleton is left. A *simple point* is a point whose deletion does not change the topology of the object [123]. There are various strategies for performing the thinning. In sequential thinning one (simple) point is removed at each iteration. In parallel thinning several points can be deleted in one iteration. More details for example in [266].

Skeletons are sensitive to noise and often have a lot of unnecessary branches. The method for removing the unwanted branches is called pruning.

Granulometry

Granulometry is a morphology-based method for determining size distribution of objects in a binary image. It is based on subsequent series of opening operations with enlarging structuring element s and calculation of the image integral (volume) in between the operations. The enlarging structuring element is defined as:

$$s_t = \underbrace{s \oplus \ldots \oplus s}_{t \text{ times}}.$$

Now if a is the binary image to be analysed the series of opening operations is

$$\gamma_t(a) = a \circ b_t.$$

The granulometry function that defines the volumetric change in between the consecutive opening operations is defined as:

$$G_t(a) = M_{000}(\gamma_t(a)).$$

M_{000} is calculated as in equation (19). The size distribution of b is now given by:

$$PS_t(a) = G_t(a) - G_{t+1}(a),$$

where t refers to the size of the object. The result is statistical approximation of the size distribution.

3.3.3 Direct voxel processing

Flood fill is an algorithm to determine similar areas or volumes in an image. The area needs to be connected by some similarity rule, commonly gray value. The principle of the algorithm is the following: 1) algorithm is initialized by adding manually or by some heuristic seed voxels to set V, 2) while $B_{\text{out}}(V)$ contains voxels that fulfil the similarity rule they are added to group V. We may choose the similarity to be exactly one gray value or a range of gray values.

The flood fill is a simple algorithm where only the voxel neighbourhood and the implementation of the algorithm affects the end result and effectiveness [135] [77]. However, with large images the efficiency and memory consumption differs between the implementations. So-called scanline method [65] is more optimized for its memory consumption and speed, by filling the space by lines storing only the start points of the lines instead of each individual pixel, thus consuming less memory.

The flood fill algorithm can be utilized to find local maxima of an image. The simple algorithm to find local maxima is to use flood fill to find localities in an image that are not bordered by any voxels with gray values larger than the value in locality, i.e, derivative of the area is zero of negative. That is, we have a set of voxels V defined by the flood fill in image a, if $\forall \mathbf{v}_1 \in V$ and $\mathbf{q} \in B_{\text{out}}(V) : a[\mathbf{v}_1] > a[\mathbf{q}]$ area V is a local maximum. Every voxel need to be accessed only once. However, a problem with the natural images is that they contain noise. The simple algorithm finds all the local maxima. For noisy images, the noise will cause a large number of non-real maxima. An efficient solution to this problem is geodesic reconstruction introduced by Vincent Luc 1993 [253]. The idea is to flatten the top of a local maxima by using geodesic dilations (see Algorithm 2).

Algorithm 2 Geodesic reconstruction

```
Let's consider we have an image $a$, we define $a_h = F - h$ (we subtract voxel-wise the value $h$ from the gray values of $a$).
while The resulting image does not change do
    The geodesic reconstruction step: $\rho_G^{(n)}(F) = \sigma_G \circ \sigma_G \circ \ldots \circ \sigma_G(F)$, where $\sigma_I(G)$ is an elementary geodesic dilation of $G$ "limited" by $I$: $\sigma_I(G) = (G \oplus b)(x) \bigwedge I$, where $b$ is the structuring element (see gray scale dilation), $\bigwedge$ is a point wise minimum.
end while
```

As a result we get an image where each local maximum is flattened by the parameter h, now the local maxima can be found using the original simple algorithm on the flattened image, or by subtracting the flattened image from the original one and threshold this; see figure 35.

FIGURE 35 A 2D example of the geodesic reconstruction. On the left the black line represents the original image, and the gray area is the G. In the middle the algorithm 2 has been applied to G; the lighter gray areas are filled by the reconstruction. And on the right is the difference between the original and reconstructed G.

3.3.4 Transformations

Transformations are used to rotate or scale the data into a position required by the analysis or to crop the image into a more convenient size for analysis.

Interpolation

Interpolation refers to a method for defining an intensity value for any real valued (not voxel index) coordinate in the image. There are several schemes that can be used to select the value. The most simple is the nearest neighbour interpolation; the real value coordinate is rounded to the closest voxel index. This method is fast but loses details. A bit more advanced method is linear interpolation [159]. In linear interpolation, an "interpolation cube" is placed around the given point such that one vertex is at the nearest neighbour, the new value is a linear combination of the 8 neighbouring voxels as shown in image figure 36. This type of interpolation provides adequate quality while being easy to implement and is computationally fast. However, it does not provide a continuation of the interpolation function along two adjacent voxels. Tricubic interpolation is the simplest interpolation method that also provides the continuation; see [116] and [134]. Various different interpolation methods have been proposed, however, all the methods produce some kind of artefacts (see figure 37 for example) and thus, it is recommendable to avoid excess rotation or scaling.

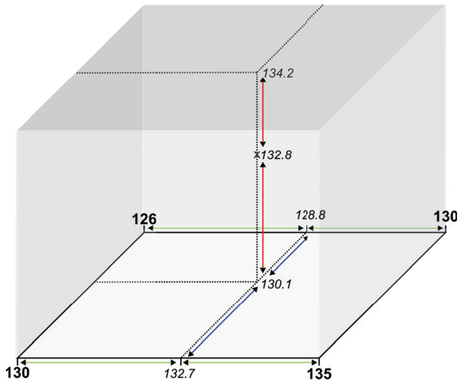

FIGURE 36 The schematic of linear interpolation. In 3D the interpolation is performed as series of three linear interpolation. First the interpolation is performed along the X-axis, then the Y-axis and finally along the Z-axis (note that for the sake of simplicity the lines are not drawn at the top of the voxel).

Rotation

In principle, the rotation of a digital image is done voxel by voxel. We consider a vector that goes from the center of the image to the voxel being processed. This vector is multiplied by a rotation matrix to find its new orientation. In three dimensional space the rotation matrix is formed of three components:

$$R_x(\gamma) = \begin{bmatrix} 1 & 0 & 0 \\ 0 & \cos\gamma & -\sin\gamma \\ 0 & \sin\gamma & \cos\gamma \end{bmatrix}$$

$$R_y(\beta) = \begin{bmatrix} \cos\beta & 0 & \sin\beta \\ 0 & 1 & 0 \\ -\sin\beta & 0 & \cos\beta \end{bmatrix} \tag{22}$$

$$R_z(\alpha) = \begin{bmatrix} \cos\alpha & -\sin\alpha & 0 \\ \sin\alpha & \cos\alpha & 0 \\ 0 & 0 & 1 \end{bmatrix}.$$

Here $R_x(\gamma)$ defines the rotation around the x-axis at angle γ, $R_y(\beta)$ defines the rotation around the y-axis, and $R_z(\alpha)$ defines the rotation around the x-axis. These can be combined into one single rotation matrix by multiplying them together:

$$R = R_x(\gamma)\, R_y(\beta)\, R_z(\alpha), \tag{23}$$

where the origo of the rotation is at the center of the image (translation is required if otherwise). Now to rotate the image a we create a new image called a_r (that is the rotated image), we walk through every voxel $\mathbf{v}$ in a_r and define its gray value from the original non-rotated image: $a_r[\mathbf{v}] = a(R\mathbf{v})$. The voxel value is defined using interpolation if not at the exact pixel location.

3.4 Image Preprocessing

Image preprocessing is a phase where the image is modified into a form where it is most convenient to further process. This phase involves cropping, rotating, rescaling, reslicing, gray value scaling, denoising, etc. The aim is to reduce the size of the image to make it faster to perform operations. There are several possibilities for decreasing the image size. Cropping the non-informative parts of the image is an effective way to reduce the file size. The bit-depth of the image affects its memory consumption and one should consider the lowest possible bit-depth that is suitable for the analysis. In the case lower resolution shows enough details, the image can be scaled to a smaller size.

Image rotation is a common preprocessing task. If a cubical sample has not been exactly aligned to the rotation axis of the scanner it appears to be tilted in the reconstruction. This hinders the cropping of the sample. In addition some analysis methods are position-sensitive and require proper alignment of the image. Unless the rotation is multiplication of 90 degrees, it requires interpolation that degrades the image quality. In figure 37 we compare results of interpolation methods after multiple consecutive rotation operations. The quality differences are obvious. Rotations of 90 °, 180 °, and 270 ° can be done by rearranging the pixels (reslicing), and it does not affect the image quality. When necessary to rotate the image it is best to minimize the number of rotations.

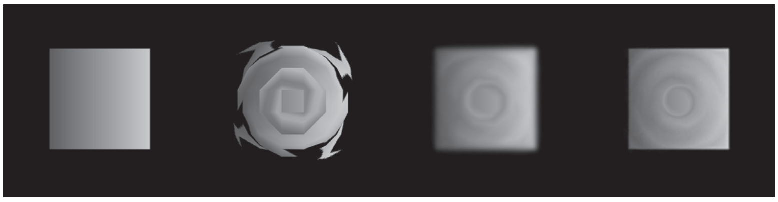

FIGURE 37 An example of an iteratively rotated image of 360 degrees with steps of 1 degree. On the left the original image, nearest neighbour (2917 ms), bilinear(4587 ms) and bicubic (25657 ms) respectively. The value inside the brackets is time the process took on Intel i7-2600 CPU with 16GB of RAM.

In practice, manual 3D rotation is difficult as it is not easy to find the exact rotation angles around each axis. A more visual way is to rotate the image slice-wise in each direction; the *reslice* operation allows change between rotation axes.

Another way is to consider some sort of automatic rotation. For planar samples it is possible to find the upper surface (V_{Surf}) of the material. A plane $Ax + By + Cz + D = 0$ can be fitted into this surface by finding $A, B, C,$ and D that minimize the equation $E = \sum_{[i,j,k] \in V_{Surf}} (k - \frac{Ai+Bj+D}{-C})^2$. By solving the least squares problem we can find the most fitting, plane and the normal vector of this plane defines the rotation angles around the x and y -axes.

Sometimes it is necessary to find an optimal rotation/translation, *rigid transform*, to match one image into another. That is, for example, if you have taken an image that you want to digitally compare with another and they need to be in the same position. At first you need to use some automatic or manual method to find (at least) three points that are the same in both images. The optimal solution is then found using the Kabsch algorithm [107]. It in practice solves following problem: $b = R * a + t$, where R is the rotation and t is the translation applied to image a to align it with image b. The algorithm is explained in more detail in Algorithm 3.

Algorithm 3 Kabsch algorithm

```
1: Find the centroids of both data sets using the method presented in equation (20). We name them $a_c$ and $b_c$.
2: Find the optimal rotation using Singular Value Decomposition (SVD). First compose matrix $\mathbb{H} = \sum_{i=1}^{N} (\mathbf{v}_{a_i} - a_c)(\mathbf{v}_{b_i} - b_c)$, where $\mathbf{v}_{a_i}$ and $\mathbf{v}_{b_i}$ are the corresponding points in images $a$ and $b$, respectively. Solve the SVD: $[U, S, V] = SVD(H)$. Now the rotation matrix $R = VU^T$.
3: Check for reflection (SVD sometimes returns a reflected case of the rotation and it does not work). If the determinant of $R$ is negative, multiply the third column of the $R$ by -1.
4: Find the optimal translation by $t = -Ra_cb_c$.
```

The rotation matrix R corresponds to the rotation matrix of equation (22) and is applied in a similar way.

4 DENOISING

Noise is one artefact (see section 2.6) that cannot be fully removed by the image acquisition system. Denoising is a process where the noise of the images is reduced using some heuristic computational method. Denoising is very often the first step on the way to segmentation and image analysis.

Standard techniques for noise reduction include linear filters like Gaussian filter [80], rank filters like median filter [202] and transform-based filters like low- and high-pass filters. While these classical methods are computationally very fast, they tend to perform poorly if an image contains sharp edges or small details. More precisely, linear and statistical methods tend to smooth edges out and diminish small details, whereas transform-based methods suffer from ringing effects (so-called Gibbs' phenomena) near edges. On CT-imaging one common denoising method is median filter (like in [268, 103, 2, 147]). However, it has undesirable properties of removing small details, producing staircase-like structures [111, 112] and combining objects that are close to each other, and those can be important especially when utilizing CT imaging in material research. Some edge preserving denoising methods, e.g., PDE-based [39, 114, 113, 110, 78, 168] and statistical [91] methods and methods based on anisotropic diffusion [126], have therefore been proposed. From the viewpoint of CT-imaging the benefit of these methods is good denoising properties and the property of preserving the volume of the objects, but it comes at the cost of computation time and memory need.

Each denoising method has its own properties. We compare here the methods by their denoising quality, computational efficiency, and usability. In practice no method has been perfect on every aspect, instead each method usually shines in one or two properties but lacks on the third. This is visually depicted in figure 38.

4.1 Denoising of CT images

CT images have few properties that affect performance requirements of algorithms. Images are in 3D and are usually large, possibly tens of gigabytes in file size. An image is almost always piecewise constant, i.e., material is often composed of homogeneous areas

FIGURE 38 The requirement triangle of an denoising algorithm.

of constant gray value. Heterogeneous materials are composed of two or more materials in the form of grains, fibres, particles, etc. There rarely exist short gradients, except in artefacts. Gradients are usually fast caused by sharp shifts from one material to another. Beam hardening, edge softening, ring artefacts or partial volume effect can cause slow gradients. Some of them can be removed by changing the imaging conditions, but it usually means longer scanning time, which can be limited. The edge quality of a CT reconstruction depends on many variables. In parallel beam geometry the edges appear sharper than in cone beam systems, where the half shadow effect reduces the edge quality (see equation (1)). The noise type of the final output is hard to predict; the projection images contain both, multiplicative (due to the signal gain) and additive noise [219], but after reconstruction the noise properties are not the same [157]. The noise properties depend also on imaging conditions and sample properties, on high contrasting samples low frequency Gaussian-type noise is typical. On low contrasting samples, a speckle type of noise is more dominant.

The practical limitations favours algorithms that perform in a filter-like manner, i.e., only a local area around the voxel to be denoised is required to get the results. Such classical algorithms are mean, Gaussian and median filters. They are fast and easy to use, while the result usually has some unwanted properties. For more computation-demanding algorithms anisotropic diffusion and bilateral filtering are popular and well studied algorithms also used in tomography [196, 246]. They also have a tendency to sharpen the edges of an image. In addition, we have studied the variance weighted mean filter, which is a computationally relatively light weight edge-sensitive denoising algorithm. In some cases the quality outweighs the computational demands; sliding Cosine transform [201, 64] is computationally demanding while the denoising abilities are claimed to be good. Mean shift is computationally demanding but is also effective at sharpening the edges. We compare this group of denoising algorithms that we consider effective for various needs in X-ray image processing.

A few promising methods were left out of the comparison due to the lack of suitable implementation or performance issues. Non-local means [38] is based on an idea of averaging all the voxels in the image - instead of just voxels surrounding the target voxel - with weights obtained from the similarity of the neighbourhood of the voxels. However, as such, the algorithm is extremely computation demanding and optimization is required. We tested the algorithm found at Avizo-fire software, but for large datasets, used in this work, the processing was too slow, in order of days. BM4D [152] is an extension of non-local means, with a potential to be an excellent method for pure noise removal of tomographic images. According to [152] the processing of a 3D image of size of 181x217x181 took 11 minutes, which is over double the time the slowest method tested here is consuming. Yet, the method look promising and should be considered when the computational capabilities increase. Also, we consider the DCT-based method to give similar results (although the noise removal performance is a bit worse) to the BM4D [154, 152] and, thus, can be used as a reference to measure the performance of the method against XμCT images.

4.1.1 Convolution-based methods

In discrete form, convolution of two images a and b in 3D is as follows:

$$(a * b)[i,j,k] = \sum_{l=-\infty}^{\infty} \sum_{m=-\infty}^{\infty} \sum_{n=-\infty}^{\infty} a[l,m,n] \cdot b[i-l, j-m, k-n]. \tag{24}$$

Convolution is a weighted average of the image a at every location $[i,j,k]$, where the weighting is given by $b = g[i-l, j-m, k-n]$ (g usually has a much smaller support and is called a kernel). The convolution operation shifts the kernel to each voxel location $[i,j,k]$ and performs the weighting operation. As such, this is a slow operation. A common way to speed up the convolution with large kernels is to perform it in Fourier space [223]. Fast Fourier transform (FFT) can be performed in $\mathrm{O}(N \log N)$ time [70]. The Fourier theorem states that convolution of signal f with g is the same as taking the FFT of both signals and multiplying them. See [80] for more details. Convolution can be used in many processes such as denoising, sharpening, edge detection, etc. Convolution with a delta-peak (discrete image terms an image with singe voxel having value 1) will translate the image by the vector from the center of the image to the delta peak location [223].

Mean and Gaussian filters are the simplest type of filters. The idea of these filters is to replace the value of the denoised voxel with the weighted average of its surrounding voxels. They can be used to remove noise in the image, but they will also diminish small details from the image. Both filters are based on convolution of the image with a certain kernel. For N-dimensional Gaussian filter, the weights for the kernel are defined by Gaussian function:

$$g(\mathbf{v};\sigma) = \frac{1}{(\sqrt{2\pi}\sigma)^N} e^{-\frac{||\mathbf{v}||_2^2}{2\sigma^2}}, \tag{25}$$

where σ defines the variance of the filter, the larger the sigma more blurring is obtained. For mean filter, the kernel is even simpler; the value of the voxel is replaced by a mean value of the voxel neighbourhood. The mean and Gaussian filters are not particularly good at noise removal, but they have other applications in image processing and can be used as building blocks for more sophisticated applications. In addition, the mean filter has a negative effect of producing a stopband characteristic with many sidelobes [216]. However, it has been shown that similar results to the Gaussian filter can be obtained by applying a cascade of box filters [216], thus resulting in a fast implementation of Gaussian filter. The standard deviation σ of the Gaussian filter when using a cascade of n box filters with window size T is [216]:

$$\sigma = \sqrt{\frac{nT}{12}}.$$

Both Gaussian and mean filters have the useful property of being separable. This means that an n-dimensional kernel can be expressed as an outer product of n 1-dimensional vectors. This also means that instead of convolution with a full n-dimensional kernel we convolve n-times with a 1-dimensional kernel. The benefit is a speed-up in processing as the amount of calculations per voxel is much less. For example with a 2D kernel of size of 5x5, 25 calculations per pixel are originally needed, whereas with separated 5x1 and 1x5 kernels only 10 calculations per pixel are done.

4.1.2 Median filter

Median filter is a classical rank-based filter that is good for removing salt and pepper noise. It assumed to preserve edges better than Gaussian or mean filters on low-noise images [8]. The median filter replaces the denoised voxel intensity value with median value of the voxel intensities in some neighbourhood of the voxel. Naturally, due to its definition, if the size of an object in the image is less than half the size of the filtering neighbourhood it will disappear.

Median filtering is a slow process compared to linear filtering. The process can be sped up using accumulation schemes and histogram-based determination of the value of the center rank [96]. To find a median value from the histogram, a cumulative histogram of the voxel locality is defined (see section 3.3.1); median value can be found at the center bin [149]. At the next voxel location, the histogram can be updated using the accumulation method.

One parameter is used in this scheme:

- spatial parameter r is the radius of neighbourhood

4.1.3 Bilateral filter

Bilateral filter (BF), discussed in more detail in [234], can be presented with the following equation:

$$a(\mathbf{v}) = \frac{1}{w(\mathbf{v})} \int_{-\infty}^{\infty} \int_{-\infty}^{\infty} a(\mathbf{q}) \cdot w_s(\mathbf{q}, \mathbf{v}) \cdot w_r(a(\mathbf{q}), a(\mathbf{v})) \mathrm{d}q, \tag{26}$$

with the normalization coefficient

$$w(\mathbf{v}) = \int_{-\infty}^{\infty} \int_{-\infty}^{\infty} w_s(\mathbf{q}, \mathbf{v}) \cdot w_r(f(\mathbf{q}), f(\mathbf{v})) dp. \tag{27}$$

The denoising effect is obtained using a similar approach as, e.g., in mean filter or Gaussian filter: The surrounding voxels are averaged with certain (non-uniform) weights. The double integral in equation (26) means the filter works in both spatial domain and range domain. In spatial domain the weighting is obtained from $w_s(\mathbf{q}, \mathbf{v})$, the function w_s measures the closeness of the point $\mathbf{q}$ to the point $\mathbf{v}$ to be denoised. On codomain the weighting obtained $w_r(a(\mathbf{v}), a(\mathbf{q}))$, is the similarity in gray value. As the weights depend on the similarity properties at the locality, they can not be predicted and normalization has to be incorporated.

In discrete form the filtering of image a can be expressed as:

$$a_{\mathrm{bf}}[\mathbf{v}] = \frac{1}{w[\mathbf{v}]} \sum_{\mathbf{q}_i \in \mathcal{N}[\mathbf{v}]} a[\mathbf{q}_i] \cdot w_s(\mathbf{v}, \mathbf{q}_i) \cdot w_r(a[\mathbf{v}], a[\mathbf{q}_i]),$$

where $\mathcal{N}[\mathbf{v}]$ is a window centred to $\mathbf{v}$, W as in equation (27). The w_s and w_r can be any functions but most often Gaussian function (see equation (25)) is used for both:

$$\begin{aligned} w_s(\mathbf{q}, \mathbf{v}) &= g(||\mathbf{q} - \mathbf{v}||_2; \sigma_s), \\ w_r(a(\mathbf{v}), a(\mathbf{q})) &= g(||a(\mathbf{v}) - a(\mathbf{q})||_1; \sigma_r). \end{aligned} \tag{28}$$

Two parameters are used in this scheme:

- The spatial parameter σ_s, the larger features get smoothed when σ_s is increased.
- The range parameter σ_r affects the edge sensitivity. As σ_r increases the bilateral filter gradually approaches Gaussian convolution, removing the edges more.

4.1.4 Mean shift

Mean shift (MS), introduced in [47], works similarly to bilateral filter; weighting is performed in both spatial and co-domain. The key idea of the mean shift filter is to apply a kernel density estimator in order to iteratively search the mode of the gray values closest to the voxel currently inspected. The algorithm works in feature space that combines the gray values and the coordinates to 4D space (for 3D images). At each data point a window around it is defined and the center of mass of the values inside the window is calculated. The window is then shifted to the center of mass. This is repeated until the shift is small. The resulting gray value is then put into the spatial location of the original starting point.

So in 3D for each voxel $\mathbf{v}$ in image a we have a 4D vector $\mathbf{h}^t = [x^t, y^t, z^t, I^t]$, t represent the current time step. The system is initialized as $\mathbf{h}^0 = [\mathbf{v}, a[\mathbf{v}]]$. We iterate the following:

$$\begin{aligned} x^{t+1} &= \frac{\sum_{\mathbf{q} \in \mathcal{N}[x^t, y^t, z^t]} x^t \cdot m(\mathbf{h}^t, \mathbf{q})}{\bar{m}}, \\ y^{t+1} &= \frac{\sum_{\mathbf{q} \in \mathcal{N}[x^t, y^t, z^t]} y^t \cdot m(\mathbf{h}^t, \mathbf{q})}{\bar{m}}, \\ z^{t+1} &= \frac{\sum_{\mathbf{q} \in \mathcal{N}[x^t, y^t, z^t]} z^t \cdot m(\mathbf{h}^t, \mathbf{q})}{\bar{m}}, \\ I^{t+1} &= \frac{\sum_{\mathbf{q} \in \mathcal{N}[x^t, y^t, z^t]} I^t \cdot m(\mathbf{h}^t, \mathbf{q})}{\bar{m}} \text{ and} \\ \bar{m} &= \sum_{\mathbf{q} \in \mathcal{N}[x^t, y^t, z^t]} m(\mathbf{h}^t, \mathbf{q}) \end{aligned} \tag{29}$$

where $m(\mathbf{h}^t, \mathbf{q}) = g(\frac{|x^t - \mathbf{q}_x|^2}{w_x^2}) g(\frac{|y^t - \mathbf{q}_y|^2}{w_y^2}) g(\frac{|z^t - \mathbf{q}_z|^2}{w_z^2}) g(\frac{|I^t - a[\mathbf{q}]|^2}{g_x^2})$ and $g(x) = \exp(-x)$. The final I^t is the denoised gray value to be put to the $a[\mathbf{v}]$.
Three (+1) parameters are required:

- Parameters w_x, w_y, w_z affect the spatial sensitivity and in general are all the same, thus considered here as one parameter w_s.

- w_I affect to the edge sensitivity
- Neighbourhood $\mathcal{N}_r^p[\cdot]$ has an effect to the denoising result. The r is a parameter for the user; p can be selected at the implementation.
- (Number of iterations or some other stopping criterion can be implemented in the code.)

4.1.5 Anisotropic diffusion

Anisotropic diffusion (AD), first introduced by Perona and Malik in [182], is a generalization of diffusion process in such a way that it allows diffusion direction to be dependent on the edges in the image. Gaussian filtering or generalized Weierstrass transform can be considered as a diffusion process with a constant diffusion in all directions [257]. In anisotropic diffusion the diffusion does not happen through edges (defined by parameters) in the image, thus, smoothing only the constant areas between the edges. For voxel $\mathbf{v}$ in an image, the anisotropic diffusion is as follows:

$$\frac{\partial f^t(\mathbf{v})}{\partial t} = \nabla \cdot \left(c^t(\mathbf{v}) \nabla f^t(\mathbf{v})\right),$$

where ∇ denotes the gradient, $\mathrm{div}(\cdot)$ is the divergence operator, $c^t(\mathbf{v})$ provides the diffusion coefficients at coordinate $\mathbf{v}$ at time t. The index t denotes that the system is being iterated over time. The diffusion coefficient is usually a function of the gradient image as it preserves the edges well. Most commonly

$$c\left(||\nabla f||\right) = e^{-(||\nabla f||/K)^2} \quad \text{or} \quad c\left(||\nabla f||\right) = \frac{1}{1+\left(\frac{||\nabla f||}{K}\right)^2},$$

where the K controls sensitivity to the edges.

Following Perona and Malik [182], the basic discrete 3D formulation of denoising image a of the process is the following:

$$a_{ad}^{t+1}[\mathbf{v}] = a_{ad}^{t}[\mathbf{v}] + \lambda \omega[\mathbf{v}], \tag{30}$$

where the content of the $\omega[\mathbf{v}]$ depends on the dimensionality and discretisation of the Laplacian operator. For $\mathcal{C}_6[\mathbf{v}]$ it can be written as:

$$\begin{aligned} \omega[\mathbf{v}] = c_n^t[\mathbf{v}_n] \cdot \Delta_{[1,0]}^{y} a[\mathbf{v}] + c_s^t[\mathbf{v}_s] \cdot \Delta_{[0,1]}^{y} a[\mathbf{v}] + c_e^t[\mathbf{v}_e] \cdot \Delta_{[1,0]}^{x} a[\mathbf{v}] + \\ c_w^t[\mathbf{v}_w] \cdot \Delta_{[0,1]}^{x} a[\mathbf{v}] + c_u^t[\mathbf{v}_u] \cdot \Delta_{[1,0]}^{z} a[\mathbf{v}] + c_d^t[\mathbf{v}_d] \cdot \Delta_{[0,1]}^{z} a[\mathbf{v}], \end{aligned} \tag{31}$$

where subscriptions n, s, e, w, u, and d refer to the neighbouring voxels north (j+1), south (j-1), east (i+1), west (i-1), up (k+1), and down (k-1) respectively, for example, $c_n^t[\mathbf{v}] = c(||\nabla a^t[i, j+1, k]||)$. The gradient can be calculated as shown in section 3.2.3. Equation (30) takes into account only the N_6 neighbourhood where distance between the neighbouring voxels is 1. If N_{18} of N_{26} are used the distances ($\sqrt{2}$ for edge connected voxels and $\sqrt{3}$ for corner connected voxels) are used as weights for the ωs.

Two parameters are required:

- K controls the sensitivity to the edges.
- Number of iterations adjust the smoothing efficiency.

4.1.6 Variance weighted mean filter

The principle of variance weighted mean filter (VaWe) uses local variance to give weights for the window of a mean filter [80] (pp. 239-240). Variance is assumed to correlate with the smoothness of the inspected area. A low variance is interpreted as a flat area and high variance indicates an edge. A lower weight will be given to areas with high variance and vice versa. Filter can be described with the following equation:

$$a_{vw}[\mathbf{v}] = a[\mathbf{v}] - \frac{\sigma_\eta^2}{\sigma_l^2}(a[\mathbf{v}] - \mu),$$

where a is the image to be filtered, σ_η^2 is a parameter that describes the maximum variance of the noise to be removed, $\sigma_l^2 = \mathrm{Var}(\mathcal{N}_r^p[\mathbf{v}])$ and $\mu = \mathrm{Ave}(\mathcal{N}_r^p[\mathbf{v}])$ denote the variance and average of a voxel neighbourhood as defined in section 3.2.2. A square neighbourhood ($p = 1$) can be used with user selectable radius r. When the local variance is close to noise variance, there are no edges in the locality and the value of a voxel is replaced with the mean of the locality. If the variance is high, i.e., there is edge in the locality, the value of the voxel remains untouched. By using larger neighbourhood the filter can be set to filter more grainy noise. More smoothing can be gained by using several passes with different window sizes.

The method requires calculation of mean and a variance of given window size. The variance can be calculated using the formula:
$\sigma_X^2 = E[(X-\mu)^2] = E[X^2] - (E[X])^2$,
where E denotes the expected value. The mean of an image can be calculated efficiently using the scheme described in section 4.1.1. The mean of squared values can be calculated similarly. There are also few variations to note. The adaptive window size version would enlarge the calculation neighbourhood until the given variance limit is obtained. This will cause more smoothing on flat areas and less on border. The iterative version uses window size of 1 but runs multiple iterations until convergence. It can also be altered by using different statistical estimates of location and scattering around it, e.g., σ-trimming, or robust variance methods like median absolute deviation [16, 92]. The drawback of these methods is that they tend to degrade the edge detection property and therefore will not bring much benefit over the original method.

Two parameters are used in this scheme:

- The reference variance σ_η^2 can be obtained from the original image.
- The radius of the neighbourhood.

4.1.7 Sliding discrete cosine transform

Discrete cosine transform (DCT) [1] is a Fourier transform-like operation that transforms a signal into a sum of different frequency cosine functions. DCT has many applications in data compression, where, e.g., JPEG, MP3 and MPEG are using it. DCT has a property of being efficient on approximating signal with a small number of functions than many other transforms. In addition the method is used efficiently in image denoising [201, 64].

To utilize the DCT on image denoising the image is divided into overlapping voxel neighbourhoods (a window is slid over the image), whose DCT coefficients are thresholded and then transformed back to spatial space. A common selection for the neighbourhood size is 8x8x8 [105]. The values are projected to image space such that overlapping areas are weighted according to their relevance by a reciprocal of remaining non-zero coefficients. There are many variants of DCT transform while the most common is following:

$$X_k = \sum_{n=0}^{N-1} x_n \cos[\frac{\pi}{N}(n+\frac{1}{2})k], \tag{32}$$

where $k = 1, ..., N-1$ and x is the original 1-D signal. The inverse transformation is the following:

$$x_k = \frac{2}{N}(\frac{1}{2}X_0 + \sum_{n=1}^{N-1} X_n \cos[\frac{\pi}{N}(k+\frac{1}{2})n]), \tag{33}$$

The multidimensional transform is a composition of 1-D transform along each axis. To speed up the execution the cosine parts can be pre-calculated for each n and k combination. We call the method sliding discrete cosine transform (SDCT). The overall algorithm in overall is presented in Algorithm 4.

Algorithm 4 SDCT algorithm 3D

```
Create an empty result image $a_r = 0$ and an empty weight sum image $a_w = 0$.
for each 8x8x8 window $n \in a$ do
    Transform the $n$ into DCT domain using equation (32), we obtain the coefficients $X_k$.
    Threshold the coefficients: set $X_k = 0$ if $X_k < \tau$ for all $k$, where $\tau$ is user defined parameter.
    Calculate weight $w$ for the area: let $C_0$ be the number of zero coefficients in $X_k$, $w = 1/C_0$).
    Inverse transform the thresholded coefficients (equation (33)). Insert the resulted values multiplied by $w$ into the window $n$ in $a_r$. If there already exists a value at the voxel then add the new value to the old one.
    Insert value $w$ into all voxels in the window $n$ in $a_w$. If there already exists a value at the voxel then add the new value to the old one. This is for weight normalization.
end for
Normalization, $a_r \leftarrow a_r / a_w$. Now $a_r$ contains the denoised image.
```

One parameter is required:

- The coefficient threshold limit τ affects to the denoising strength.

4.2 Denoising results

Next we compare the various denoising methods in the context of actual XμCT imaging. The quantitative comparison of different denoising methods is complicated as each method has it own parameter space and characteristic behaviour. For example, any method can be tuned to smooth the noise to a very low level, but at the same time details of the image can disappear. The different methods do have their own properties that we group here roughly:

- Gaussian and mean filters are not sensitive to edges, they smooth the image evenly everywhere.
- Median filter preserves the edges better by changing its smoothing properties when passing an edge.
- Anisotropic diffusion, MS and bilateral filter adjust their smoothing kernel according to the shape of the details in the image. The edges are left intact.
- VaWe uses constant kernel, but does less denoising at the edges
- SDCT denoises the image by removing the less "important" frequencies of the noisy area and tries to leave the relevant shape.

In this section we will try to find the characteristics features of each methods and also try to gain understanding of how those properties would be beneficial in the viewpoint of XμCT. In addition, the denoising and segmentation are a close couple as the quality of denoising will have a impact on how easy (or difficult) the segmentation process will be. Thus, the following segmentation chapter will continue to analyse the effect of denoising methods on the segmentation process.

4.2.1 Denoising quality

We consider the noise in tomographic images mostly additive with the following model:

$$a = n + \bar{a}, \tag{34}$$

where a is the observed image, n is the noise and $\bar{a}$ is the true (non-noisy) image. The result of a denoising method $\hat{a}$ is an approximation of the $\bar{a}$, and an approximation of the noise $\hat{n}$ can be found by subtracting $\hat{a}$ from a. Typically this can be used to approximate the quality of the result; an optimal denoising method would produce $\hat{n}$ that contains only noise, however, all methods tend to remove some non-wanted image components that can be seen as a structure in the $\hat{n}$ as well. In XμCT the distribution of n is hard to approximate due to the multiple phases of the tomographic imaging, thus, it is not easy to create an artificial image that follows the noise model of XμCT images (see section 2.3) exactly. To overcome this problem we use two tomographic images obtained with the same parameters except for the exposure time, which was for single projection image 1 s for noisy image and 30 s for low noise reference image. Imaging time for the low quality sample was around 1 hour and for the high quality one 30 hours. A cross-sectional images of the sample data is shown in figure 39.

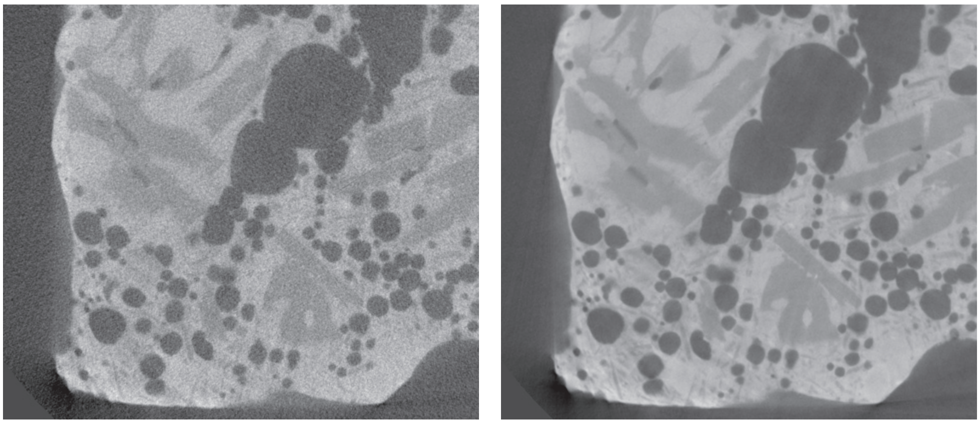

FIGURE 39 The sample images for the denoising comparison. On the left, the noisy, and on the right, the reference image.

TABLE 3 Denoising parameters found by analysing five patches (P1 to P5) and finding the parameters that minimize the difference between denoised patch and reference image.

	P1	P2	P3	P4	P5	Selected
Gaussian (σ)	1.3	1.3	1.2	1.3	1	1.22
Mean (r)	2.3	2.3	2.3	2.3	2	2.24
Median (r)	4	2.5	2.5	2.5	2	2.7
SDCT (τ)	82	77	77	78	64	75.6
BF (σ_s, σ_r)	2, 28	2, 33	2, 25	2, 33	1, 77	2, 28.6
MS (w_s, w_I, r)	10, 80, 4	10, 70, 4	10, 80, 4	10, 80, 4	40, 80, 3	10, 77.5, 4
AD (K, iters)	16, 9	15, 10	14, 9	15, 8	17, 9	15, 9
VaWe (σ_η^2, r)	4, 6	3, 7	3, 8	3, 8	3, 7	3, 7.5

To find the parameters for the denoising algorithms, we compared the denoising result of the noisy image to the reference image and tried to optimize the parameters such that most similarity was obtained. To avoid problems with edge and flat area sensitivities, we took five 100^3 patches from the object area of the image and defined the optimal parameters for each patch. The selected optimal parameter was the average over the patches, unless there was a window size parameter, when the average was calculated over the results with the most common window size (mode of the window sizes). The parameters obtained are shown in table 3.

The comparison of the denoising results is visually demonstrated in figure 40. An optimal filter would remove only the additive noise, but leave the object edges intact, thus, the residual image should show no traces of the edges. By visually inspecting the results, the SDCT image looks the best in that sense and Gaussian, mean and MS the worst. To analyse the results quantitatively, we also compare the gray value differences between

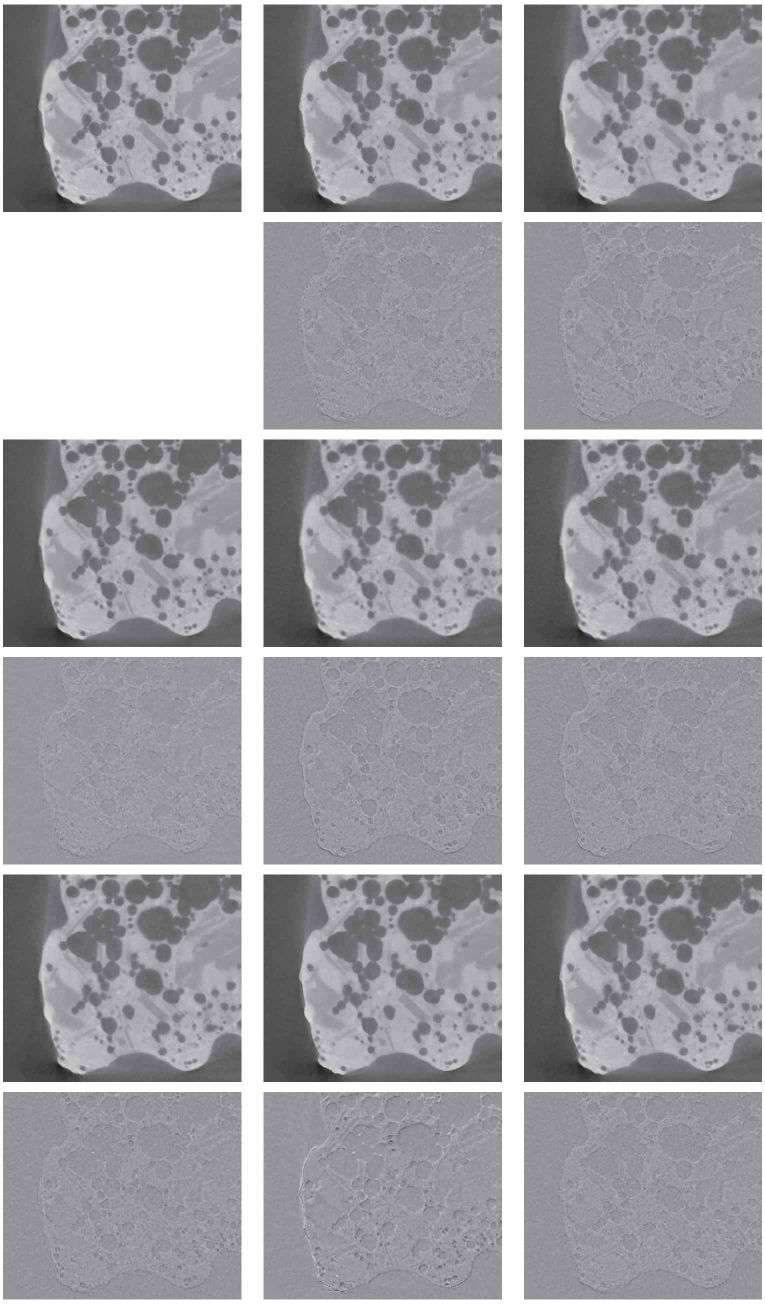

FIGURE 40 Comparison of the effect of denoising methods. The results are grouped such that at the top a normal image and below it a the noise component. From top to bottom, from left to right: reference image, AD, BF, SDCT, Gaussian, mean, median, MS, and VaWe.

all the results and reference image, similarly to [79], for the whole sample and for three different areas (one pure noise and two detail areas) depicted on figure 41. The results

TABLE 4 The average gray value difference (l_1 -norm) of the denoised results to the reference image. The results are calculated for the whole image, to the pure noisy area, and to two areas containing image details. The number in parenthesis marks the rank of the result.

	Whole image	Noisy area	Detail area 1	Detail area 2
Original noisy	6.412	4.689	8.527	8.127
AD	3.077 (5)	1.532 (5)	3.747 (7)	3.305 (4)
BF	3.025 (4)	1.490 (2)	3.712 (4)	3.340 (5)
SDCT	2.681 (1)	1.484 (1)	3.235 (1)	2.997 (1)
Gaussian	3.265 (7)	1.905 (7)	3.726 (5)	3.342 (6)
Mean	3.228 (6)	2.040 (8)	3.737 (6)	3.420 (7)
Median	2.999 (3)	1.714 (6)	3.548 (2)	3.229 (2)
MS	3.573 (8)	1.528 (4)	3.894 (8)	3.448 (8)
VaWe	2.941 (2)	1.525 (3)	3.613 (3)	3.254 (3)

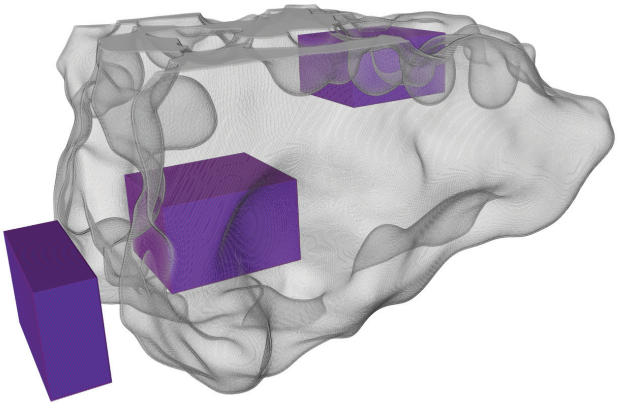

FIGURE 41 The analysis areas for the denoising test. Areas marked with dark color and the sample shape visualized in gray. The area outside the sample is to analyse the pure noise area.

are shown in table 4. Here almost all the denoising methods are performed similarly in terms of preserving the details (probably because we seek the parameters in such a way that most of the details were preserved). The results indicate that the SDCT performs best in all aspects: The noisy area is well denoised and also the detail are best preserved. Gaussian and mean filter are able to preserve the details quite similarly to the many other methods, but as the parameters are tuned to preserve the details, the noisy area is not denoised as well. Median filter shows similar performance, but being a bit better on noisy patch. AD, BF and VaWe perform similarly, denoising the detail area as well as other methods, but, in addition, the noisy area is denoised better (in comparison to Gaussian, mean and median). MS gives the worst result; the reason for this is, by inspecting the difference image, that it tends to sharpen the edges more than the other methods, thus causing large residual values at the edges (l_1-norm does not even overemphasize these). This might be a good property for image segmentation, but for pure denoising analysis it gives a bad result.

To analyse the edge behaviour of the filters more thoroughly we use sigmoid function to estimate the edge sharpness of the denoised images. The sigmoid is defined as:

$$S(x) = \frac{1}{1 + e^{-a(x+b)}}, \tag{35}$$

where a defines the slope of the sigmoid (the actual derivative at $x = 0$ is $4a$) and b defines the location of the sigmoid. In other words, a defines the steepness of the gradient between “lower part” and “higher part” of the sigmoid and, thus, the sharpness of the edge. See figure 42 for examples. We fitted the sigmoid to the edge profiles of denoised images and to the reference image; the results are shown in figure 5. The larger the a is, the sharper the edge is. In case a is larger than the value from the reference image, we assume that the method sharpens the result, if smaller it softens the edge. Obviously Gaussian and mean filter softens the edge notably. SDCT, VaWe and Median smooth the edge a bit, but keep it close to the original sharpness. AD, BF and MS sharpen the edge. MS filter sharpens the edge a notable amount. All the methods keep the edge in its original location (parameter b marginally, by less than half a voxel).

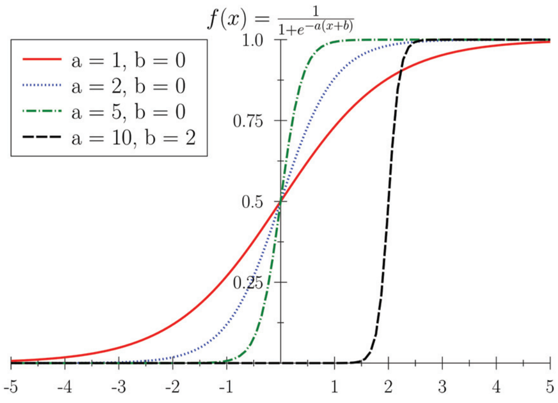

FIGURE 42 Sigmoid function.

In addition to further analyse the behaviour of the denoising method, we used a set of artificial test images with added Gaussian distributed noise with standard deviations of 15, 25, 35, 45 and 55. The test image contained a square box (value 192) over background (value 128). Each test image was denoised with each method such that CNR over 8 was obtained and edge quality was manually optimized. The results are presented in figure 43. At the low noise levels the results are similar to previous results. When the noise level is

TABLE 5 The fitting parameters of the sigmoid fitted into the denoised images. *a* defines the slope and *b* defines the location of the sigmoid. Ref refers to the reference image. The number in parenthesis marks the rank of the result.

	a	b
AD	1,347 (3)	0,002
BF	1,357 (2)	-0,008
SDCT	1,107(5)	0,020
Gaussian	0,829 (8)	0,152
Mean	0,868 (7)	0,128
Median	1,071 (6)	0,044
MS	3,168 (1)	-0,452
VaWe	1,117 (4)	0,039
Ref	1,204	0,000

increased the differences between the methods become less pronounced. And actually the Gaussian filter gives quite similar results compared to the others. The bilateral filter has an interesting behaviour as at the low noise level it performs well, but falls to the worst when noise level is increased. SDCT provides the best results at the high noise levels. We ranked the results according to the total sum of the sigmoid values: SDCT (1), MS (2), AD(3), VaWe (4), BF (5), Median (6), Gaussian (7), Mean (8).

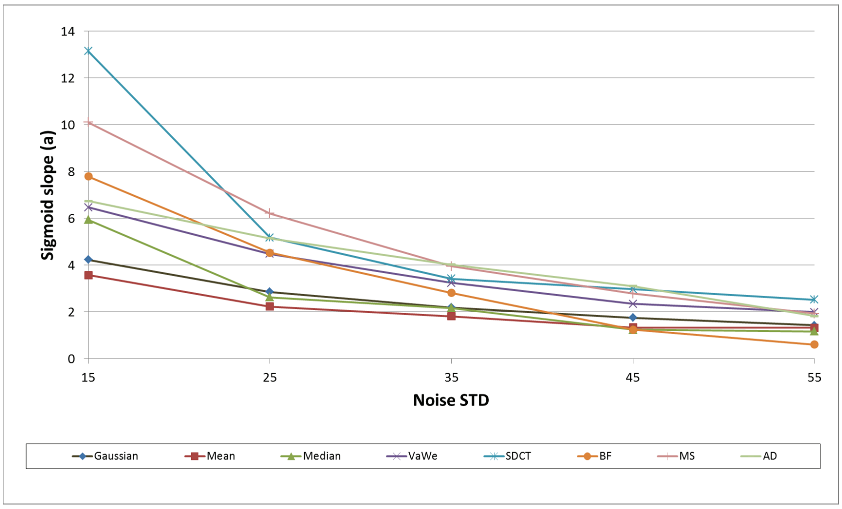

FIGURE 43 The edge preservation of denoising methods. The sigmoid slope as a function of the noise std.

4.2.2 Processing time

The processing time of the denoising methods were compared by measuring the time to process a series of images of various sizes. All methods were tuned to give same signal-to-noise ratio. The 3D Gaussian and 3D median filters were implementations from

ImageJ software [209]. The bilateral filter was ImageJ plugin called SUSAN [222]. The mean filter, VaWe, SDCT, anisotropic diffusion were implemented by the author. All realizations were multi-core implementations, however, there is probably a possibility to further optimize the codes, and these results should just be used to roughly compare the computational burden of the algorithms. In addition, anisotropic diffusion was also tested using a commercial Avizo-fire (version 7.1) software.

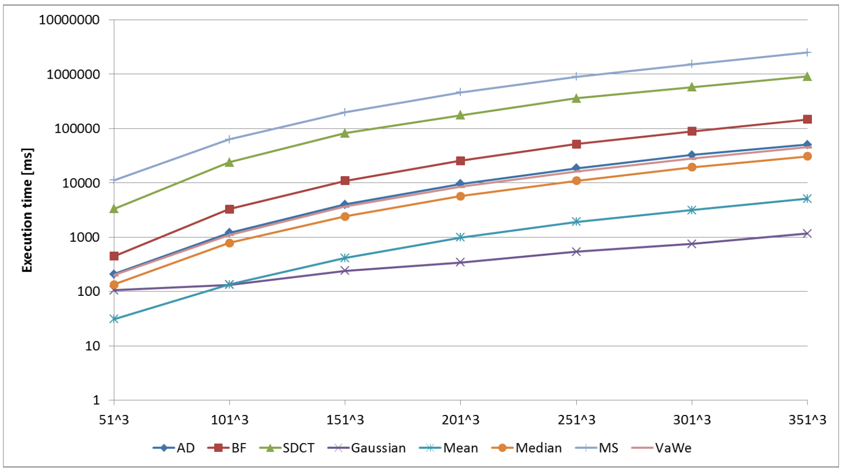

FIGURE 44 The processing time of the denoising algorithms as a function of image size.

The results are shown in figure 44. The results were calculated on a standard desktop computer (Intel i7, 16GB of memory). The simplest mean and Gaussian filters performed almost equally as quickly, being able to process even a large image (> 1024^3) while the user is waiting. The median filter, VaWe and bilateral filter form the second group, having a bit longer processing time, but still less than an average coffee break for even large images. AD is a bit more time consuming but still should process an average image in reasonable time. SDCT and MS are rather slow processes requiring a night or more to process large image. We ranked the results according to the total processing time for all sample images: Gaussian (1), Mean (2), Median (3), VaWe (4), AD (5), BF (6), SDCT (7), MS (8).

4.2.3 Usability

The usability study of such an algorithms the is hard to perform realistically and, therefore, we content ourselves with studying just the number of parameters and how well they are defined.

For all the methods having only one parameter (Gaussian, Mean, Median, SDCT), the parameters affects the strength of the smoothing and, thus, those can be considered equally good. Three methods have two parameters, namely BF, AD and VaWe. For Vawe and BF, the parameters describe the spatial size of the kernel and the edge sensitivity of the system. For AD, the parameters (gradient threshold scale and number of iterations) are not that easy to interpret. MS has three parameters. To this end we conclude to the following ranks: Gaussian (4), Mean (4), Median (4), SDCT (4), BF (6), VaWe (6), AD (7), MS (8).

4.3 Results

Most of the denoising methods are based in the a weighted average on voxel neighbourhood around the denoised voxel. The selection of which voxels to average and with which weights varies. To this end the methods can be further categorized by the selection of averaged voxels. For Gaussian, mean, median and VaWe the averaging is performed over a local non-adaptive window, thus leading into easily predictable memory consumption and computing time. The other methods have somehow adaptive collection of averaging neighbourhoods. Bilateral filter has a constant spatial window, but the weights in the gray value range make the system adapt into local shapes. Anisotropic diffusion does not have a particular window, but instead the process lets the gray values diffuse without crossing edges even from large distances as the system is iterative. SDCT differs in the sense that it does not average voxels directly but first suppresses the frequencies assumed to be noise and then averages the voxels in patches such that more weight is given to patches with no edges.

The denoising tests here indicate that in case there are details in the denoised structure, the edge-sensitive methods result in more smoothing at the flat areas while preserving the details. SDCT is the most effective in preserving the details. VaWe and median filters also performed well in this test. In addition, the edge-sensitive methods keep the edges of the structures sharper. AD, MS and BF even enhance the edges by making the gradient steeper; whether this is a benefit or not depends on application.

The usability of the methods is hard to analyse. We can consider the number of parameters and the ease with which the user can find a good parameter for the current image processing problem. Obviously for mean, median and Gaussian filters, there is only one parameter, that is, the size of the denoising kernel. As each of those methods is reasonable fast, user can quite easily test the methods and find the most suitable parameter. The response of the filters on change of the kernel size is also very predictable. In SDCT there is also only one parameter which, is also easy to determine. SDCT is, on the other hand, slower and the usability is not as high as with the simpler methods. For VaWe there are two parameters for the user to select, both of which are well defined in the problem domain and thus are quite easily determined. For anisotropic diffusion we have one parameter that defines the sensitivity to the edges and another for the number of iterations. The parameters need to be defined experimentally and, thus, it is a bit more laborious than with the previous methods. However, methods that analyse the noise properties to define the K parameter for AD exist [238]. In MS there are three parameters to be chosen, and as the method is a bit slow it is not the easiest to use to find the parameters.

The processing time of the methods can be roughly divided into three groups. The simple Gaussian and mean filters are fast and can be applied to data while waiting. The median, VaWe, AD and bilateral filters perform quite similarly and can be applied to the data while taking a short break. The SDCT, NLM, and MS are slow algorithms and

TABLE 6 Summary of denoising results. The origin 1 is table 4, 2 is table 4, 3 is table 4, 4 is table 4, 5 is table 5, 6 is figure 43, 7 is figure 44 and 8 is usability.

Origin	1	2	3	4	5	6	7	8	SUM
AD	5	5	7	4	3	3	5	7	39 (5)
BF	4	2	4	5	2	5	6	6	34 (4)
SDC T	1	1	1	1	5	1	7	4	21 (1)
Gaussian	7	7	5	6	8	7	1	4	45 (6)
Mean	6	8	6	7	7	8	2	4	48 (8)
Median	3	6	2	2	6	6	3	4	32 (3)
MS	8	4	8	8	1	2	8	8	57 (7)
VaWe	2	3	3	3	4	4	4	6	29 (2)

require usually at least overnight processing. However, maybe for efficient algorithms a slightly slower processing time can be allowed if it similarly shortens the scanning time i.e. same image quality with less scanning time (groups usually have only one XμCT scanner, but many computers. Having quick scans is in demand).

To this end, we consider the SDCT to provide the best results in terms of image quality and usability. However, the processing time is long, but there is still room for optimization (pre-calculations, GPU calculations etc.). The VaWe provides a quite usable and reasonably fast method that provides reasonable results as well. However, the VaWe is most usable in cases when the noise std is less than the difference between gray values of two neighbouring material components in the image. BF and AD are standard methods quite commonly used and are good choices if one has knowledge of the usage; however, they have the same limitation as VaWe. Gaussian, mean and median filters are fast and easy to use, but the results are not on par with the other methods. The can, however, be a effective and quick solution especially on very noisy images where the edges are already hard to locate. The overall results are summarized in table 6 to compare the results in similar way as in [203]. SDCT was the best in this comparison; we can see from the results that it is good on denoising the image in such a way that the results are close to the reference image. VaWe become the second in this comparison, and is a “Jack of all trades master of none”. AD, BF and median gave quite similar results, AD and BF being better at enhancing the smooth edges of the image. MS has a strong tendency to sharpen the edges of the image, also causing it to perform poorly on denoising tests, as the edge sharpening resulted large differences to the reference image. Gaussian and mean filter are fast, but denoising-wise, perform poorly.

5 SEGMENTATION

Segmentation is a process in which the interesting structures within an image are separated from one another. With voxel data, this typically means that each voxel is given a label that identifies the structure to which it belongs. As tomographic imaging usually focuses on analysing properties like volume, thickness, connectivity and surface area of the material, the accuracy of segmentation is essential for obtaining reliable results. Segmentation should be consistent throughout the image to ensure that, if some areas of the image are well segmented, then the other areas are, as well. It is also beneficial if the analysis result can be inspected as a function of the segmentation parameter to see how robust the segmentation method is.

Depending of the property we are interested in, segmentation can be performed in different ways. figure 45 presents a overview of the segmentation procedure.

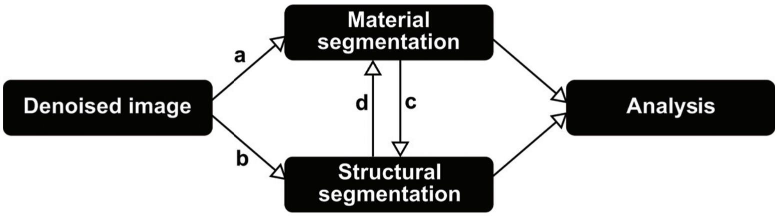

FIGURE 45 The segmentation process of a XμCT image analysis.

In figure 45, segmentation of XμCT images is divided into two categories: 1) material segmentation, where the material components (matter in a physical sense) of the image are distinguished from each other and 2) structural segmentation, where the structural components (possibly of the same material) are distinguished from each other by their shape. Path *a* refers to the methods that convert an image that has been input into an image in which each piece of matter has its own label (thresholding being the most common method). Path *b* refers to the methods that convert an image that has been input into an image in which the structural components have their own labels; region growth, level sets, and watershed are the most common methods. Path *c* defines the process of first separating the material phases and then separating the structures inside the material phases (watershed and flood fill, for example). Path *d* uses structural segmentation to detect the shape of the object and then further divides it into material components.

Material segmentation can be further divided into two categories: materials consisting of two components (typically air and some other material) or more than two components. Structural segmentation can also be divided into two groups: materials in which the structural components are either not touching (some foams for example) or are touching (fibres in papers or composites, for example). In non-touching cases, the structural segmentation is trivial; the traditional method of dividing/labelling all non-connected components is to use the flood fill algorithm (see section 3.3.3). When the structural components are touching, segmentation is usually more complicated, and solutions are often related to the characteristic shape to be restored.

Dividing an image into individual material components is achieved using methods that analyse the gray scale values of individual voxels and/or their neighbourhood. In principle, each material component can have it's own gray scale value and segmentation can be performed by choosing the gray scale value of the desired component using relatively simple tools. Segmentation into more than two phases is more complicated. Noise, beam hardening artefacts, and edge spreading are impossible to fully remove from the image (see section 2.6). figure 46 shows the results of the false gray values near the edges of artefacts.

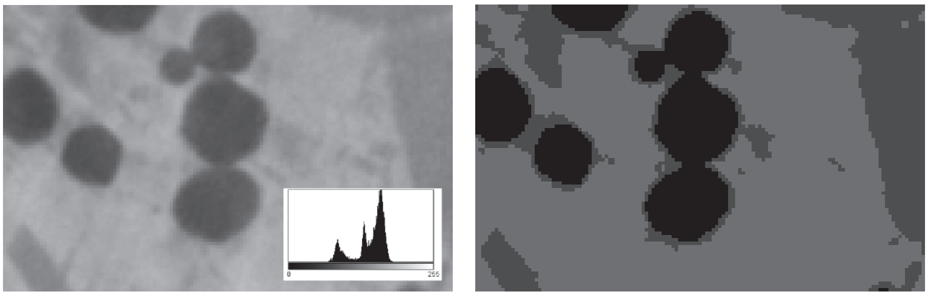

FIGURE 46 An edge spreading on multiphase segmentation of igneous rock. In the left labelled image, air is represented by black, the light mineral is represented by dark gray, and the heavier mineral is represented by light gray. In the right image (which shows the original data), the gray value corresponds (roughly) to the density of the material. As the interface between the phases of brightest and darkest gray value distributions is smooth, values exist that belong to phases between these two.

Various methods exist for gray value image segmentation problems. The methods can be grouped in many ways, as shown in [52, 80, 264, 274, 262]. We define the main groups as follows:

1. Threshold-based methods
2. Region-based method
3. Partial differential equation (PDE) -based methods
4. Graph-based methods

5. Artificial neural network-based segmentation
6. Morphology-based methods

Threshold-based methods [80] are simple considering only the voxel gray value in their basic form, not taking into account any shape or region similarity. Threshold is a common segmentation method used in XμCT, because it is easy to understand and to adapt to different external measurements, like known volume or structure thickness of the data. It is an attractive choice for segmentation due to its simplicity and is the reason that different materials should be separated by their gray values. The selection of the threshold value can have a large impact on the analysis results. Moreira et al. [166] and Nogueira et al. [173] have studied the effect of threshold selection on the image analysis results. They found that variations between the selected threshold values can be large between the operators and automated method, leading to considerable divergence in the average porosity values. Many methods for automating the algorithm have been proposed: Otsu [28], entropy-based methods, iterative methods [256], and local methods [251] can be used to find the suitable threshold value. For homogeneous materials threshold selection using data obtained from shadow images was proposed in [21].

The region-based methods [80] assume voxel value similarity and connectivity between the voxels. It is possible to incorporate many kinds of similarity criteria [100]. Region-based methods are typically more laborious to use because they require seed regions that are often defined manually [80]. For images with more artefacts, region grow can be used to split the sample into two or more phases. For instance, in [196] it is used for binarisation of an XμCT image of a paper, in [215] for an XμCT image of a iron ore sinter, and in [82] for rock. Region grow based methods are fast and especially useful when trying to separate certain connected structural components in the image when the component areas of the image have the same gray value. The watershed algorithm[254] is an algorithm that can be used to separate connected structures, into smaller pieces using certain rules. For structural segmentation of porous or grainy material, the watershed algorithm is often used to separate the individual pores or grains; as shown in [2] and [252]. Faessel and Julin [60] used a method called stochastic watershed to avoid the over-segmentation.

PDE based methods are a family of tools used for denoising [182, 199], segmentation [36, 115], and many other image processing [41, 42] algorithms. The connecting thread between the methods are the partial differential equations used to represent some specific properties. In segmentation, these algorithms usually assume voxel similarity and connectivity between the voxels, and adds constraints to the shape using the surface tension property. These methods are slower than the ones from the first two groups and usually require special knowledge to tune the algorithm. PDEs are often used to solve level-set method-type segmentation problems, although they have not gained great popularity on XμCT material analysis, probably due to high computational costs, but also and lack of commercial implementations. In [63] the level-set method was used to detect fatigue crack propagation. It has mostly used in biological [186, 5] and medical [236] applications where one or few organs are segmented from neighbouring tissue. As with the region growth, these methods usually require certain prior information for initialization.

The graph-based methods can be used in similar applications as PDE-based methods [18], such as for edge-preserving denoising [18] and segmentation [34]. Graph-based methods also have high computational requirements, however, they are mathematically more stable, do not require approximation of the PDEs [34], and can be a viable option when computing power increases. In segmentation, voxel similarity, connectivity between the voxels, and additional shape constraints can be used to handle the edge discontinuities in a similar manner as in PDE-based methods.

Artificial neural network-based segmentation methods are adaptive feature based-systems that can be trained to adapt to specific problems. In [53], an artificial neural network was used to recognize bone structure. Pulse-coupled neural networks are models based on the feline visual cortex and were used to segment MRI images in [44].

Many other tools and adaptations are used as well. In [255], a grainy sample is separated using a deformable surface that allows analysis of each individual grain. In [211], cracks in carbon-epoxy laminate were segmented using seeded growth. In a fibrous sample, it is of interest to separate each individual fibre, which was partially achieved in [9] and [10] by tracking the lumens of the fibres, and in [269] and [150], a medial axis transform was used to segment non-hollow fibres, and in [259], segmentation was obtained using graph cuts. In [156], (non-hollow) fibre segmentation was carried out using the heavy ball method. In bone research, it is interest to analyse both the structure of the pore space and the different types of bone. In [183], constrained region growth was used to detect the remodelling zones of a bone. To separate the trabecular and cortical bone, various methods exist based on image morphology [194], [40] and image filtering [146].

5.1 Segmentation of XμCT Images

The most commonly used segmentation methods in XμCT are relatively simple. The simplest and most adequate method is usually the most suitable. The properties of XμCT images (e.g., large datasets, no gradients, and material separation by a gray value based on density) and the requirement for simple use makes thresholding an efficient segmentation method for many purposes. The need for other segmentation method occurs when the image quality drops and thresholding cannot produce acceptable results.

5.1.1 Material Segmentation

Segmentation refers to an operation during which the voxels of the image are grouped according to their gray value or geometrical similarity. In material segmentation, the voxels are grouped according to their gray value similarity.

Once the segmentation is complete, a binarised or labelled image is produced. The binarised and labelled images may require post processing to remove falsely labelled areas. There are several possible techniques for post processing. Opening and closing operations are effective for removing noise (see section 3.3.2). During opening and closing operations, the size of the noise particles define the structuring element or the number of iterations of subsequent dilations and erosion (opening or closing). The operations can be performed before segmentation using gray value morphology. A median filter is also effective for removing small, falsely labelled areas from the image. Flood fill can be used to find the some property of the separated particles and the ones below some threshold (volume, surface area, circularity etc.) can be removed.

Thresholding

Thresholding is the most common and simplest way to binarise an image. The idea of thresholding is to divide the voxels according to their intensity value:

$$T(a,\tau) = \begin{cases} a[p] > \tau \Rightarrow p \in \text{Object}, \\ a[p] \leq \tau \Rightarrow p \in \text{Background}, \end{cases}$$

where τ is the chosen threshold value.

Fog high quality images, thresholding is an efficient way for segmenting an image. However, it requires the histogram of the image to show clear peaks for each material. To demonstrate the use of histograms and thresholding, see figure 47.

Due to artefacts the gray value of each material is not constant; instead it has a distribution that usually overlaps with neighbouring materials. The threshold value should be selected to optimally divide the image in least worst way. There are a few publications ([166, 173] for example) that claim large error margins for manual thresholds. To find the optimal threshold value automatically, several methods have been proposed. It is generally more accepted method to use an automatic threshold selection algorithm. Sankur [204] lists 40 methods and categorized them into six classes:

1. Histogram shape-based methods, where the τ is found by analysing the shape of the histogram, e.g. [198, 191, 76].

2. Clustering based methods, where the gray values of the image are clustered into two groups (e.g. [193, 118, 177]).

3. Entropy based methods that aim on minimizing the entropy of the voxel groups (e.g. [136, 109]).

4. Object attribute-based methods that attempt to find a τ that maximizes the similarity between the gray value image and binarised image (e.g. [237, 95]).

5. Spatial methods use higher order probability distribution or pixel correlations (e.g. [69]).

Many automatic threshold selection methods are tuned to work with certain types of data and may not be applicable to XμCT images. The automatic systems optimize certain properties of the image or histogram that may not most suitable for the XμCT images.

An another, perhaps more recommended way for selecting the τ is to use an independent measurement compared to the results measured from the binarised image. Information about porosity (measured, for example with a mercury intrusion porosimeter,

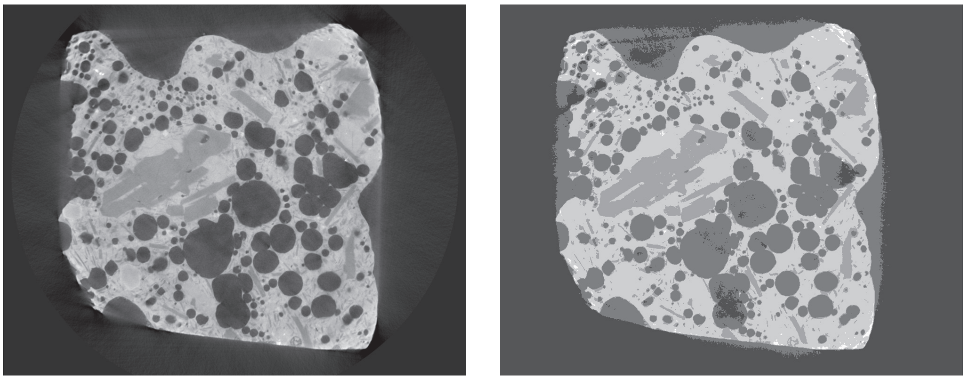

(a) Original image

(b) Labelled image

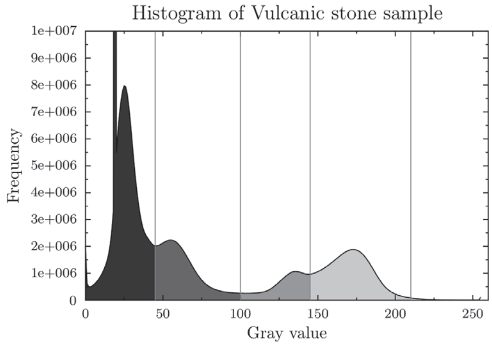

(c) Histogram

FIGURE 47 Thresholding, histogram, and labelled images. The vertical lines in the histogram denote the (hand-selected) threshold values, and the colors of the labelled image denote the colors of the areas in the histogram.

see [99] for details), density, weight, volume, or thickness of details (seen by some other imaging method) can be used to ensure the threshold value.

In some cases the thresholding is not working due to the reason that the gray value ranges of different material phases overlap we need a stronger approach for the segmentation. Region grow based methods are the next option where also the locality and neighbourhood of the voxels are taken into account. This adds more work to the segmentation process as the seeds for the regions need to be determined.

Multiphase thresholding

In the case of multiple phases, similar-histogram based method than thresholding can be used to label the voxels, see figure 49. The voxels are divided into more than one class by finding more than one threshold value. The Otsu's method [177] has possibility to find multiple thresholds, and Mardia and Hainsworth (MH) have introduced a Bayesian based threshold method [155] for image labelling. Their method is based on the Bayesian allocation rule which assigns voxel gray values into group to maximizes the likelihood of that allocation.

Another general multi-phase segmentation method is based on Gaussian mixture model (GMM), which assumes that images have n number of regions distinguishable from each other by their gray value distributions, and assumed to follow a Gaussian shape with a mean of μ_n and a standard deviation of σ_n. The gray value probability distribution for the whole image is a mixture of the Gaussian distribution from all regions:

$$p(\boldsymbol{\theta}) = \sum_{i=1}^{n} \phi_i \mathcal{N}(\boldsymbol{\mu_i}, \boldsymbol{\sigma_i}),$$

where ϕ represents the weight given for each normal distribution $\mathcal{N}$, and θ is the group of parameters describing the whole distribution ($\theta = \phi_1 ..._p hi_n, \mu_1, ...\mu_n, \sigma_1, ..., \sigma_n$). The system is usually solved using an expectation maximization (EM) algorithm, which is described in more detail, for example, in [62].

In figure 48 an example of the Gaussian mixture model is given for an igneous rock image.

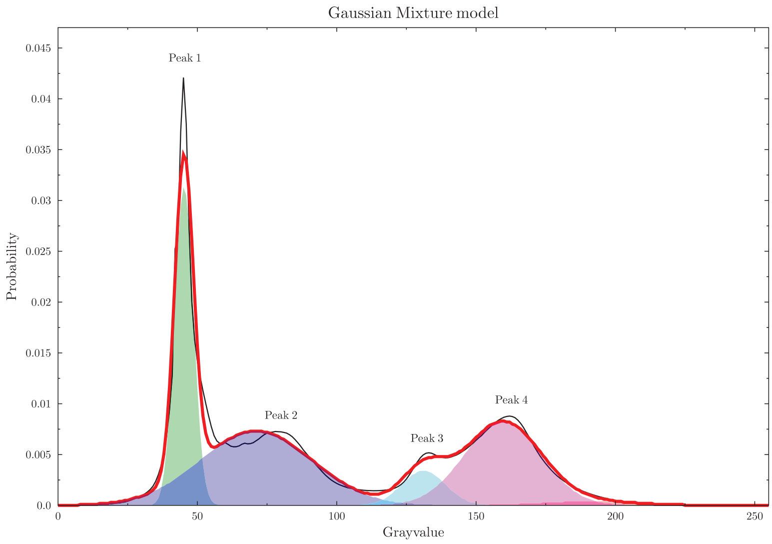

FIGURE 48 An example of the Gaussian mixture model for an igneous rock sample. The filled areas represent the Gaussian components of the image, the thick line is the sum of the Gaussian components, and the thin line is the original gray value probability distribution obtained from the image.

Region Grow

Region growing [80] is a method for determining connected areas in an image. The connectivity is based on similarity on voxel gray values, and it can be the gray value itself or some value calculated from the it (e.g., the gradient or standard deviation). Region grow is typically used in cases where the gray value distributions of separate phases overlap, but the edges of the objects are well defined (in which case the thresholding does not produce satisfactory results). Algorithm 5 describes the method in more detail.

Algorithm 5 Region grow

```
1: For each desired region, $V_i$ define at least one seed point (i.e, a point that belongs to the region).
2: For each $V_i$ if there is a voxel in $B_{\text{out}}(V_i)$ that fulfils the region similarity rule, it is added to the region.
3: Repeat step two until there are no voxels that do not belong to any region.
```

In practice, there are two approaches to region grow, either all the voxels of the image must be in a certain region (in which case step two of Algorithm 5 must be changed so that at least one point is added to some region), or the system is stopped when certain criteria are met. For both approaches, certain rules will hold true for the regions:

- V_i is a connected region;
- $V_i \bigcap V_i = \varnothing$, regions do not overlap; and
- All pixels in V_i must satisfy the similarity criteria.

A common way to define the seed areas is to use the threshold to find the regions that are known to belong the correct phase. The problem here can be the noise which can cause false seeds. To speed up the processing, it is useful for each region to have a list of its current neighbours stored in a histogram type container (in which the voxels are indexed according to their gray value), and thus the next voxel of requires gray value is fast to acquire.

The ruling for voxel similarity is typically gray value based; also gradient based similarity measurements are used in case the edges area sharp. The main problem with region growing is the leaking that occurs when the edges of the objects are not sharp; edge sharpening preprocessing can be useful (e.g., AD, BF, and MS denoising).

The benefits of this method are that it is simple, relatively fast, and requires an understandable parameter set. It usually tolerates noise quite well and also provides good customization possibilities. The following issues must be defined to realize the region grow algorithm:

- The set of seed points
- Definition of similarity

5.1.2 Structural Segmentation

In structural segmentation, the problem in practice is separation of the objects that are touching. Usually the point where the objects touch is small, and the structure should be separated from its local narrowings into separate substructures. We consider here mostly the watershed algorithm that is versatile in such a segmentation in case there are several object that need to separate simultaneous. In case there are only few objects, more manual methods can be used, and to this end we present the Edwards-Wilkinson equation based segmentation method.

Watershed

The watershed algorithm can be used to separate structures that are connected to each others by a local narrowing. The idea in 2D is to consider the gray value image as a topographic map, where the gray values represent the height of the corresponding pixels on the map. The algorithm then finds the lines that work as a watershed in the topographic map (i.e., if water droplets would fell on both sides of the line, they would slide down in separate directions). For 3D images the topographic map can be interpreted as a gravity field where randomly placed particles would be attracted to certain gravitation maximums and the watershed lines are actually surfaces that separate the interfering volume of the gravitation maxima.

Several algorithms determine the watershed lines, one efficient for large 3D images is given in Algorithm 6 (modified from [27]). The distance map a_{dt} of the original binary image is given as a parameter.

Algorithm 6 Watershed

```
Invert the distance map: $a_{dt} = max(a_{dt}) - a_{dt}$.
Find the local minima of $a_{dt}$. Let $V_i$ be the group of pixels belonging to $i$ th local minima. Notation $\min(V_i)$ is used for the local minima value belonging to $V_i$.
Start flooding with virtual water. Let $h^t$ depict the height of the water level, while $h^0$ is initialized to the global minimum gray value in $a_{dt}$.
while $h^t$ is less than the maximum value at $a_{dt}$ do
    $h^t \leftarrow h^{t-1} + 1$
    For each $V_i$ with a $\min(V_i) = h^{t-1}$, add the free neighbouring pixels with gray value $h^t$ to the $V_i$, but only if the labelled neighbours of that pixel have have the same label $i$.
end while
The watershed lines are now where virtual water from two or more basins $V_i$ meet.
```

This method works if the structures themselves do not contain any local narrowings (smaller than the areas where the objects are connected). It is efficient to separate the individual pores of a connected pore network or individual particles.

The watershed algorithm tends to over-segment. With a normal watershed each local minimum creates a new basin area in the image. In natural images, the noise can cause more local minima than necessary. There are several schemes to avoid the over-segmentation. First is by preprocessing, in which denoising and geodesic reconstruction (see Algorithm 2) can be used to remove minimums that are close in codomain. Another option is a seeded watershed. In a seeded watershed the basins are initiated only from the given seeds, that are provided separately. This sometimes provides better result because the seed image can be processed separately. A third option to avoid the over-segmentation is to use post processing operations, some examples of those include:

- Small areas are merged to its neighbour. Thus, when finished, if $\sum_{\mathbf{v} \in V_i)} \mathbf{v}$ value is smaller than a given threshold, it is merged to a neighbour.

- Areas where the narrowing between the basins is small are merged. That is let V_i and V_j be neighbouring basins, if $|\min(V_i) - \min(V_j)|$ is smaller than some threshold, the basins are merged. This can be obtained using the geodesic reconstruction.

- Neighbours with large common interface area are merged.

EW Based Interface Detection

In cases where only a few objects in the image are to be segmented, manual tools can be used. The level-set and active contours method are common in these situations. Next a simple and fast image segmentation method suitable for planar, tubular and spherical objects [241] is presented. This method allows a flexible sheet (with a known location) to adapt itself to the shape of the interface. The method is based on the following Edwards-Wilkinson equation:

$$\frac{\partial h(\mathbf{x};t)}{\partial t} = \nu \, \Delta h(\mathbf{x};t) + F + \rho f(\mathbf{x}, h(\mathbf{x};t)), \tag{36}$$

in which $\mathbf{x} = (x, y)$ are the lateral coordinates of the sheet and $h(\mathbf{x};t)$ is its depth at time t. Thus, the location of the sheet in the 3D image at time t is $(x, y, h(\mathbf{x};t))$. The Laplace operator, $\Delta h(\mathbf{x};t)$, is the surface tension term, which gives the sheet resistance to noise and defects in the surface. Surface tension is controlled by factor ν and controls the tolerance to noisy pixels and discontinuities. $a(\mathbf{x}, z)$ is the grey-scale value of the original 3D image at (x_1, x_2, z). A constant downwards force, F, makes the sheet propagate towards the interface, and $\rho a(\mathbf{x}, z)$ describes the spatially varying force opposing its propagation.

While the sheet is above the surface, noise in the image will cause small fluctuations in $\rho a(\mathbf{x}, z)$, which are counteracted by the surface tension of the sheet. When the sheet meets the surface, there will be an increase in the opposing force causing the sheet to halt, after which the sheet will fluctuate locally and adapt itself to the topography of the surface. The chosen surface tension then determines how the interface follows sharp features (i.e., indentations, holes, and protrusions) in the topography. When the terms in equation (36) are in steady state, h is immobile and the final position of the surface of interest. If GSV is defined as the average gray-scale value, $GSV = \text{Ave}(a(\mathbf{x}, h))$, of the surface to be detected, $\rho = -F/GSV$ is chosen to allow for the sheet to come to a halt at the surface.

The Weierstrass' function [30] provides an efficient way to discretise the method. The Weierstrass transform is closely related to the the diffusion equation, which has a constant diffusion coefficient. Using a property of the Weierstrass transform, $W_t\{W_s\{\hat{g}\}\} = W_{t+s}\{\hat{g}\}$, the equation can be expressed in a form suitable for discretisation,

$$h^{t+\Delta t} = W_{\Delta t}\{h^t\} + \int_t^{t+\Delta t} W_{t+\Delta t-s}\{g_{h^s}\} \, ds. \tag{37}$$

Implementation of the algorithm is the shown in Algorithm 7. Image a is given as the parameter. F is the down force, which is in practice 1. Parameter ρ defines the sheets sensitivity to gray values (i.e., the gray value that stops it). Parameter σ defines the surface tension.

Algorithm 7 EW segmentation

```
Initialize the sheet $h_t, t = 0$ to the desired level: $h_0 \leftarrow l$. The sheet is often initialized at $l = 0$, but occasionally if the surface to be detected is far from the $z = 0$ level, it is convenient to initialize it closer to it.
repeat
    Apply the vertical forces: $h_t[i,j] = h_t[i,j] + F + \rho a[i,j,h_t[i,j]]$;
    Apply the surface tension: $h_t[i,j] = W_\sigma(h_t)$;
    $t = t + 1$;
until The sheet is stable or the iteration limit is reached.
```

TABLE 7 The similarity percentage of different multiphase segmentation methods. The phases refer to material phases shown in color in figure 49.

Phase	1	2	3	4	5
GMM - K-means	77.2	66.1	59.1	66.3	11.3
MH - GMM	71.8	56.2	55.1	74.7	21.5
K-means - MH	92.8	83.2	87.5	79.5	52.4

The tubular and spherical shapes are obtained using a coordinate transform to shape the sheet.

5.2 Segmentation results

In this section, we provide the segmentation results from the perspective of XμCT imaging. We consider the differences in denoising methods when separating the material phases (intensities) from the image. In addition, we show a few commonly used structural segmentation methods. figure 49 shows a results obtained using few semi-automatic multiphase segmentation methods.

As we do not have a gold standard for segmentation results, it is impossible to estimate how well the methods performed. table 7 compares results between different methods. There is a significant variance between the methods, and it is impossible to say which performs the best. To this end, some controlled test samples is needed.

5.2.1 Segmentation of matter

In this section we analyse the material segmentation methods. Considering the results from the previous section we consider three denoising methods: 1) Blurring methods (Gaussian), 2) Edge sensitive methods (VaWe), and 3) The edge enhancing methods (MS).

Simple structure

The first test on segmentation is a simple case of binarisation of pencil lead (graphite) mixed with epoxy (see figure 50). The pencil leads are 0.7 mm thick and broken into

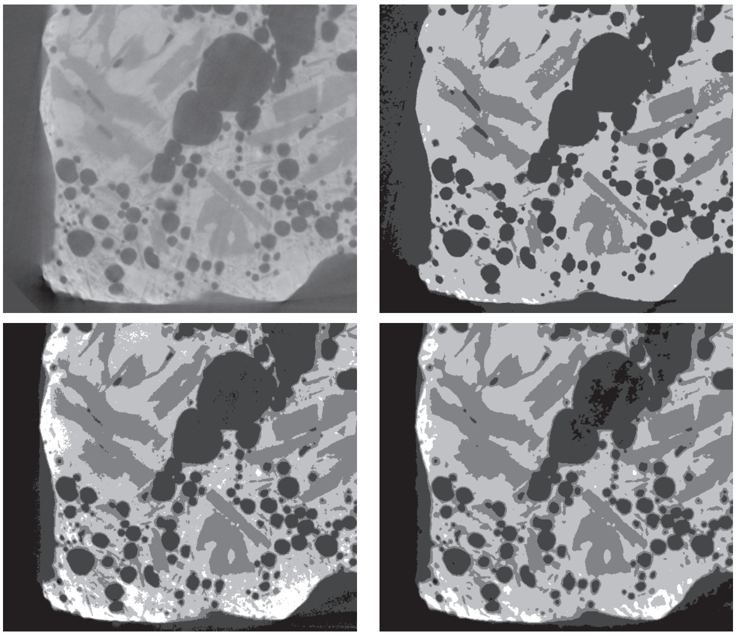

FIGURE 49 The result of few multiphase segmentation algorithms. The upper left panel original image shows the Gaussian mixture model. The lower left panel shows K-means segmentation, and the lower right panel shows Mardia-Hainsworth segmentation. In the segmented images, black and darkest gray represents the void and other gray values different minerals.

short sticks. The approximate volumes of the leads are known: there are 12 pieces of lead; the thickness of apiece of lead varies between 0.70 mm to 0.72 mm, and the length of each piece of leads is 60 mm. These pieces of lead are broken into shorter pieces and mixed with epoxy. The sample is imaged using a Skyscan 1172 XμCT scanner, with the X-ray tube set to 44 kV source voltage and 76 uA current. The rotation step is set to 0.25 degrees. The voxel size of the resulting image is 16.16 μm with a resulting file size of 2 GB.

Due to the variation in lead thickness, we have a certain margin of error within the approximation of the sample's real volume. In addition, the density of epoxy is not homogeneous; some air bubbles are present, as well as some more dense spots (perhaps resulting from the process of mixing the two components by hand). The dense spots pose a challenge for segmentation as the density of the graphite is very close to the density of some of spots. However, as we know that our material consists only of bulky pieces, we can filter out the dense particles that are smaller than a certain volume threshold. This can be done from the binary image using flood fill, or from the gray value image using top-hat filtering; see section 3.3.2 for details. Here, we used the top-hat transform in order to obtain non-biased volume threshold curve to select the threshold value.

Figure 51, which shows the results, also presents the volume of the binarised graphite as a function of the threshold value. The results indicate that even the simplest denoising methods are able to denoise the sample and to provide satisfying binarisation results. For

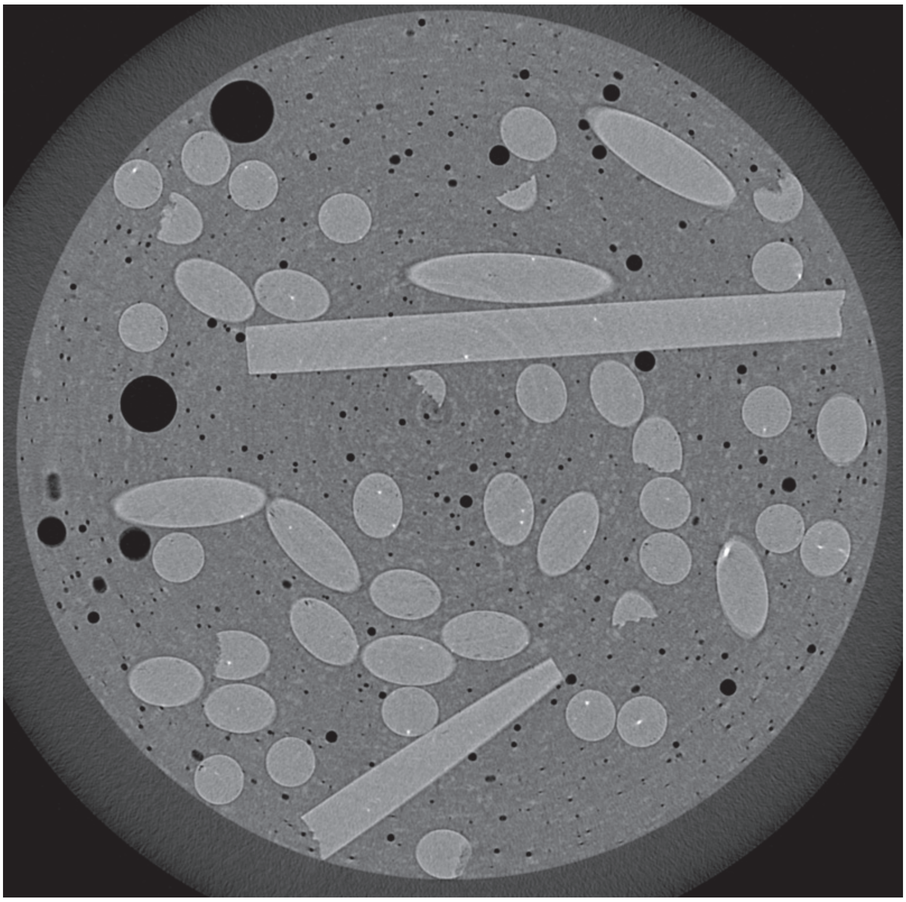

FIGURE 50 A cross-sectional image of the pencil leads in epoxy.

non-edge sensitive methods, the slope of the curve is steeper, indicating that the small changes in threshold value will affect to the volume of the sample more than with the edge-sensitive methods. However, because the top-hat transformed curve is close to the original curve (i.e., not many small particles have been removed), the changes in threshold value are more likely to affect the thickness of the structures than to add new solid regions. That effect can be useful if the thickness of the structures is known; the know thickness value can be used to validate the threshold value selection. For the edge-sensitive methods, it is obvious that the bright blobs are not smoothed, and that these blobs should be removed before they are compared with the experimental value. The benefit of these methods is that the slope of the volume-threshold curve is lower, thus providing a longer "OK" section for the threshold value; this makes the selection of an appropriate threshold value more robust. If the denoising time is being considered, the non-edge-sensitive method is a reasonable choice for denoising, though an experimental measurement for selecting the threshold value is also required.

The final measurement performed in this study involved analysing the surface area between the different pieces of the contact area. The results are shown as a percentage of voxels belonging to the contact area (see table 8; the results for all denoising methods

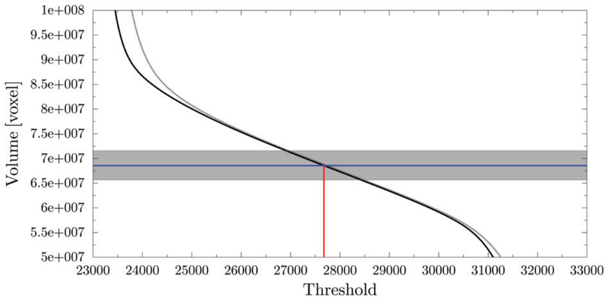

(a) Gaussian filter

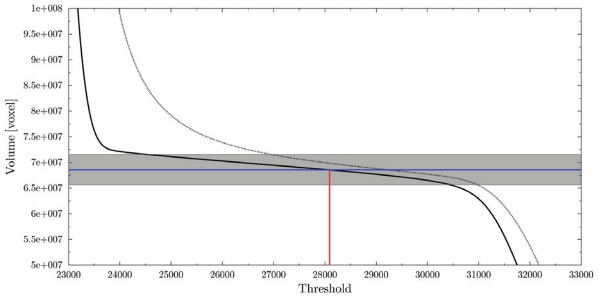

(b) DCT

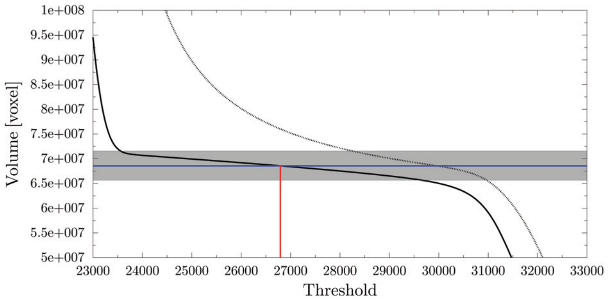

(c) VaWe

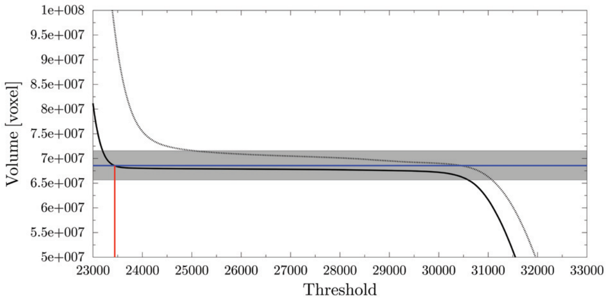

(d) MS

FIGURE 51 The threshold vs. object volume for the segmentation of the simple graphite epoxy sample. The solid line is after top-hat filtering and dotted line is without it. The horizontal line is the experimentally measured volume of the sample and the vertical line shows the threshold value when the true volume is expected. The gray area shows the error limits of the measured volume. The graph has been zoomed to focus on the area of interest.

can be found in table 14 of Appendix 2). Of note here is the variability of the results. This is because the smoothing denoising methods lower the details detectability of the system, and thus makes larger area to appear being in contact. The real contact area of rigid particles, with mostly round shape, is near zero. Due to the limited resolution of the imaging system, the contact areas reflected are larger than the real contact areas. Hence, it is necessary to acknowledge that this analysis might not actually measure the real surface area of the contact area; instead, it may actually measure the surface area of the objects that are so close that they are considered to be touching one another, keeping in mind imaging limitations, noise, and post-processing.

TABLE 8 The percentage of voxels belonging to the contact area.

Gaussian	DCT	MS	Vawe
0.22	0.08	0.09	0.09

We also considered the automatic threshold selection methods. We used the algorithms provided by ImageJ [209]. We used the resulting gray value to binarise the image, then determined the corresponding solid volume. The results are shown in figure 52 (the results for all denoising methods can be found in figure 87 of Appendix 2). The results of this portion of the study are further discussed in section 5.2.1.

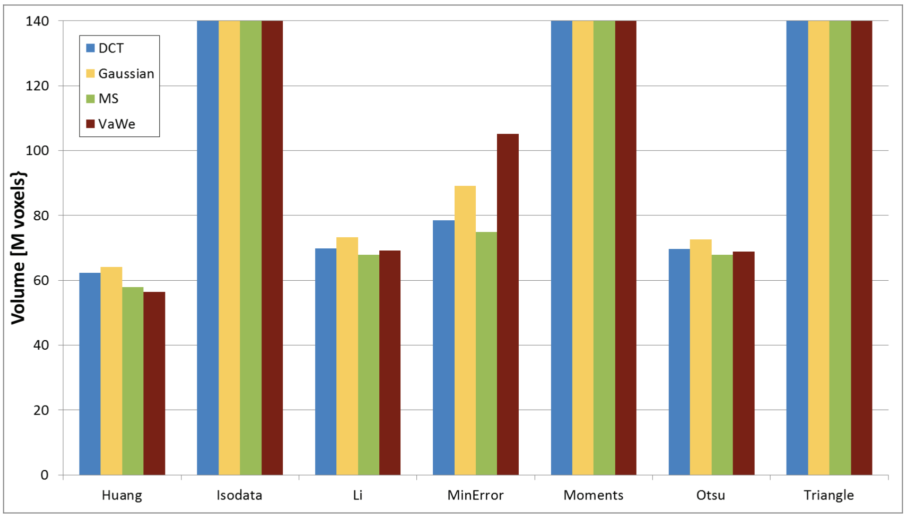

FIGURE 52 The volume of the sample determined using some automatic threshold selection methods. The red line indicates the measured volume. Isodata, Moments, and Triangle gave out-of-scale, truncated results.

Grainy structure

The second segmentation test was a more complex binarisation of pencil lead (graphite) that had been crushed down to various particle sizes and mixed with epoxy. The weight of the crushed pencil lead particles is measured to approximate the volume of the lead.

The sample was imaged using a Skyscan 1172 XμCT scanner with an X-ray tube set to 44 kV source voltage and 76 uA current. The degree of rotation used was 0.25. The voxel size of the resulting image was 16.16 μm resulting in a file size of 2 GB.

Because we did not know the size distribution of the grains, we were unable to use the top-hat filter to remove the smaller particles from the data. The epoxy contained some spots that were close in density to the graphite; however, these spots were slightly less dense than the graphite, and their edges were usually less sharp. The adjust for this, the parameters of each denoising method were adjusted in order to smooth the spots and that each method would give almost the same noise standard deviation for the noisy area.

We also used the automatic threshold selection methods (provided by ImageJ [209]) with this sample. The resulting threshold value was used to binarise the image, after which we determined the corresponding solid volume. The results from this analysis is shown in figure 54, and the results for all denoising methods can be found in figure 88 of Appendix 2). Studying the result here, and also from figure 52, we conclude that the automatic methods seem to be slightly sensitive to the denoising method and can be unreliable. Some methods, such as those of Huang, Li and Otsu seem more robust for this kind of process. However, the test material related to the automatic methods in this study is quite small, making it impossible to reach reliable conclusions

Multiphase structure

To compare the segmentation of a multiphase case, we created an image in which the volume of the materials was known. The materials we user were an eraser, a rubber band, and a pencil lead (graphite). The volume of each of these materials was first determined by XμCT; the materials were first scanned whole, then chopped into small pieced and immersed in the epoxy. The eraser and rubber were easily distinguished from the epoxy, while the graphite created a challenge for the segmentation, as the gray values overlapped with the background intensity. The sample was imaged using a Skyscan 1172 XμCT scanner with an X-ray tube set to 72 kV source voltage and 137 uA current. A rotation step set to 0.3 degrees and an aluminium filter of 1 mm were used to avoid beam hardening of the artefacts. The voxel size of the resulting image was 4.47 μm, resulting in a file size of 123 GB. For practical reasons, the file was cropped and rescaled to obtain 18 μm voxel size; the final file size was around 2 GB.

The segmentation of the rubber band and the eraser was straightforward, as these items could be segmented using thresholding. We calculated the joint volume of these materials and determined the threshold value using the volume-threshold curve. The separation of rubber band and eraser was not that straightforward, figure 55 shows the overlapping gray values of the rubber band and eraser caused by the internal structure of the rubber band. Thus, plain thresholding is not sufficient for separating these two phases. We used morphological gray value opening (the operation is defined in more detail in algorithm 8) to level the gray values in each phase (see figure 56 for the result). We used the binary image of rubber band and eraser as a mask for the levelled image, then thresholded the result to separate the eraser and rubber band. The results are shown in table 9, and the result for all denoising methods can be found intable 18 Appendix 2. The average amount of error was 1.5%, with the mean and the Gaussian filter giving the smallest amount of

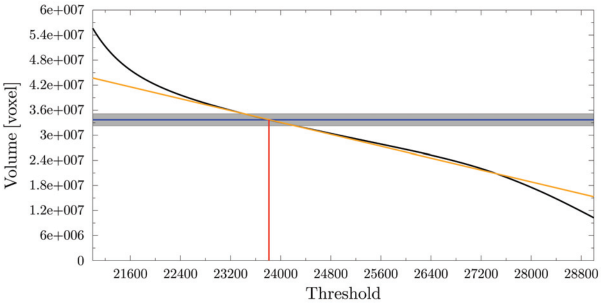

(a) Gaussian filter

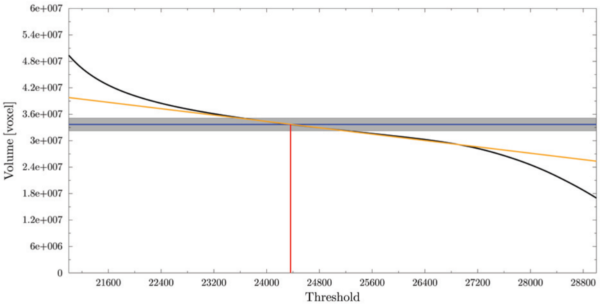

(b) DCT

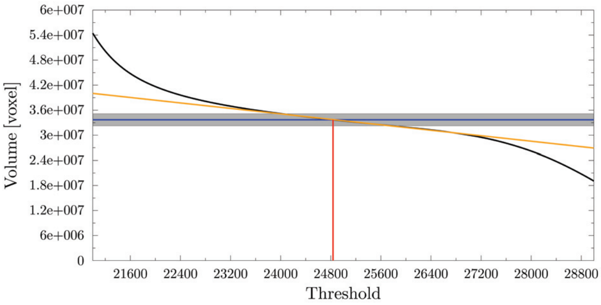

(c) VaWe

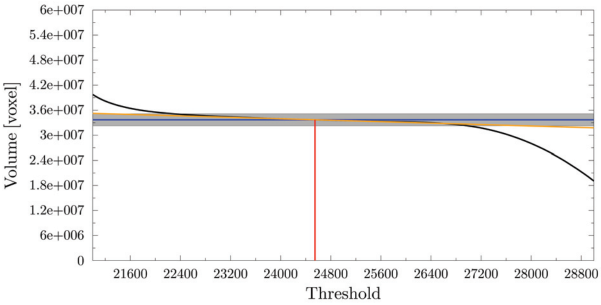

(d) Mean shift

FIGURE 53 The threshold vs. object volume for segmentation of the graphite particles epoxy sample. The black line is the volume as a function of the threshold. The horizontal line is the experimentally measured volume of the sample. The vertical line shows the threshold value when the true volume is expected. At the cross-section of the horizontal and vertical line is the tangent of the black line. The gray area depict the error limits for the true volume. The graph is zoomed into the area of interest.

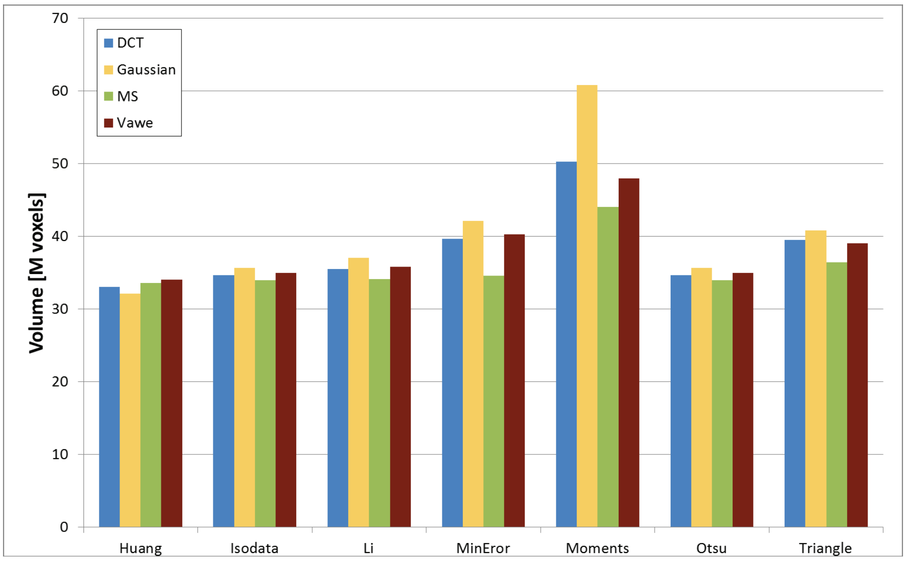

FIGURE 54 The volume determined using some automatic threshold selection methods. Red line is the measured volume.

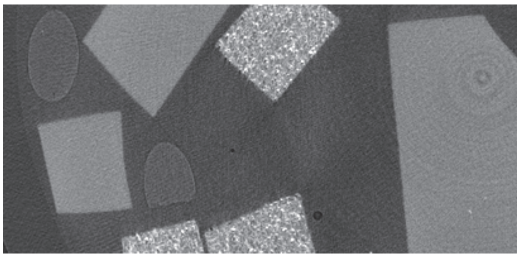

FIGURE 55 A 2D crop of the segmentation sample image. The brightest material (with internal structure) is the rubber band, the mid-gray is the eraser, and the darkest gray (oval shape) is the graphite. At the far left side of the image, the edge of the plastic container is visible.

error.

a_r contains the mask for rubber band and a_e contains the mask for eraser.

The segmentation of the graphite, however, was entirely different from the segmentation of the other materials. The shadow and streak artefacts (see section 2.6) cause variation in the background gray values overlapping with the gray values of the graphite. This makes it impossible to find a threshold value that would separate the graphite from the background. We have no evidence for following, but in our opinion, if the sample contains materials with large density differences, the streaks and shadows very easily hinder the segmentation of the lighter materials. If the acceleration voltage is adjusted according to the high-density material, the contrast will be low at the least dense material. If the acceleration voltage of the XμCT scanner is adjusted according to the low-density material, the high-density material will cause shadows. The properties that differentiate

Algorithm 8 Morphological separation

```
1: $a_\tau \leftarrow T(a,\tau)$, where threshold value $\tau$ is selected, such that the rubber band and the eraser are separated from background.
2: $a_{\text{leveled}} \leftarrow a \circ b$, where the size of $b$ is selected, such that the shape of the objects is preserved as well as possible, but a reasonable smoothing of gray values is still accomplished.
3: $a_{\text{e+r}} \leftarrow a_{\text{leveled}} \cup a_\tau$, where $\cup$ denotes the masking operation.
4: $a_{\text{r}} \leftarrow T(a_{\text{e+r}},\tau)$, where $\tau$ is selected to separate the rubber band from the background.
5: $a_{\text{e}} \leftarrow a_{\text{e+r}} - a_{\text{r}}$
```

the graphite from the background are the shape of the tubes and the faster gradient at the edges. We used this information to build a segmentation algorithm based on region growing, where the enlargement of the area was based on the gradient such that the region did not expand into areas surrounded by large gradients. This allowed us to binarise the image into a solid and a background, and the graphite region could then be separated by subtracting the (already known) rubber band and eraser from the solid volume. This method is clearly more complicated, more time consuming, and harder to control. The parameters of this method are the seed points and the gradient step limit, and we were therefore unable to create a similar volume–parameters graph to ensure the correctness of the volume. The obtained graphite volumes of this method are given in figure 9. In this case, the more advanced denoising methods clearly give better results. The property of a denoising method of preserving the large gradients (the edges of the relevant objects), or even sharpening them, is beneficial for this kind of a segmentation. Here, the edge sharpening methods gives the best result, while the other methods all have quite a large amount of error. The result from all denoising methods can be found in table 18 of Appendix 2; these results show how the anisotropic diffusion is only slightly worse in this method than it is with other comparable methods. However, the stronger edge-sharpening property of MS denoising makes it more suitable for this kind of a segmentation problems (see figure 57 for comparison of the edge sharpening property of these methods).

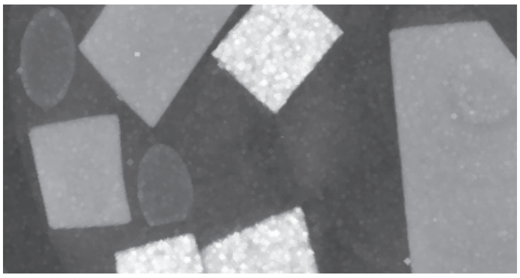

FIGURE 56 A 2D crop of the segmentation sample image shown after the gray-value opening with a radius of 4 pixels.

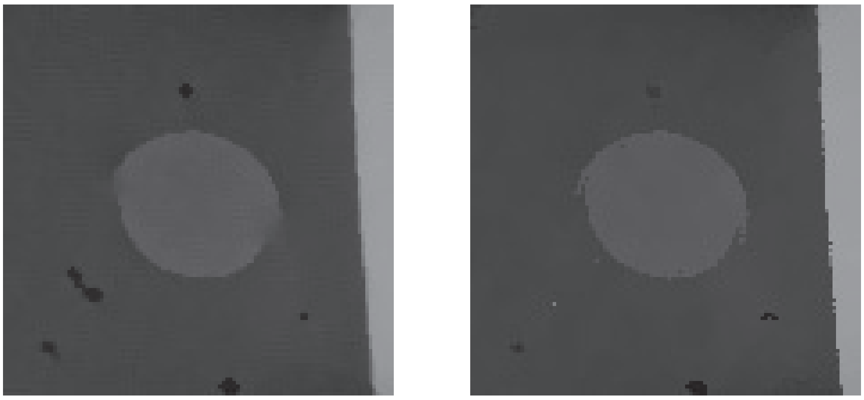
(a) (b)

FIGURE 57 A cross-sectional image of the denoising result of AD (a) and MS (b).

TABLE 9 The volume of different materials in voxels, obtained from the labelled data. The values are rounded to the closest thousand (k denotes kilo).

Material	Measured	Gaussian	DCT	MS	Vawe
Eraser	78731 k	79475 k (101%)	79958 k (102%)	80067 k (102%)	79946 k (102%)
Rubber band	15109 k	15270 k (101%)	14909 k (99%)	14772 k (98%)	14869 k (98%)
Graphite	4237 k	5139 k (121%)	4842 k (114%)	4301 k (102%)	5927 k (139%)

5.2.2 Segmentation of Structures from Binarised Images

To analyse the quality of the segmentation, we performed the thickness analysis for the binary images on the simple pencil leads (see section 5.2.1). The thickness analysis is also a method for separating the structures according to their thickness. The average thickness of the structures were determined using the local thickness transformation (see section 6.1.2). The results are shown in table 10 and the results for all denoising methods can be found in table 15 of Appendix 2. The values in the table were determined by taking the average gray value from the center part of each piece of lead (determined by thresholding the distance transform of the structure), thus avoiding the problems the edges would cause. The results from the different pieces of lead were all quite similar. However, this type of analysis tends to underestimate the thickness values; this is because the local thickness transform finds the “maximal fitting ball”, which is very easily disturbed by any noise in the sample. For example, the values for the MS binarisation were lower than the others due to edges that created some binary noise in the sample. Fortunately, this error represented less than 1.5% of the error caused during the preprocessing method, which is less than the voxel size of the image.

In addition to conducting a thickness analysis, we separated the individual leads pieces using the method described in section 12. The number of individual graphite pieces found with each segmentation method is shown in table 11 (the results for all denoising methods can be found in table 16 of Appendix 2). The difference in results is mostly due to the star artefacts (see section 2.6) caused by impurities in the graphite. The artefacts

(a) Original data with star artefact.
(b) VaWe filtered and segmented.
(c) Gaussian filtered and segmented.

FIGURE 58 An example of an effect of a start artefact (see section 2.6) to segmentation process.

TABLE 10 The average thickness of the leads analysed by local thickness transformation. If the real thickness of a lead is approximately 710 µm, the largest error (1.3% error) is with the MS.

Gaussian	DCT	MS	Vawe
704,8 µm	706.8 µm	700,6 µm	705,6 µm

cause unpredictable events to occur during the segmentation process (see figure 58 for visual demonstration). The more edge-sensitive algorithms do not smooth these artefacts as the smoothing filters do; therefore, the artefacts remain in the binary data, causing segmentation problems.

TABLE 11 The number of individual graphite particles found using each denoising method. The real number of particles (108) was determined manually.

Gaussian	MS	DCT	VaWe
108	109	109	111

To further analyse the crushed graphite pieces (see section 5.2.1), we used the local thickness transform to define the thickness distribution (see section 6.1.2) of the particles. This method can also be used to separate the structures according to their thickness. The results of the thickness transform are shown in figure 59 (see Appendix 2 to see the results for all denoising methods). The shape of the distribution was relatively similar for the larger grain sizes between the different methods. With the non-edge sensitive methods, the small particles were smoothed out or merged into the larger particles. This caused the distribution to be missing small particles, and it also widened the other peaks to the right, thus creating more large particles. The edge-sensitive methods all had similar performances due to their similar shape distributions. However, we do not have a ground true particle size distribution for this material and the results should be interpreted only qualitatively.

We also used the watershed segmentation (see section 12) for this sample. table 12 is presents the number of separated particles captured by each method. The result for all denoising methods can be found in table 17 of Appendix 2. There were major differences in the number of separated particles captured due to the different denoising

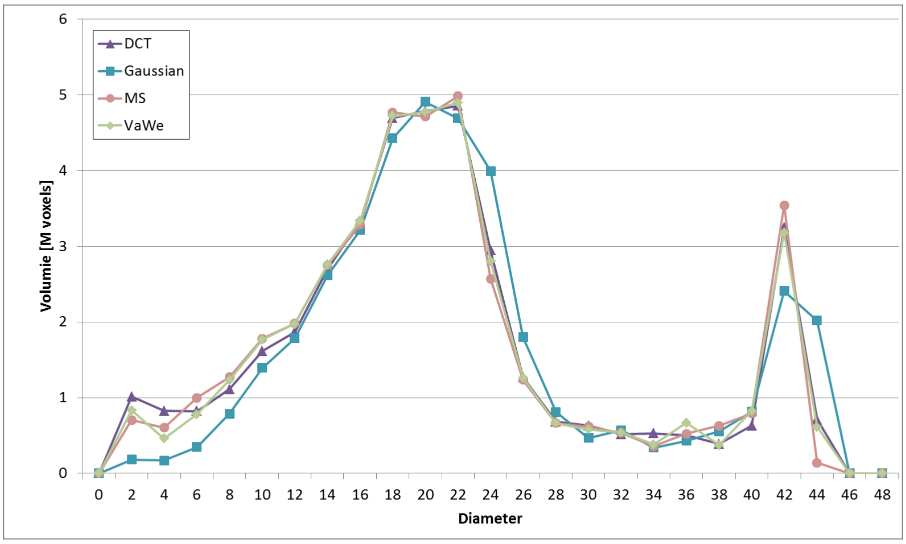

FIGURE 59 The volume of particles as a function of particle diameter.

methods used; some methods were able to smooth out more particles and combine them in different ways, depending on the parameters given.

TABLE 12 The number of particles found using a watershed for particle separation.

Gaussian	DCT	MS	VaWe
7198	20017	12012	57592

5.2.3 Segmentation of Structures from Gray Value Images

The segmentation of structures directly from gray value images requires methods that are generally more labour-intensive than those methods that use binary data. When considering the entire process (denoising, segmentation, etc.), however, the amount of labour involved can to be about the same across the different methods. Dividing the overall process into smaller tasks usually simplifies the individual tasks and makes the entire process more approachable. On the other hand, a long chain of small tasks may cause the effects of the parameters and errors to all accumulate at the end of that chain, again complicating the process of finding the correct parameters and minimizing error. The methods that separate the structures from the gray value images are, in our opinion, best used when there are only a few things to separate. The use of EW segmentation is described in section 5.1.2.

Paper is a complex material with various end uses. Some paper grades are coated with, a mixture of mineral pigments and latex. A common task in the 3D analysis of paper structure is determining the topology of the aforementioned coating layer.

In the present study, segmentation of the coating layer took place in two phases. During the first phase, we determined the top surface of the coating layer (see figure 60), while in the second phase, we determined the bottom surface (see figure 61). The

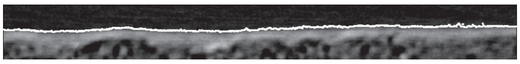

FIGURE 60 Top surface of a coating layer of paper. This surface is shown as a thick white line above the coating.

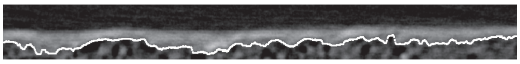

FIGURE 61 Bottom surface of a coating layer of paper. This surface is shown as a thick white line beneath the coating.

following steps were used throughout the process:

1. In order to detect the top surface of the coating layer, the sheet was initialized at the top of the image. The downward force on the sheet was constant, and the upward force was set up to stop the sheet when the sheet met the interface ($\nu = 1/45$). The stopping parameter was selected by inspecting the gray values at the coating layer. This method is quick and efficient for testing a few parameters in order to find the optimal one.
2. Surface tension of the sheet was adjusted so as to handle the surface holes.
3. The bottom surface of the coating layer was detected by continuing the propagation of the sheet from the top surface. This required taking a negative of the image and adjusting the forces to fit the new intensity values; we used $\nu = 1/210$ for the upward force.

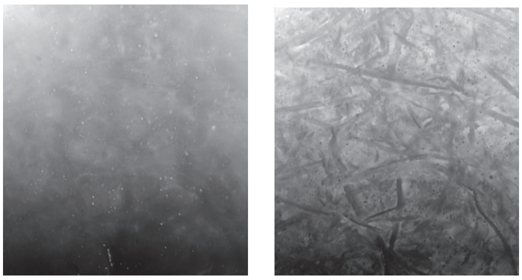

FIGURE 62 Top and bottom surface topographs of a coating layer of paper.

The output of this process was a profile of the coating layer. In addition, coating layer could be removed from the image so as to allow an easier analysis of the base paper.

Next example is to use the EW segmentation method to find a seam between two friction-welded wood samples. The X-ray intensity of the seam was the same as that of the annual rings and, thus, it would have required a special pre or post processing if a simple binarisation method had been used for segmentation of the image.

This segmentation process took place in two phases. During the first phase, the upper surface of the seam was detected using a planar version of the method. The sheet was then allowed to approach the seam from above in order to initialize to the top of the image. In the second phase, the lower surface of the seam was detected by letting the sheet move upwards, starting from the bottom of the image. The results of these two processes are shown in figure 63. Because these processes gave us the upper and lower surfaces of the seam, the image could then be binarised for a more detailed analysis (see figure 64).

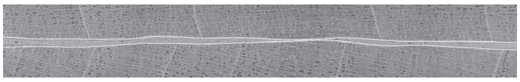

FIGURE 63 Cross-sectional image of a friction-welded wood sample; the upper and lower surfaces of the seam are marked with a white line.

FIGURE 64 Three-dimensional visualization of a binary image of the seam.

A cylindrical coordinate transform allowed us to segment the elongated objects. We used the EW method for segmentation of the femoral bone of a mouse. The sheet was initialized around the bone and was then allowed to shrink towards it. Parameters were set to first detect the outer surface of the bone, and then to continue detection of the interface between the cortical and trabecular bones (by adjusting the surface tension and GSV). The cortical and trabecular bones were separated (figure 65). This method can also provide the surface topography of the bone.

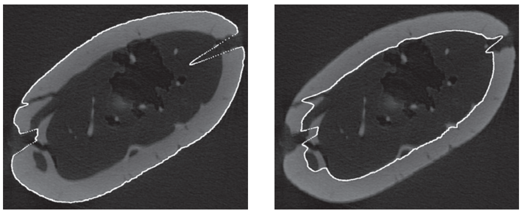

FIGURE 65 Left panel: The interface between the air and the cortical bone. Right panel: The interface between the cortical bone and the trabecular bone. Bone was embedded in PMMA, which cracked the bone while it was being cured. The white lines represent the locations of the sheet.

We obtained a nanotomographic X-ray image of a piece of a nuclear bomb (from the Thule accident in 1968). This particle was very porous and thus had a badly defined surface. The spherical version of the EW method was used to determine the surface. The qEW sheet was initialized around the particle and let to shrink towards its center, as shown in figure 66. This allowed us to determine the content of solids in the particle.

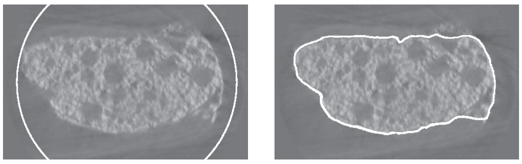

FIGURE 66 Cross-sectional image of segmentation of a nuclear particle. Left panel: the initial state of the spherical sheet. Right panel: the final segmented particle. The white lines represent the locations of the sheet.

A nano-tomographic image of a cell was obtained from Berkeley National Laboratory. To segment the nucleolus of the cell, we used the spherical version of the EW method. We applied the EW method to the gradient image as the edge of the nucleolus has both brighter and darker areas than the center of the nucleolus. In addition, we used a high surface tension to avoid the surface becoming stuck in the holes inside the nucleolus. The results are shown in figure 67.

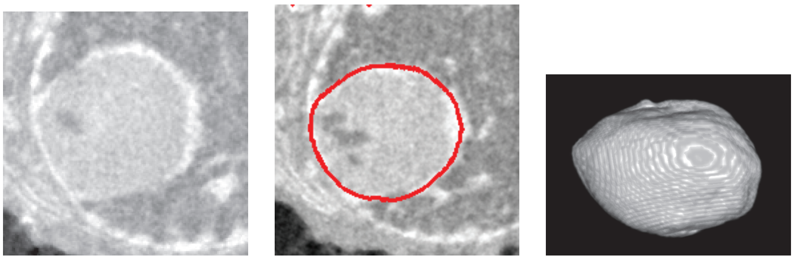

FIGURE 67 Left panel: cross-sectional image of the 3D stack of the cell nucleolus. Middle panel: cross-sectional image of the 3D stack; the cell nucleolus is marked. Right panel: 3D visualization of the segmented nucleolus.

5.3 Results

The methods reviewed by this study could all be easily performed in a reasonable amount of time using a desktop computer. We found the most crucial aspects of successful segmentation to be imaging and denoising. This was especially true for low-contrast samples, as the artefacts caused by the imaging system can seriously impair the segmentation process for these samples. However, denoising also plays an important role. A denoising method that sharpens the edges and smooths the flat areas effectively is essential for successful segmentation, especially when the imaging is not occurring in optimal conditions. Bilateral filter, anisotropic diffusion, and mean shift are all effective methods for denoising in this sense (Chapter 4). Mean shift is particularly useful, as it creates sharp edges; these edges make segmentation easier, as they create a less significant edge effect to the threshold selection.

With thresholding it is easy to add many kinds of priori information to ensure the obtained volumes are correct. The selection of the denoising method and threshold value plays a crucial role in establishing the reliability of the results. The results gathered in this chapter show that the selection of the denoising and segmentation method depends on the contrast between the background and objects, the size and shape of the objects to be analysed, and the artefacts in the image. As our first test indicated for simple data with large structures, good contrast, and clear distance between structures, almost any denoising method is sufficient. The volume and thickness of the objects are not greatly affected by of the denoising method chosen if an independent measurement is used. Each of the methods have their own benefits, for example, the smoothing methods can remove certain artefacts more better than other methods. However, the differences do become visible when small properties - such as the contact area — are analysed, as methods that cause more smooth make the detail (like gap between object) detectability also worse.

When analysing structures where the object size is altered the selection of the denoising method is very important. The results of the grainy sample indicate that all the edge-sensitive methods perform quite similarly. The non-edge sensitive-methods combine objects that are close to each others.

The most complicated process was the multiphase segmentation. During this process, the selection of the denoising method was most important for the low-contrast samples. The dense objects could be labelled using thresholding. However, the shadow artefacts caused by the dense objects were mixed with the gray values of the less dense objects, causing the gray values of the objects and background to overlap and also sometimes fade out the edges of the objects. Thus, it was impossible to use thresholding for these objects. Region growing type of segmentation was required, and while the method being quite simple, controlling the result (with the external measurement) become more complicated and the whole process more time consuming. Thus, in this situation, more advanced denoising methods are required.

Threshold methods are able to provide sufficient results when used with materials with good contrast. For low-contrast materials, region-based methods can be useful; however, these methods may require more work, as they usually involve some type of manual initialization. The structural segmentation method chosen was the watershed method; this method partitioned the structure from its local narrowing. This method is suitable for many uses, including pore space segmentation and the separation of many kinds of structures that are touching each other. When only one part of the structure is being segmented, the labour required for noise-tolerant methods is justified. We consider our EW equation-based method to be robust and useful for many different purposes.

6 IMAGE ANALYSIS

The process of CT imaging often aims to statistically analyse the material. This often means comparing several samples of similar material according their structural properties. Components that are typically analysed by CT imaging include morphology, material proportions, interfaces between the phases, connectivity, routes through the material, and structural or density changes. For the purpose of analysing particle/pore images, Schladitz [208], suggests the use of so-called intrinsic volumes – otherwise known as Minkowski functionals or quearmass integrals – to summarize the material properties of the image. In practice, these properties refer to volume, surface area, the integral mean curvature, and euler number. Intrinsic volumes can be used to find any additive property of an object [260]. Axelsson [13] described a complete set of properties that can be analysed of a porous sample. In addition to standard single pore measurements, a pore connectivity graph was found useful for finding flow-related values, such as tortuosity.

Additionally, the medial axis of the pore network allows us to perform various connectivity related analyses [184, 142, 273, 132]. Medial axis, distance transform, and thickness transform allow us to perform a simple simulation of liquid intrusion into the material as shown in [99, 58]. Fibrous materials have many properties of interest for scientists and according to [178] these remains perhaps the least understood material. In [178] the properties analysed are related in its strength, wetting behaviour, packing and flexibility. For fibrous structures, it is possible to approximate the fibre orientations using a variety of operations. The structure tensor is often used to find the orientation, as this method does not require the use of binarised data [125]. Axelsson [11] proposes the use of quadrature filters and structure tensors for fibre orientation analysis. In [25, 50], the fibre orientation results are obtained using a robust binary technique called mean intercept length. In [229], the following measurements were described for fibrous samples: fibre wall thickness, lumen thickness, degree of collapse, fibre length, free fibre length, slenderness ratio, fibre curl, and torsional resistance. Thickness of the structures can be analysed either by manual methods or by using local thickness transform [90]. The local thickness transform is not suitable for analysing hollow fibres, but it has been used for the analysis of bone, such as in [265] it can also be used to measure distances between the objects.

For fibre length analysis a path-opening method [148] has been used, such as in

[106]. The surface area of a sample can be calculated many ways. A common way is to use triangulation [145]. Triangulation has been applied to material research, such as for the analysis of [170] and stone [132]. Deformation analysis is a method where some sort of manipulation (compression/stretching/pending, heating/cooling, humidity/wetting) is performed, and the sample is imaged at the original and deformed stages. The present study was interested in investigating the structural changes that occur either due to direct (i.e., deformation field) or indirect (i.e., structural parameters) effects. The effect of compression on a Fontainebleau sandstone was studied in [66]. In [67] the displacement map of a compacted sugar is analysed in 3D using a digital volume correlation. In another study, XμCT imaging was used to measure water flooding inside a sandstone [213].

6.1 XμCT image characterization methods

Image characterization refers to operations that output numerical or statistical information from the image data. Histograms (see section 3.3.1), image moments (see section 3.3.1), and image correlation (see section 6.1.5) are methods that are often used to characterize structures. Some more specific characterization tools are described in the following sections.

6.1.1 Fast Marching method

The Fast Marching method is a numerical method for solving boundary value problems or boundary propagation problems. This method calculates the travel time of a surface as it passes through a specific point in space. The starting points used may be freely initialized in space, and the curve propagates toward its outer normals. The speed of the surface may be dependent on the material (i.e., the gray value of the voxel). This method is explained in detail in [212]. It is based on the Eikonal equation:

$$F(\mathbf{v})|\nabla T(\mathbf{v})| = 1.$$

This method is used to solve the evolution of a closed curve. This is done by finding the function of time T, which describes when the curve passes through a given point. The starting points of the curve are given and the curve front moves towards its normal direction until the whole T is determined. According to Eikonal equation, the gradient of T is inversely proportional to the speed of the front. The speed function F can, in practice, be an image.

The method is a simplified version of level-set method, it performs faster as only outward flow from the seeding area is allowed. The algorithm uses a narrow-band method to limit the calculation only to the relevant area. The relevant area is established by tagging the grid points as either *accepted*, *neighbours* or *far away*. The points in the *accepted* group are locked and cannot be processed again. The points in the *far away* region are not immediately processed, as they are too far away to be of any relevance. As soon as they become close enough, these points are moved to the *neighbour* group. The points in the *neighbour* group are processed until they are moved to the *accepted* group.

The main idea of the Fast Marching algorithm is that the information propagates from smaller values of T to larger ones. This means that the container for the *neighbours* must be ordered ordered in such a way that the lowest T value can be found quickly. In cases where constant speed are used a histogram-type point container is effective. The histogram-type container is a two-dimensional queue in which the first index includes the T value and the second index includes the points that have the T value. In the case of $F = 1$ we can store the T values in power of two which means they are all integer values. By keeping track of the smallest stored value, we can restore the smallest point very quickly without needing to sort the container.

The T at point $\mathbf{v}$ is approximated using the following scheme:

$$\begin{aligned}1/F[\mathbf{v}]^2 =& max(max(\Delta^x_{[0,1]}T[\mathbf{v}],0),-min(\Delta^x_{[1,0]}T[\mathbf{v}],0))^2\\ &+max(max(\Delta^y_{[0,1]}T[\mathbf{v}],0),-min(\Delta^y_{[1,0]}T[\mathbf{v}],0))^2\\ &+max(max(\Delta^z_{[0,1]}T[\mathbf{v}],0),-min(\Delta^z_{[1,0]}T[\mathbf{v}],0))^2.\end{aligned}\tag{38}$$

The algorithm itself contains the following steps:

Algorithm 9 Fast Marching Method 3D

```
1: Initialization: Set the starting points $V_A$ as accepted. Set $T = 0$ for all points in $V_A$. Set the narrow band $V_N$ points (All $\mathcal{C}_6[V_A]$ points). Set $T = 1/F(x)$ for all points in $V_N$. Let all the other points be far away points. Set $T = \inf$ for all the points in far away.
2: while $V_N$ is not empty do
3:     Take point $\mathbf{v}$ with smallest $T$ value from $V_N$.
4:     Add $\mathbf{v}$ to $V_A$ and remove it from $V_N$.
5:     Gather all the 6-connected neighbours that are either on narrow band or far away. If neighbour is far away, move it to $V_N$.
6:     Recompute the values of $T$ at all neighbours according to equation (38) and select the largest possible solution to the quadratic equation.
7: end while
```

At step 6 the calculation of T is done by finding a solution that satisfies the equation (38). The solution is proven in detail in [212]. Here, we briefly describe how to find the solution at point $[i, j, k]$. Let $f = 1/F$ and

$$\begin{aligned}t =& \{\min(T[i-1, j, k], T[i+1, j, k]),\\ &\min(T[i, j-1, k], T[i, j+1, k]),\\ &\min(T[i, j, k-1], T[i, j, k+1])\}.\end{aligned}$$

We define $t_1 = \min(t)$, $t_2 = \min(t \setminus \{t_1\})$, and $t_3 = \min(t \setminus \{t_1, t_2\})$. Now

$$T = \begin{cases} t_1 + f & \text{if } t_1 + f < t_2,\\ \max\left(\frac{-b_1+\sqrt{d_1}}{4}, \frac{-b_1-\sqrt{d_1}}{4}\right) & \text{if } t_1 + f < t_3,\\ \max\left(\frac{-b_2+\sqrt{d_2}}{6}, \frac{-b_2-\sqrt{d_2}}{6}\right) & \text{if } t_1 + f \geq t_3,\end{cases}$$

where $b_1 = -2t_1 - 2t_2$, $d_1 = b_1^2 - 8(t_1^2 + t_2^2 - f^2)$, $b_2 = -2t_1 - 2t_2 - 2t_3$, and $d_2 = b_2^2 - 12(t_1^2 + t_2^2 + t_3^2 - f^2)$.

6.1.2 Local Thickness Transform

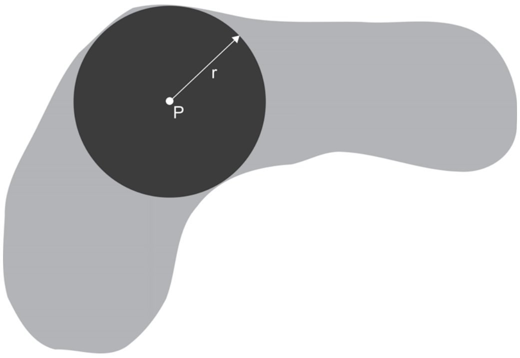

FIGURE 68 The principle of the local thickness analysis. Voxels get the distance value, which is the diameter of the largest sphere that fits inside the object and contains the voxel. If the dark sphere is the largest sphere that fits inside the structure, all the voxels inside the sphere will get $2r$ as their value, unless there is a larger sphere that also contains that voxel.

Local thickness is a distance transform-related operation that was first introduced in 3D in [90]. Let A be a binary image with two voxel classes: object and background. The local thickness transform converts a binary image into a thickness presentation, where the gray value of each object voxel is the radius of the maximal sphere that can be fitted into that locality, and which includes that voxel (see figure 69 for an example). A maximal sphere is the largest possible sphere that can be fitted inside the object such that it does not contain any void voxels (see figure 68). As a result of the transform, each voxel gets a value that is the same as the diameter of the largest sphere that can fit inside the object and contain that voxel.

The implementation of the local thickness transform in 3D is performed in three steps (see Algorithm 10). First, the data is distance transformed. The result of the DT is an image that describes the largest sphere that can be fit into the locality of that voxel. The second step is to discard the spheres that are included by larger ones. Done this way, the second step of implementation has very high computation demands and is quite inefficient. To improve its efficiency, this step can be optimized by finding the median axis of the distance image; then, the points that are not found on the median access can be determined as being part of the larger spheres [90]. The median axis can be found by finding the so-called "distance ridge" from the DT. Fitting the spheres only to the relevant points can significantly reduce the amount of calculation required.

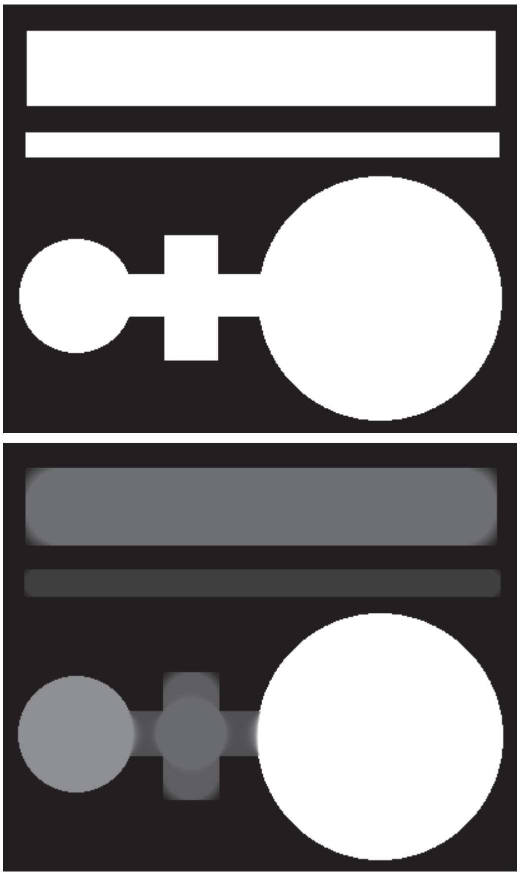

FIGURE 69 Top: the original image. Bottom: the local thickness transform applied to the original image. The gray value represents the local thickness value.

6.1.3 Affine region detector

Structure tensor [29] and *Hessian shape descriptor* [165] are methods used to determine orientation and simple shapes, such as tubes, blobs, or sheets, in gray value or binary images. The methods are based on analysing the eigenvalues of a matrix constructed from the gradient information of the image. For structure tensor, the matrix, at each voxel $\mathbf{v}$ at image a, is constructed as:

$$J[\mathbf{v}] = \sum_{\mathbf{q} \in \mathcal{N}[\mathbf{v}]} w(\mathbf{q}) \begin{bmatrix} (\frac{\partial a}{\partial x}[u])^2 & \frac{\partial a}{\partial x}[u] \cdot \frac{\partial a}{\partial y}[u] & \frac{\partial a}{\partial x}[u] \cdot \frac{\partial a}{\partial z}[u] \\ \frac{\partial a}{\partial y}[u] \cdot \frac{\partial a}{\partial x}[u] & (\frac{\partial a}{\partial y}[u])^2 & \frac{\partial a}{\partial y}[u] \cdot \frac{\partial a}{\partial z}[u] \\ \frac{\partial a}{\partial z}[u] \cdot \frac{\partial a}{\partial x}[u] & \frac{\partial a}{\partial y}[u] \cdot \frac{\partial a}{\partial z}[u] & (\frac{\partial a}{\partial z}[u])^2 \end{bmatrix},$$

where $u = \mathbf{v} - \mathbf{q}$. The purpose of weighting (windowing) with w is to allow the different scales of structures to be detected. w is often chosen to be Gaussian [250, 249].

For the Hessian shape descriptor, the matrix is as follows:

Algorithm 10 Local thickness transform

```
Let $a$ be a binary image.
Let $a_{dt}$ be distance map of $a$.
Remove all the points from $a_{dt}$ that are not at the ridge. See ref. [141] for more details.
Define the local thickness at each point belonging to the ridge. The local thickness can be found using the distance map $a_{dt}$ (this value is the radius of the maximum sphere).
```

$$H(\mathbf{v}) = \begin{bmatrix} \frac{\partial^2 a}{\partial x^2}[\mathbf{v}] & \frac{\partial^2 a}{\partial x \partial y}[\mathbf{v}] & \frac{\partial^2 a}{\partial x \partial z}[\mathbf{v}] \\ \frac{\partial^2 a}{\partial y \partial x}[\mathbf{v}] & \frac{\partial^2 a}{\partial y^2}[\mathbf{v}] & \frac{\partial^2 a}{\partial y \partial z}[\mathbf{v}] \\ \frac{\partial^2 a}{\partial z \partial x}[\mathbf{v}] & \frac{\partial^2 a}{\partial z \partial y}[\mathbf{v}] & \frac{\partial^2 a}{\partial z^2}[\mathbf{v}] \end{bmatrix}.$$

To make the Hessian shape descriptor sensitive to a certain sized objects and to avoid artefacts caused by image noise, Gaussian filtering is used to smooth the image data so that the details below the desired size scale are removed. For multi-scale detection, the shape descriptor needs to be applied to the scale space (a cascade of Gaussian filtered images) representation. The scale space approach requires the user to know the size range of the objects of interest. Due to the commutative property of the Gaussian derivative operators, the derivatives can be determined in a scale space image as convolutions of the image using derivatives of the Gaussian kernel in the desired scales [224] to enhance the accuracy.

The eigenvalues $(\lambda_1, \lambda_2, \lambda_3)$ of matrix H can be solved using the algorithm described for the example in [221]. The eigenvalues are then used to define the local shape using the following rules (the -+ means value is close to zero, the - - value is negative, the ++ value is positive):

λ_1	λ_2	λ_3	Structure type
-+	-+	-+	Noise
-+	-+	- -	Bright sheet
-+	-+	++	Dark sheet
-+	- -	- -	Bright tube
-+	++	++	Dark tube
- -	- -	- -	Bright blob
++	++	++	Dark blob

For the Hessian shape descriptor to apply these rules to evaluate the abundance of certain shapes, various formulae have been proposed. Frangi's formula for the abundance of tubular shapes in the structure [68] is as follows:

$$V_\sigma(\lambda) = \begin{cases} 0 & \text{if } \lambda_2, \lambda_3 > 0, \\ (1 - e^{-\frac{R_A^2}{2\alpha^2}}) e^{-\frac{R_B^2}{2\beta^2}} (1 - e^{-\frac{S^2}{2\gamma^2}}) & \text{otherwise,} \end{cases} \tag{39}$$

where $R_A = \frac{|\lambda_2|}{|\lambda_3|}$ (sheetness), $R_B = \frac{|\lambda_1|}{\sqrt{\lambda_2 \lambda_3}}$ (blobness), and $S = \sqrt{\lambda_1^2 + \lambda_2^2 + \lambda_3^2}$ (noise). Parameters α, β, and γ are defined by the user. In figure 70 the results of applying this formula to an image of blood vessels in the brain is shown. Equation (39) can be adapted for extraction of blob like structures by replacing $e^{-\frac{R_B^2}{2\beta^2}}$ with $1 - e^{-\frac{R_B^2}{2\beta^2}}$. This means, in essence, that all eigenvalues have a similar magnitude. Also the trace of H is strongly correlated with the abundance of blobs. For the multi-scale sheetness various formulae has been proposed; for example in [4, 55]:

$$S_\sigma(\lambda) = \begin{cases} 0 & \text{if } \lambda_3 > 0, \\ (e^{-\frac{-R_A^2}{2\alpha^2}}) \cdot (1 - e^{-\frac{R_{B2}^2}{2\beta^2}}) \cdot (1 - e^{-\frac{S^2}{2\gamma^2}}) & \text{otherwise,} \end{cases} \tag{40}$$

where $R_{B2} = \frac{|(2|\lambda_3| - |\lambda_2| - |\lambda_1|)|}{|\lambda_3|}$ is another blobness measurement.

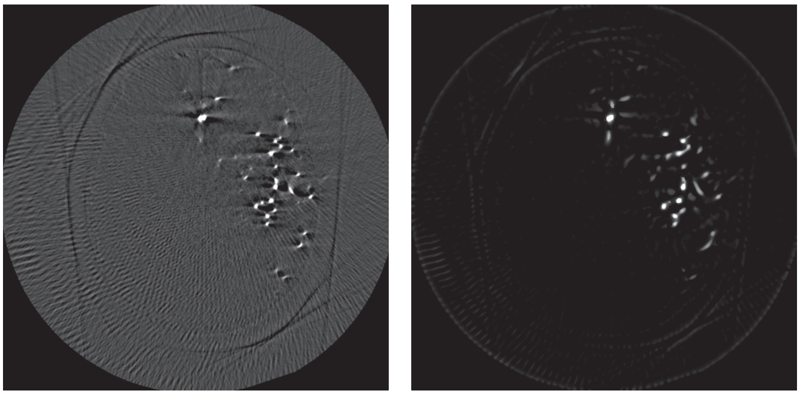

FIGURE 70 On the left is a cross section of the original image of blood vessels in the brain. On the right is the map of Hessian coefficients by the above formula for the same cross section.

The difference between the structure tensor and Hessian shape descriptor is that the former is based on first order variations; the response is strong at boundaries. Whereas the latter is based on the second order variations; it responds more at the inside of the structure [55].

In addition to shape detection, the both structure tensor and Hessian shape detector can be used to find the orientation of the structures. The shortest eigenvector points to the direction of the slowest gray value change and thus marks the orientation of the structure. In figure 71 the orientation analysis is demonstrated using an artificial test pattern.

6.1.4 Surface Area Estimation

The surface area of a 3D object is a measured based on how much of the object's area is exposed to other material phases. Accurately calculating the surface area is complicated because continuous data are presented on a discrete grid (see in figure 72). The real shape of the object is approximated by square blocks. Digitalization is a one way transform; a digitalized shape can be produced from any object, although, the real shape of the object cannot be determined from a digitalized shape. Thus, the surface area analysis is always

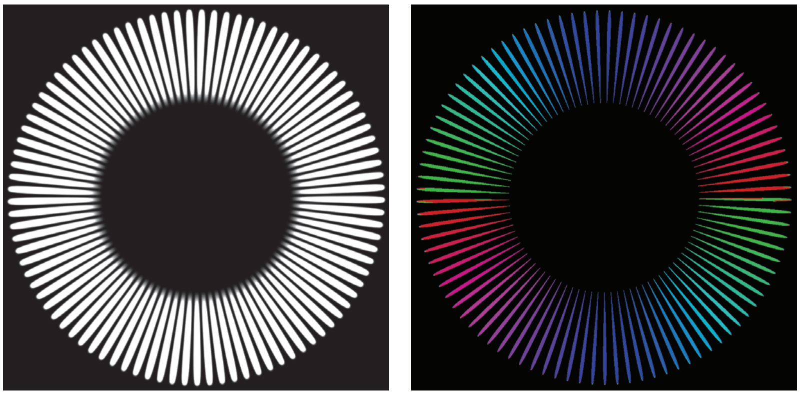

FIGURE 71 Orientation analysis of a test pattern. The test pattern is on the left and the right image shows color-coded orientation after analysis.

done within certain accuracy limitations [160], because how the border actually behaves in each locality must be approximated.

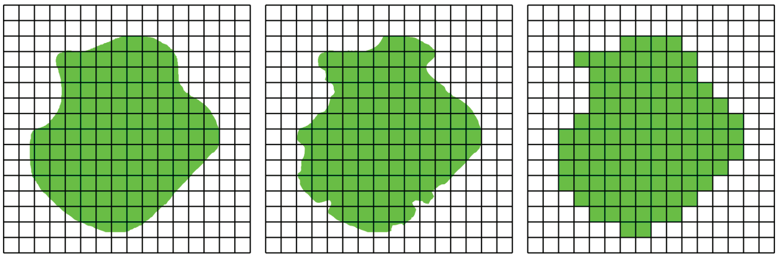

FIGURE 72 On the left is the original data, in the middle is the modified original data, and on the left is the discretised version of both data sets using a Gaussian digitization. The original and modified data obviously have different real surface areas but the discretised version is still the same.

Various methods approximate the surface area; the most simple way is to calculate the number of voxels between a solid and a void. However this method underestimates surface area and provides different values depending on the orientation of the image.

One way to calculate the surface area is to use marching cubes [145] to obtain a polygonal mesh of the voxel data and then adding area of the triangles. This method has a maximal asymptotic error of 12.8% [117]. A version with optimized weights for each configuration was published 2005 by Lindblad [140], yielding a 7.3% maximum asymptotic error. The improved version uses weighted local voxel configurations. A 2 x 2 x 2 matrix is shifted over the object, and the local configuration is determined according to which 8 voxels are solid and which are void. This leads to 2^8 possibilities, but when taking into the account the rotation symmetry and complementary cases, the configurations can be reduced to 14. Each configuration has its own weight, and the sum of these weights determines the total surface area of the object.

A statistical approach for surface area estimation uses the Cauchy-Crofton formula (see [144] for more details). Consider a 3D object O with a boundary S and a surface area of s. L is a group of all possible lines l in $\mathbb{R}^3$ and dL_i is the density of all lines intersecting the surface. The Cauchy-Crofton formula can now be written as

$$\int_{l \in L} w_l dL_i = \pi s, \tag{41}$$

where w_l is the number of intersection points of the given line l with the surface. Next, the reference object O_r is considered alongside the boundary S_r to determine the surface area s_r, letting O be contained by O_r. Consider a set ι of m lines that are randomly sampled from the set of lines that intersect O_r. Let n_s and n_r be the total number of intersection points with ι S, and S_r respectively. Now equation (41) is:

$$\frac{n_s}{N} \approx c\pi s \quad \text{and} \quad \frac{n_r}{N} \approx c\pi s_r.$$

By combining these s can be estimated by:

$$s \approx \frac{n_s}{n_r} s_r. \tag{42}$$

An algorithm [144] to find surface area of an object is given in Algorithm 11.

Algorithm 11 Surface area estimation

```
1: Generate a reference object $O_r$ containing $O$. This can be, for example, minimum sphere that contains $O$. The Gartner miniball method is suggested in [75].
2: Generate a set $\iota$ of uniformly distributed lines that sample the set of all lines intersecting the reference object $O_r$. To accomplish this low-discrepancy sequences are used.
3: Compute $n_s$ and $n_r$.
4: Use equation (42) to estimate the surface area of $s$.
```

6.1.5 Image Correlation

Correlation is mathematically related to image convolution (see section 4.1.1). For function f, the correlation with signal g can be expressed as:

$$(f * g)(t) = \int_{-\infty}^{\infty} f(\tau) g(t + \tau) d\tau.$$

The local maximum of $(f * g)(t)$ gives the translation for where the images best match. To obtain subpixel accuracy, interpolation should be used. For fast correlations, FFT can be used to calculate the convolution in $\mathrm{O}(N \log N)$ time.

Autocorrelation is the correlation of an image with a translated version of itself. It can be used to find repeating patterns in the image and determine the orientation distribution of elongated structures [195]. Autocorrelation can be defined using the following equation:

$$R(a,b,c) = \sum_{i=-\infty}^{\infty} \sum_{j=-\infty}^{\infty} \sum_{k=-\infty}^{\infty} a[i,j,k] \cdot a[i-a, j-b, k-c],$$

where a, b, and c represent the translation of f in x, y, and z directions respectively.

Image similarity

Let a be the original image and b be image to correlate with a; the problem is to determine how similar the images are. To accomplish this a similarity measurement between the two images must be defined. Various similarity measurements have been proposed and reviewed ([133, 181]). The similarity measurements can be roughly divided into feature-based and intensity-based [133]. In the feature-based approaches the image information is converted into features that are located in all images to be correlated. This makes the algorithm fast, but finding the mutual features is automatically is difficult. The intensity-based methods compare the voxel values directly and calculate a statistical value representing the similarity. These typically require more computation but can be easily automated. The intensity-based methods are usually based on a normalized cross correlation:

$$C(a,b) = \frac{\sum_{\mathbf{v}\in\Omega}(a[\mathbf{v}] - \mathrm{Ave}(a))(b[\mathbf{v}] - \mathrm{Ave}(b))}{\mathrm{Var}(a)\mathrm{Var}(b)}.$$

Other measurement for the similarity is the sum of absolute difference values:

$$A(a,b) = \sum_{\mathbf{v}\in\Omega}(|a[\mathbf{v}] - b[\mathbf{v}|).$$

This can be normalized to a 0–1 range by dividing it with the maximum allowed gray value multiplied by the total number of voxels. In addition to the plain sum standard deviation, entropy, and the histogram standard deviation of the difference image are used [133].

6.2 General Analysis

In this section a few general analysis methods are defined. As noted in Chapter 5, the segmentation process separates the interesting areas for analysis in this phase. The success of the segmentation process depends on the image quality. If successful, the separation of objects in interest was possible and analysis of those objects individually can be done. However, if the quality of the image does not allow the segmentation of the objects, in some cases, the analysis of shapes can be approximated using other methods. In this section we define few general purpose 3D image analysis methods.

6.2.1 Porosity

Porosity is the percentage of void volume in a whole sample. This is one of the most basic analyses that can be easily performed. In general, there are three possibilities for the segmentation: cropping the sample so that the outside is not in image area, labelling the image so that internal and external pore space is individually labelled, and defining the shape of the object for use as a mask.

To calculate the porosity, there are a few possibilities. From segmented images void voxels inside the sample and the total voxels of the sample are calculated. Additionally it can be defined directly from the histogram if the threshold value is known.

6.2.2 Analysis of local thickness

Many analyses or structural segmentation methods (see Chapter 5) are based on analysis of object diameter. There are several methods for finding the diameter of an object [45] such as morphological opening (granulometry) or the local thickness transform. See figure 73 for an example of results obtained with these methods. These methods work especially well on tubular shapes. As the algorithm finds the maximum sphere that fits completely inside the sample (see figure 68) it will underestimate objects with sharp corners or oval shape. Despite this, it is a general purpose tool for both segmenting objects of different thickness and analysing the thickness of the objects. Additionally, skeleton combined with EDT can be used to analyse the thickness of structures to provide results for spherical, plate-like, cylindrical, tubular, and many other shapes.

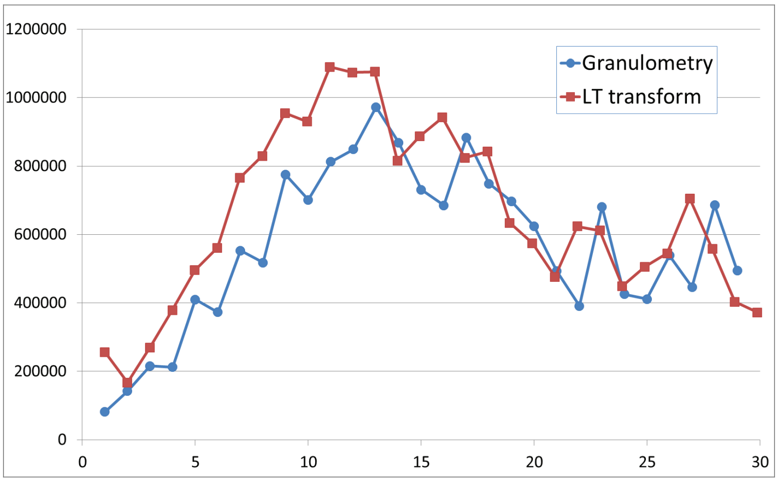

FIGURE 73 The pore thickness distribution of a volcanic stone sample obtained using granulometry and the local thickness transform.

6.2.3 Z-projection

Projection of certain values (like porosity, density, maximal particle size) along one of the 3D axis is a robust and simple tool to show information about the sample structure. Different types, like mean, maximum, minimum, or standard deviation value, can be used for the projection. If combined with segmented or labelled images it can provide information, such as pore count, mean fibre orientation, porosity, or tortuosity, as a function of plane depth. An example of a such a z-profile is given in figure 74.

6.2.4 Histograms

Gray value histograms are typically used in XμCT is to analyse a material volumes inside a sample. In figure 75 you can see a typical histogram of a 3D image of coated paper. The image has three phases: air, base paper, and the coating layer, seen as peaks in the histogram.

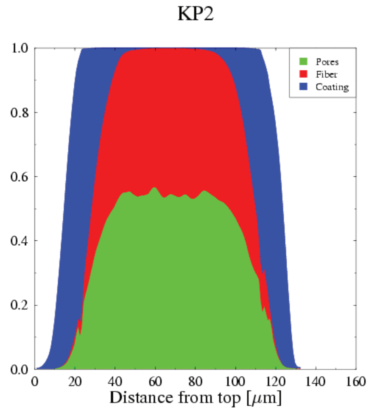

FIGURE 74 Z z-profile of labelled paper sample showing the portions of coating, fibre, and pore space as a function of depth in z-axis.

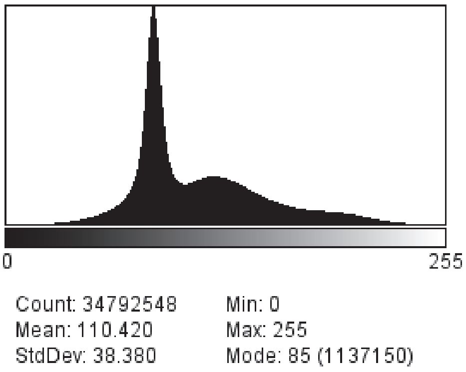

```
Count: 34792548    Min: 0
Mean: 110.420      Max: 255
StdDev: 38.380     Mode: 85 (1137150)
```

FIGURE 75 Gray value histogram of a coated paper sample.

Multidimensional histograms can be used to find internal structural correlations for an image. For example, a previously mentioned histogram combined a distance transform and density information. figure 76 shows a 2D histogram where x-axis is the shortest distance from the void phase (distance transform) and the y-axis is the density.

From this histogram we can say that the more dense areas are further away from the void, they are more inside the sample.

6.2.5 Distance Through Material

The fast marching method (section 6.1.1) can be used to define the time it takes to travel from a given start point or start points to the connected material points in image. For example, it if someone dropped a stone into water, the fast marching method would calculate when the front of the waves would arrive at other points of the water container. If the velocity is constant the distance can be calculated from the arrival time values. Additionally, is is possible to have a variable velocity that changes, for example, according to the local

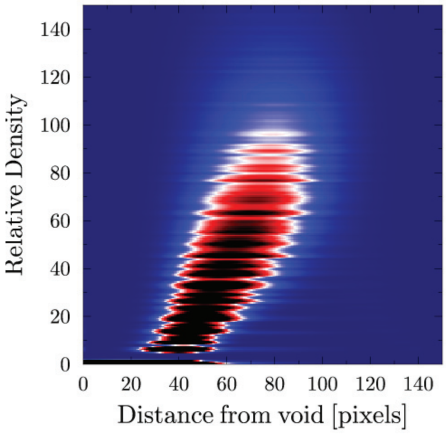

FIGURE 76 A distance-density histogram for a porous stone sample. Gray values represent the count. The histogram reveals that the more dense areas of the image are closer to the inside of the sample.

thickness of the material (which could be useful for simulating liquid transportation).

figure 77 shows two cross-sectional time maps (with a constant velocity) of fibrous material, where the start points were at the bottom of the image, and the fast-marching method was used to define the distance to the top of the stack. Further more, this can be used to define the distances or routes through the material.

6.2.6 Rigid Shape Transforms

Transforms inside an object, such as twists or object translations can be analysed using image correlation. The analysis can be performed for whole images or by cropping to certain areas. In some cases filtering (e.g., the Gaussian filter) can add robustness to the method.

For twist analyses, the center of rotation must be defined, which is often the same as the center of mass. When the center of rotation is known, the image correlation is defined a function of the rotation angle. The maximal correlation value reveals the rotation angle.

For object translation, similar procedures may be used. For more complex transforms, the optical flow [228] algorithm is used to find the local transformation vectors.

6.3 Porous and Particle Material

Pore and particle analyses are similar to each other as in both we have a group of individual objects (pores and particles), that are usually touching. As a results of the analysis we commonly want a distribution of certain properties for the individual objects. In practice, there are two options:

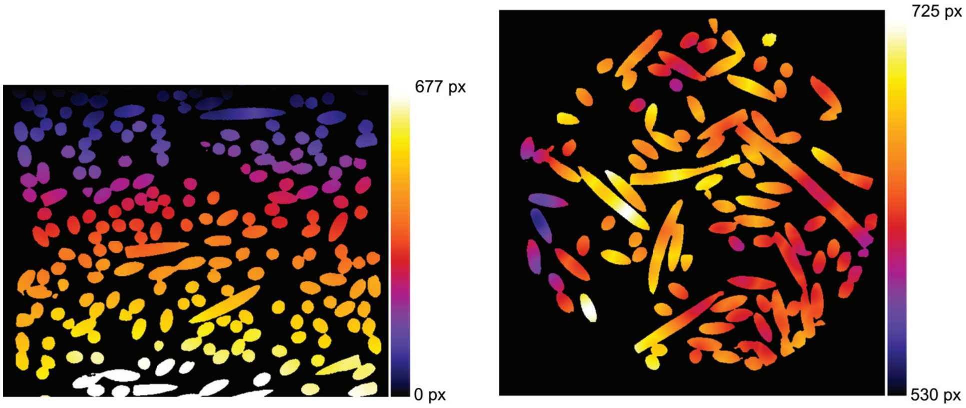

(a) Sideview

(b) Crossectional view.

FIGURE 77 The result of fast marching method to a fibrous sample. The seed points were at bottom slice of the image. At figure 77a is shown the distance from “side view”, at figure 77b is shown the cross-sectional distance map of the top-most slice.

- Separate the structure into individual objects and analyse each object separately to obtain the distribution.
- Approximate the distribution using an analysis method that does not require separation of the distribution (e.g. the local thickness transform).

Structural segmentation is easy to obtain for objects that are not touching each other. For pores or particles that are connected, the watershed segmentation can be used to split the structure into individual objects. When using the watershed transform, the definition of a pore is that it is a space limited by local structural narrowings. For some structures, a K-means clustering can be used to split the structure into equally spaced and similar sized particles. See figure 78 for an example of both of the segmentation results.

The surface of a porous material can be difficult to determine due to the surface pores. There is no explicit way to define whether a cavity at the surface of the material is pore or hole. The rolling ball algorithm [226] or the surface segmentation tool defined at section 5.1.2 can be used for this purpose.

6.3.1 Analysis of individual pores / particles

CT images allow us calculations of various parameters for each individual pore or particle ([12]). For labelled images, the following parameters for each pore and particle can be defined:

- **Center of mass** can be calculated using 3D image moments. See section 3.3.1.
- **Volume** can be analysed by calculating the number of voxels inside the pore or particle using a flood fill algorithm. the volume is also M_{000} moment of the image. See section 3.3.1.
- **Orientation** can be approximated using the image moments. See section 3.3.1.

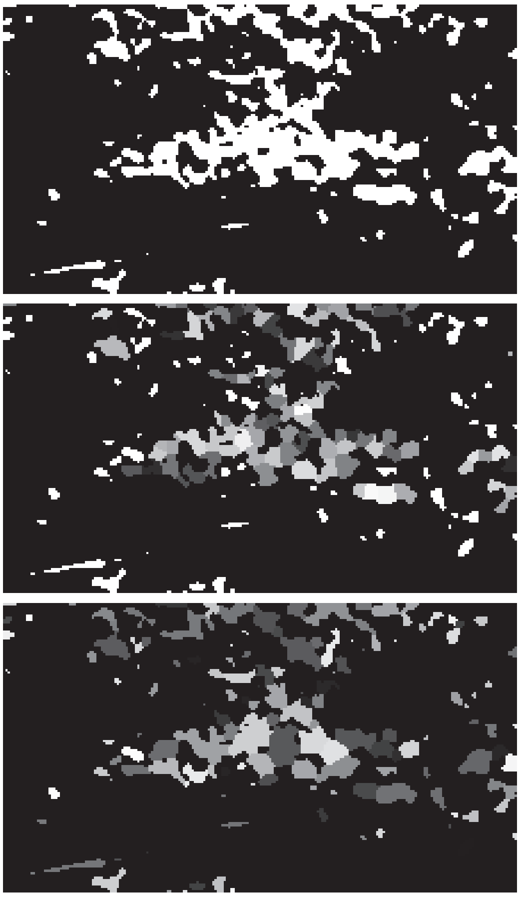

FIGURE 78 The first row shows the original image, the second row shows the result of cluster segmentation (where the number of clusters is approximated from the volume of the object), and the third row shows the watershed segmentation of a particle sample.

- **Surface area** can be determined using surface triangulation. See section 6.1.4.

- **The number of connected components** can be defined from samples in which the particles are touching each other. The number of neighbours can be extracted by analysing the outer edge of the pore defined by the flood fill algorithm.

- **The area of the interfaces** can be defined by using the surface area calculation for the interface area only. See section 6.1.4.

- **The number of holes inside** a object can be calculated using the flood fill algorithm to fill the connected void space from outside the object. The unconnected void space defines the holes inside the particles.

- **The shape** of the object can be described using many methods. One is to define the sphericity, using $\Psi = \frac{\sqrt[3]{36\pi V^2}}{A}$, where V is the volume of the object and A is the surface area of the object. An other option is to define statistical parameters from the distance between the center of mass and the outer edge of the particle.

6.3.2 Analysis of Pore Network

The labelled connected object network can be divided into a graph presentation, where objects define the pores and links are the throats between the pores. This graph allows a simple physical simulations of the structure. For example, non-wetting liquid penetration into the pore space can be analysed this way. The basic physical phenomenon affecting liquid intrusion into the material is surface tension. A certain force is required for a non-wetting liquid to overcome the capillary pressure in an opening of a given size in the pore structure. The relation between the external pressure P and the size r (radius) of the opening is determined using the Washburn equation:

$$Pr = -2\gamma \cos\theta,$$

where γ is the surface tension and θ the contact angle of the liquid. Both γ and θ are usually assumed to be constants, and the size of the opening is directly related to the external pressure, $r = -2\gamma \cos\theta / P$. This result assumes that pores are cylindrical capillaries.

To simulate liquid intrusion, a virtual pressure is used to push liquid into the structure. Throat size (links) limits the movement according to the given pressure. When the pressure limit is reached, the space behind the links are filled until a throat with a smaller radius is found. This is similar to mercury intrusion porosimetry (MIP), which is a common way to experimentally measure the pore size distribution of a material. The pore size distribution is obtained by letting mercury intrude the sample for increasing values of pressure, so that the mercury will penetrate increasingly smaller openings in the pore structure. The amount of pores accessible for a given opening can then be calculated from the volume of the mercury at each pressure step. MIP measurement has two phases. During the intrusion phase, the external pressure is gradually increased and pores behind openings of gradually decreasing size will be filled. This process is called invasion percolation. Opening here refers to the interface between two pores. During the extrusion phase, the pores are emptied when the external pressure is decreased. According to the Washburn equation, the smallest pores have the highest capillary pressure pushing the liquid out of the pore (i.e., the smallest pores are emptied first). The liquid intrusion can also be simulated using, e.q., the Lattice-Boltzmann (LB) method. However, this is very time consuming and requires high performance computing facilities. The graph-based method is lightweight and fast in comparison.

The intrusion phase is initialized by choosing the initial area of the liquid. All the voxels belonging to this area are marked as the liquid front. The algorithm fills the volume using the liquid front as a starting area, and the throat thickness to limit the filling to certain radius (expanding the front). This process is continued for decreasing sizes of openings (corresponding to the gradually increasing pressure of the intruding liquid) until the whole pore space is filled. The extrusion step is initiated by analysing the sizes of the pores in the whole pore space. The smallest pores are extruded first. The assumption is that a pore is emptied (when its size allow) only if it has a liquid connection to the sample surface. Therefore, a certain amount of liquid will be trapped inside the sample and the liquid connection may get broken

The graph representation allows also analysis of the tortuosity by calculating the routes through the material from the nodes. Tortuosity is a measurement that defines how complex the paths through the pore network are, and it is defined as:

$$\tau = \frac{R_{\text{ave}}}{D},$$

where R_{ave} is the length of an average route between the two surfaces, and D is the Euclidean distance between the surfaces.

6.3.3 Pore structure analysis

When the pore structure cannot be split into individual pores, few another analysis methods can be applied. To obtain an approximation of the pore size distribution, the local thickness transform (see section 6.1.2) or granulometry (see section 3.3.2) can be applied. Those give a volume-radius curve of the structure. Additionally similar liquid intrusion simulation (MIP) can be performed by using the radius defined by the local thickness transform to limit the flood fill. The liquid front is defined by the user, and the intrusion is simulated using flood fill to fill the space until all voxels connected to the liquid front that have larger gray values (in thickness map) than the given limit are filled. Then the gray value is decreased and the flood fill is performed again. The starting value is the largest gray value found from the initialized front.

6.4 Fibrous Material

CT images allow us calculations of various parameters for fibrous materials, such as fibre length, volume fraction, aspect ratio and orientation. The binarisation of fibrous samples is usually simple because it is usually composed of only two materials. However, to keep the correct thickness of the fibres can require an usage of an external measurements as the beam hardening and the point spread function can cause the fibre edge to be smooth. For example, a microscope can be used to determine the fibre thickness to be used as an independent measurement for segmentation.

The segmentation of individual fibres is difficult for hollow natural fibres because they tend to break easily, causing shapes that are not easy to model. For fibres that keep their shape, segmentation of individual fibres can be realized using graph cuts such as in [259], by following the lumen of the fibres [10], or by using skeletonization. In addition, morphological tools can provide a way to segment the fibres. A simple morphological segmentation of non-hollow touching fibres is shown in Algorithm 12

The algorithm assumes all the fibres are of similar thickness and that there is some separation between them even though they may touch each other. For optimal watershed transformation, each object requires exactly one seed. On digitized tubular structures, these local maxima are seldom continuous inside an individual tube due to inaccuracies in the discretisation. The inaccuracies create small variations in tube thickness that cause the local maxima of EDT vary across the length of the tube, which in turn cause more

Algorithm 12 Morphological separation

```
1: Binarise the fibres (using tools provided in Chapters 4 and 5). See figure 79a for a
   visual demonstration.
2: Perform distance transform (see section 3.3.2). The maxima of the distance trans-
   form are ridges that follow the center lines of the fibres. See figure 79b for visual
   demonstration.
3: Use the geodesic reconstruction algorithm (see section 3.3.3) to flatten small varia-
   tions of the ridges caused by small thickness differences in the fibres. See figure 79c
   for a visual demonstration.
4: Generate a seed image that contains the top part of each ridge by thresholding the
   reconstructed distance transform. See figure 79d for a visual demonstration.
5: Use the watershed segmentation with previously generated seeds to separate the indi-
   vidual fibres. See figure 79e for a visual demonstration.
```

than one seed into each tube. To remove this problem the geodesic reconstruction [253] is applied. The effect of this transform is that all neighbouring local maxima that are maximum of h gray values different from each other are connected to each other. In essence, the small variations at the center lines of the tubes in EDT are combined.

For segmentation of fibres of various diameters, either the fibre wall thickness or fibre thickness, the local thickness transform (see section 6.1.2) is an efficient method. figure 80 shows an example of such a segmentation.

The success of segmentation of individual fibres is highly dependent of the type of the fibres. For good quality fibres (round, symmetrical, whole, low fibre density) segmentation is possible to do using several different approaches (see section 5). When individual fibres are separated, similar measurements as those used for pores and particles can be used to define the properties. For samples that are not easy to label, such as broken or deformed fibres, the segmentation results are easily low quality and can not be used for analysis.

However, number of other analyses can be performed for fibre material without segmenting the individual fibres. In [59], an analytic model for number of contacts in a planar fibrous network is determined using an average shortest path through the sample in the out-of-plane direction. The shortest path was calculated using a chamfer distance transform, although a more precise length could be obtained using the fast marching method. To analyse fibre orientation, the methods from section 6.1.3 can be used. To demonstrate the usage, the orientation analysis for the sample in section 5.2.1 was performed using structure tensor. The results are visualized in figure 81. The fibre length distribution can be analysed using a method called path opening [148, 163, 43], which is a modification of granulometry, where the opening operations are performed length-wise taking into account the shape of the object.

(a) Binary image (b) Distance transform (c) Geodesic reconstruction

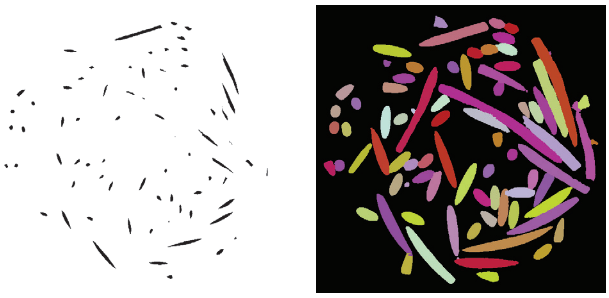

(d) Seeds (e) Result

FIGURE 79 Cross-sectional images of the fibre segmentation procedure.

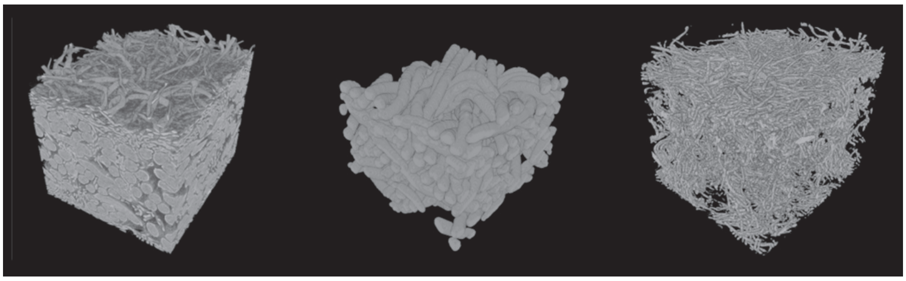

FIGURE 80 Segmentation of fibres according to their thickness. The left image shows the center of the thick fibres in the original image, the right image shows the thin fibres of the original image.

6.5 Fluid Flow Simulations

XμCT can be used to obtain realistic geometries of various materials for computational fluid dynamics. Computational fluid dynamics allows the use of direct voxel geometry for simulations and to obtain, e.g., the permeability value for a given material. Permeability is a measure of the ability of a material to transmit fluids. Many methods for the simulations exits and while they are not discussed in detail here, the processes for obtaining geometries for simulations are described. This research utilized a LB simulation directly to the binary voxel data. In other models a 3D triangulated geometry is preferred, although few

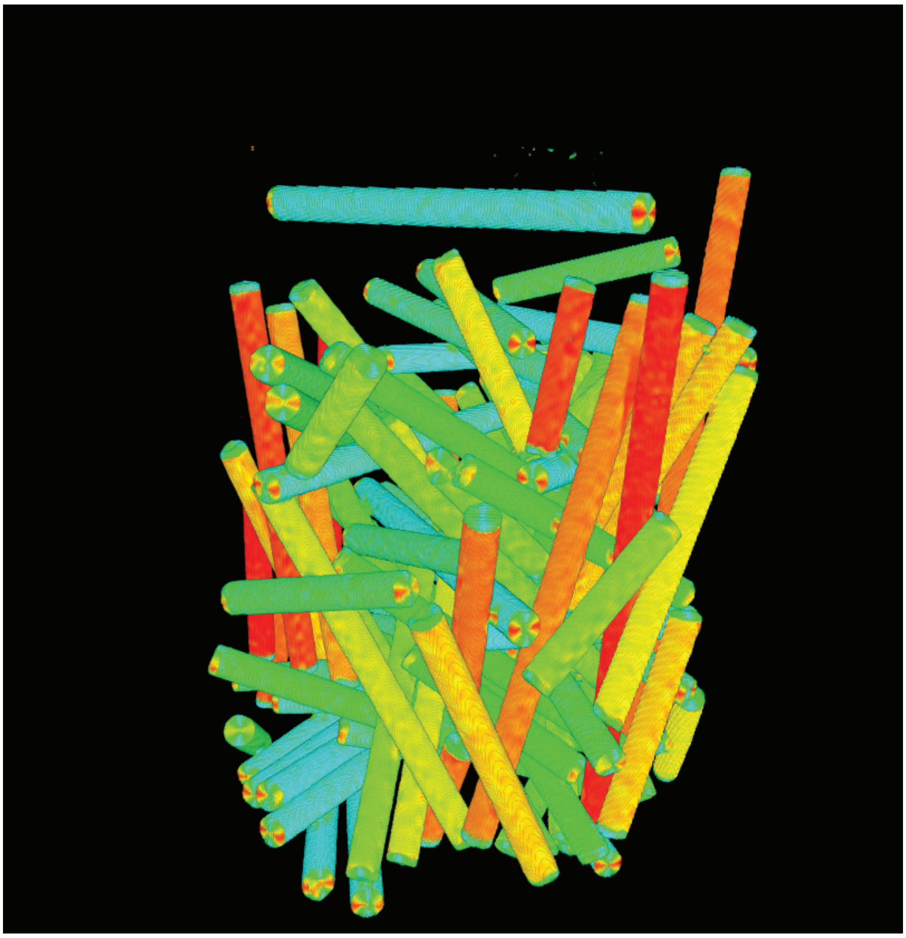

FIGURE 81 The visualization of color coded orientation of the sample in section 5.2.1.

commercial software packages are to provide this. However, when binary geometry is needed and the tools discussed at Chapters 4 and 5 can be used to obtain a high quality presentation. Artefacts, such as noise and edge blurring, cannot be avoided when using XμCT, and the effect has been studied more in details in [120]. The effect of edge blurring while thresholding a sample is visualized in figure 82 and compared to the numerically defined permeability value (Lattice-Boltzmann simulation) compared to experimentally obtained ([120]) is presented in figure 83. For the wool fibre web, the optimal threshold value would have been between 20 and 30. By visually examining the corresponding images, it was found that there was still noise left in flow channels at a threshold value 30. Permeability at the optimal threshold value would not have resulted using realistic sample geometry, combination of noise causing higher specific surface areas and thinner fibres increased the porosity of the geometry.

If untreated, the noise causes flow resistance to the flow channels and surface roughness. The effect of noise was tested here by simulations. Artificial sample geometries of hexagonal arrays of cylinders were prepared to test and demonstrate the effect of different imaging artefacts on structure and numerical fluid flow analysis. The volume size of the

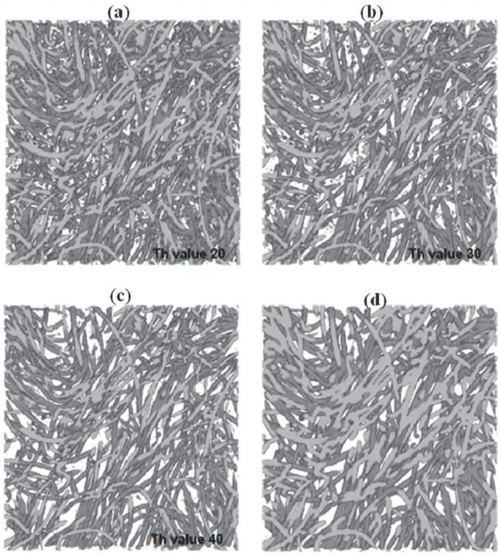

FIGURE 82 Visualization of a segmented wool fibre web sample at different threshold values: (a) 20, (b) 30 and (c) 40, and a manually processed reference segmentation (d).

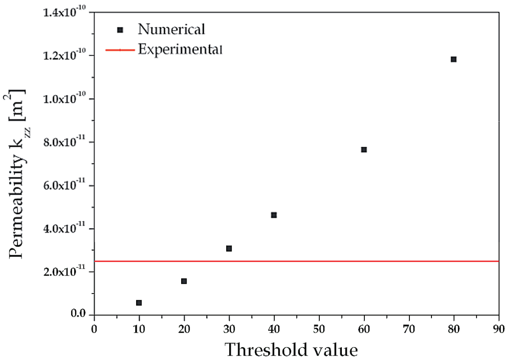

FIGURE 83 Numerically solved permeability coefficients for the wool fibre web as a function of the threshold value. Experimental results are given as an average of the five measurements for each sample type.

simulation geometries was 693 x 400 x 100 pixels and the porosity of the cylinder arrays 50 %. Visualisations of the flow field of four hexagonal arrays of cylinders having different levels of noise are shown in figure 84. Noise level is defined as a percentage of faulty voxels in the total volume of the sample.

The effect of noise on pore size distribution was evaluated as a function of noise level. Pore size distributions were determined using the local thickness transform. The pore size distribution was found to change dramatically as a function of noise level. The mode value of the distribution of the geometry with a noise level of 0.01% was approximately one third of the mode value for the noise free geometry.

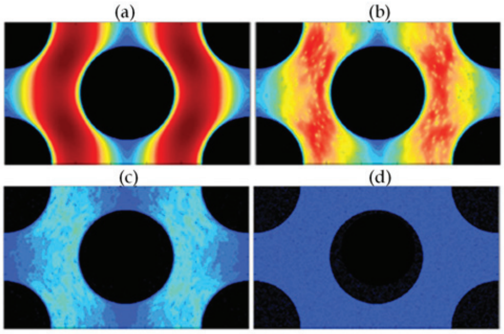

FIGURE 84 Visualisation of flow speed field of four hexagonal arrays of cylinders having different levels of noise: a) 0%, b) 0.05%, c) 0.3%, and d) 5%. Flow direction is in these cases from top to bottom. Red and yellow colours represent high flow speed and green and blue low flow speed.

6.6 Conclusions

In this chapter, we have listed various general purpose image analysis methods. Because these methods are all quite unambiguous in practice, we did not perform any tests or experimentally compare any of the methods. The reliability of the results depend on the steps taken to get those results (i.e., optimal imaging, proper denoising and segmentation).

If we are interested in the properties of some structural components of the materials at hand, we have two options for analysis:

- The structural components are individually labelled, and each component or its interaction is analysed.
- If it is not possible to separate individual components, the best means are used to analysed as a whole to obtain information regarding these individual components.

The common themes of the analysis are region-based analysis (statistical information about the regions of the image), connectivity analysis (how the parts of interest are connected to each others), distance measurements (finding routes through the materials), and simulations (using image geometry to computationally model some-real world phenomena).

The one thing not covered in this work is the representation of the data. Data can be represented visually in many different ways. Traditional charts can be used, and region-related properties, such as volume, connectivity, and number of holes, can be color-coded into the material and visualized using tools like those presented in section 2.8.

7 CONCLUSION

This paper has presented the entire process of XμCT imaging, starting from the image acquisition and ending with the results of the structural analyses. The final part of the continuum, understanding the results, has not been presented, as this aspect of the process is almost solely dependent on each individual case. Tomography has long been used as a medical examination tool for taking images of various body parts. The XμCT devices started the era of tomographic material research, which, in many cases, requires a different set of tools: this is where computer-aided image processing comes in. While the human visual system is highly adaptive, it is also easily distracted, and thus it is not able to perform accurate statistical analysis of images or gray values (see figure 85). The fact that XμCT images are large and require a great deal of effort to analyse also make the use of computers favourable for analysis of these images. However, the benefit of the human eye is that it tolerates noise and artefacts and is very good at finding shapes in images. Most computational methods of analysis perform poorly when working with noisy environments, and their ability to adapt to shapes is also limited. This is why most research performed on image analysis focuses on denoising and segmentation. The primary purpose of those two phases is to convert the data to a simple enough form for the computer to analyse it.

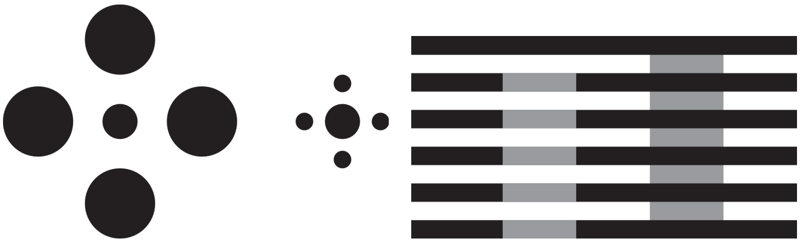

FIGURE 85 Left: Are the center dots the same size? Right: Are the gray bars the same color?

Chapter 2 presented the basics of the physical and technical background of XμCT imaging. That information is essential when trying to optimize the quality of the images, which is the key factor of success for image processing. X-ray behaviour, scanner functionality, and sample preparation are essential components of the imaging process.

Spending more time on imaging can help save time on solving the potential problems caused by poor image quality. Some problems cannot be solved using computational methods. By knowing the capabilities and limitations of the device, one also knows what can be expected from the device and from the images. If there is a problem with the image, the researcher should know whether or not there is a way to solve the problem using the hardware available to them.

Image processing can also solve many problems that occur during imaging that cannot be avoided. Noise, for example, often cannot be fully removed from images; if left unaddressed, this issue can render the analysis process useless, as it causes gray values that should be similar to become different. Many denoising methods have been developed to help reduce image noise. However, there seems to be a lack of understanding regarding how a denoising method should be selected and how they perform as a part of the imaging continuum. In this work, we wanted to compare the denoising methods in the context of XμCT to see if the selection of the method makes any difference. Chapter 4 compared the denoising methods according to their denoising quality, computational complexity, and usability. We were able to rank those methods according to the properties we consider important in denoising. Each method clearly has its advantages — some are best for restoring the original shape of the sample, some are faster than others, and some are more simple to use. The choice is often made between denoising quality and processing time. Computers are still limited in terms of XμCT image processing ability, and choosing the right algorithm can save a significant amount of processing time. Denoising quality is not the first priority for all applications.

Noise removal, however, is not the only benefit of using this algorithm. The benefit of choosing the ideal denoising method also occurs in later aspects of the image processing continuum. This can be seen in Chapter 5, where the denoising is combined with segmentation. Simple methods allow for the labelling of images with decent accuracy; however, when image quality decreases, simple methods are no longer efficient. Similarly, methods that perform well in pure-noise removal are also not ideal. Some denoising methods are able to reduce certain XμCT artefacts (like edge blurring and shadows), which is highly beneficial when segmenting the sample. Those methods produce more robust segmentation results and reduced the risks of segmentation errors. To this end, we can conclude that the selection of the denoising method does have an effect the ease with which segmentation is completed. Still, if no complicated segmentation or analysis of details close to the spatial resolution, is required, a simpler denoising method can also be sufficient.

The end of the XμCT image processing continuum marks the end of the image analysis. When considered as separate from the continuum, the image analysis if often very mechanical part, where there are not many uncertainty factors; the volume, orientation, or shape (etc.) of an object does not change when using different methods, only the implementation of the method can make difference to the usage.However, the selections made in earlier stages of the continuum may have some effect on the image analysis. For example, the resolution of the imaging system affects the size of the details that can be seen in the image, and the selection of the denoising and segmentation methods affects on how well the details of the image are preserved during the image processing. In some cases, the imaging parameters, denoising method and segmentation can affect what can be analysed in the image. If no contrast or edge is found between two material phases, it is impossible to separate those phases for the analysis.

Thus, when considering the efficiency and accuracy of the whole XμCT image processing continuum, one can reverse the continuum, starting with the analysis, and use that information to determine the requirements for the algorithms from the previous parts of the continuum. The significance of each part of the continuum can also be considered in terms of the whole process:

1. Image acquisition: During this stage we can make selections that can make the image processing either easy, doable, or impossible. At this point in the process, the selections have a very large impact on the entire process.

2. Image processing: The selection of the denoising method affects how easy or difficult segmentation will be. The chosen denoising method also affects on the quality of the analysis results. The choice of segmentation method affects what kind of analysis can be performed.

3. Image analysis: Using the correct analysis method makes the interpretation of the results easier.

In conclusion, the entire image processing continuum should be considered before individual methods for each step are selected. The selections made at the beginning of the continuum have a great impact on the steps that occur later in the process. The selections should be made according to what need to be done to avoid excess work. For example, the ability of a denoising method to remove all noise is not always necessary; often, a simpler and faster method can be used instead. However, for analysis where sharp edges are required, the selection of the noise removal method has to be considered.

In the end, the usability of the algorithm for the specific task at hand is what is most important. The easiest solution will be the one that is most appealing to the end user. If the parameters are difficult to define, and if results depend heavily on correctly defining those parameters, the user may choose to use a simpler (but less effective) algorithm, or they may try unsuccessfully to use a more complicated algorithm. It should also be noted that all algorithms have their limitations. Even the best algorithm cannot generate any more detail than is allowed by the resolution of the optical resolution of an image (though there are some exceptions; see [179]). If the quality of the image is low, the error limit of the analyses will be higher, and this reduces the reliability of the conclusions drawn from these analyses.

7.1 Future work

One of the major limitations on this research is the lack of a good open source multi threaded 3D image processing toolkit that takes into account the memory consumption and use efficient algorithms and is able to run processes in batches. A few 3D image processing toolboxes exist, including::

- Insight Toolkit. This toolkit has expanded, and it now includes more than just XμCT image processing. For some researchers, this toolkit may seem complicated and difficult to use.

- DipImage (DipLip). This toolkit is limited to use with MATLAB, and thus, it has some issues with memory and efficiency.

Many smaller tools also exist, but the lack of maintenance to these programs causes problems, such as poor documentation. Thus, there is currently a need for the development of an open-source library. Such a publicly accessible library would be beneficial for many researchers.

There are also more tools and research needed for the development of structural segmentation. Many of the problems faced during segmentation pertain to the shape-related properties of structures to be separated; many of these issues have not yet been researched very extensively. Analysis methods that do not depend on structure separation are also of interest to many researchers, as these methods can be used for more general purposes and thus can be used to solve may different problems. Scale-space and local-shape methods could be particularly useful for the study of many different materials.

In the present study, we examined the denoising methods to be used alone. To obtain better results, a combination of two methods should be studied. In practice DCT has been efficient for pure denoising and MS works well on edge restoration. A combination of these two methods, or perhaps some other similar methods, could provide better results for overall image processing.

Many of the methods presented by this paper are traditional, well-established methods. They have remained popular because they are simple and efficient. In future research, it would be interesting to explore whether more sophisticated methods, such as machine learning, graph theory, data mining, and modern simulation methods (like SPH) are able to glean more information from the images. The computers are constantly evolving allowing usage of computationally more demanding algorithms some day.

YHTEENVETO (FINNISH SUMMARY)

Otsikko: Huokoisten heterogeenisten materiaalien tutkiminen mikrotomografiakuvista.

Tässä työssä tutkitaan mikrotomografiakuvantamisketjun vaikutusta kuva-analyysin tulosten luotettavuuteen ja prosessin sujuvuuteen. Mielestämme ketjun alkupään toimenpiteet ovat oleellisimmat, ja vaikuttavat oleellisesti koko kuvantamisketjun laatuun. Työssä tutkitaan erityisesti kohinanpoistomenetelmien vaikutusta, ei pelkästään menetelmien kohinanpoistokykyä ajatellen, vaan myös ottaen huomioon koko kuvantamisketjun; sopivalla kohinanpoistomenetelmällä voidaan helpottaa työtä ketjun myöhemmissä vaiheissa. Lisäksi työn lopussa esitellään yleisimmin mikrotomografiassa käytettyjä segmentointi- ja kuva-analyysimenetelmiä.

REFERENCES

[1] N. Ahmed, T. Natarajan, and K. R. Rao. Discrete cosine transform. *IEEE Transactions on Computers*, C-23(1):90–93, January 1974.

[2] R. Al-Raoush and K. A. Alshibli. Distribution of local void ratio in porous media systems from 3D x-ray microtomography images. *Physica A: Statistical Mechanics and its Applications*, 361(2):441–456, 2006.

[3] R. Al-Raoush and A. Papadopoulos. Representative elementary volume analysis of porous media using x-ray computed tomography. *Powder Technology*, 200(1–2):69–77, 2010.

[4] A. Alfiansyah, K. H. Ng, and Lamsudin. R. Bone segmentation based on local structure descriptor driven active contour. *13th International Conference on Biomedical Engineering*, pages 1077–1081, 2009.

[5] R. Ali, C. Gunduz-Demir, T. Szilagyi, B. Durkee, and E.E. Graves. Semi-automatic segmentation of subcutaneous tumours from micro-computed tomography images. *Phys. Med. Biol.*, 58(22):8007–8019, Oct 2013.

[6] E. M. A. Anas, S. Y. Lee, and K. Hasan. Removal of ring artifacts in x-ray micro tomography using polyphase decomposition and spline interpolation. *International Conference on Electrical & Computer Engineering (ICECE 2010)*, Dec 2010.

[7] M. Andrzejczuk, T. Płocinski, W. Zielinski, and K. J. Kurzydłowski. Tem characterization of the artefacts induced by fib in austenitic stainless steel. *J Microsc*, 237(3):439–442, Mar 2010.

[8] E. Arias-Castro and D. L. Donoho. Does median filtering truly preserve edges better than linear filtering? *The Annals of Statistics*, 37(3):1172–1206, Jun 2009.

[9] M. Aronsson. On 3D fibre measurements of digitized paper from microscopy to fibre network, doctoral thesis, 2002.

[10] M. Axelsson. 3D tracking of cellulose fibres in volume images. In *Image Processing, 2007. ICIP 2007. IEEE International Conference on*, volume 4, pages 309–312, oct 2007.

[11] M. Axelsson. Estimating 3D fibre orientation in volume images. In *Pattern Recognition, 2008. ICPR 2008. 19th International Conference on*, pages 1–4, December 2008.

[12] M. Axelsson. *Image Analysis for Volumetric Characterisation of Microstructure*. PhD thesis, University of Uppsala, 2009.

[13] M. Axelsson and S. Svensson. 3D pore structure characterisation of paper. *Pattern Analysis and Applications*, 13:159–172, 2010.

[14] M. Axelsson, S. Svensson, and G. Borgefors. Reduction of ring artifacts in high resolution x-ray microtomography images. In *Proceedings of* 28^{th} *DAGM Symposium*, 2006.

[15] M. R. Ay, A. Ahmadian, H. Ghadiri, A. Maleki, P. Ghafarian, and H. Zaidi. The influence of x-ray spectra filtration on image quality and patient dose in the ge vct 64-slice cardiac CT scanner. In *Bioinformatics and Biomedical Engineering , 2009. ICBBE 2009.* 3^{rd} *International Conference on*, pages 1–4, 2009.

[16] S. Äyrämö. *Knowledge mining using robust clustering*. PhD thesis, University of Jyväskylä, 2006.

[17] L. Babout, W. Ludwig, E. Maire, and J.Y. Buffiere. Damage assessment in metallic structural materials using high resolution synchrotron x-ray tomography. *Nuclear Instruments and Methods in Physics Research B*, pages 303–307, 2003.

[18] E Bae, J. Shi, and X. Tai. Graph cuts for curvature based image denoising. *IEEE Transactions on Image Processing*, 20(5):1199–1210, May 2011.

[19] J. F. Barrett and N. Keat. Artefacts in CT: Recognition and avoidance. *Radiographics*, 2003.

[20] H. G. Barrow, J. M. Tenenbaum, R. C. Bolles, and H. C. Wolf. Parametric correspondence and chamfer matching: Two new techniques for image matching. In *Proceedings of the 5th International Joint Conference on Artificial Intelligence - Volume 2*, IJCAI'77, pages 659–663, San Francisco, CA, USA, 1977. Morgan Kaufmann Publishers Inc.

[21] K. J. Batenburg and J. Sijbers. Adaptive thresholding of tomograms by projection distance minimization. *Pattern Recognition*, 42(10):2297–2305, 2009. Selected papers from the 14th {IAPR} International Conference on Discrete Geometry for Computer Imagery 2008.

[22] K. Bavendiek, U. Ewer, A. Riedo, U. Heike, and U. Zscherpel. New measurement methods of focal spot size and shape of x-ray tubes in digital radiological applications in comparison to current standards. In •. 18th World Conference on Nondestructive Testing, April 2012.

[23] J. Bear. *Dynamics of Fluids in porous Media*. American Elsevier, 1972.

[24] R. Bedini, D. Meleo, R. Pecci, and L. Pacifici. The use of microtomography in bone tissue and biomaterial three-dimensional analysis. *Ann Ist Super Sanita*, 45(2):178–184, 2009.

[25] A. Bernasconi, F. Cosmi, and P. J. Hine. Analysis of fibre orientation distribution in short fibre reinforced polymers: A comparison between optical and tomographic methods. *Composites Science and Technology*, 72(16):2002–2008, Nov 2012.

[26] R. Berry and J. Burnell. *The Handbook of Astronomical Image Processing (Includes AIP4WIN Software) [Book with CD-ROM]*. Willmann-Bell, 2000.

[27] S. Beucher and F. Meyer. *Mathematical Morphology in Image Processing*, volume 34 of *Optical Engineering*, chapter The morphological approach to segmentation: the watershed transformation, page Mathematical Morphology in Image Processing. Marcel Dekker, Inc, 1993.

[28] I. U. Bhuiyan, J. Mouzon, F. Forsberg, S. P. E. Forsmo, M. Sjödahl, and J. Hedlund. Consideration of x-ray microtomography to quantitatively determine the size distribution of bubble cavities in iron ore pellets. *Powder Technology*, 233(0):312–318, 2013.

[29] J. Bigün and G. H. Granlund. Optimal orientation detection of linear symmetry. In *Proceedings of the IEEE First International Conference on Computer Vision*, pages 433–438, London, Great Britain, June 1987.

[30] G. G. Bilodeau. The weierstrass transform and Hermite polynomials. *Duke Mathematical Journal*, 29(2):293–308, Jun 1962.

[31] E. S. Boek and M. Venturoli. Lattice-boltzmann studies of fluid flow in porous media with realistic rock geometries. *Computers & Mathematics with Applications*, 59(7):2305–2314, 2010. Mesoscopic Methods in Engineering and Science.

[32] M. Boin and A. Haibel. Reduction of ring artefacts in high resolution micro-CT reconstructions. *Optics Express*, pages 12071–12075, 2006.

[33] G. Borgefors. Distance transformations in digital images. *Computer Vision, Graphics, and Image Processing*, 34(3):344–371, Jun 1986.

[34] Y. Boykov and G. Funka-Lea. Graph cuts and efficient n-d image segmentation. *International Journal of Computer Vision*, 70(2):109–131, November 2006.

[35] W. Boyle and G. Smith. Buried channel charge coupled devices, 1974.

[36] T. Brox and J. Weickert. Level set segmentation with multiple regions. *IEEE Transactions on Image Processing*, 15(10):3213–3218, Oct 2006.

[37] Bruker. Bruker microct www-page.

[38] A. Buades, B. Coll, and J. M. Morel. A review of image denoising algorithms, with a new one. *Multiscale Modeling & Simulation*, 2005.

[39] S. G. Bueno and A. Martinez-Albala. Contour detection by using radial searching for CT images. *Fuzziness and PDE based models for the segmentation of medical image*, 2004.

[40] H. Buie, G. Campbell, R. Klinck, J. Macneil, and S. Boyd. Automatic segmentation of cortical and trabecular compartments based on a dual threshold technique for in vivo micro-CT bone analysis. *Bone*, 41(4):505–515, October 2007.

[41] T. F. Chan and J. Shen. Variational image inpainting. *Comm. Pure Applied Math*, 58:579–619, 2005.

[42] T. F. Chan, J. Shen, and L. Vese. Variational pde models in image processing, 2002.

[43] G. Chinga-Carrasco, A. Miettinen, C. L. Luengo Hendriks, E. K. Gamstedt, and M. Kataja. Structural characterisation of kraft pulp fibres and their nanofibrillated materials for biodegradable composite applications. *Nanocomposites and Polymers with Analytical Methods*, Aug 2011.

[44] N. Chou, Wu. J., B. J. Bingren, A. Qiu, and K. Chuang. Robust automatic rodent brain extraction using 3-D pulse-coupled neural networks (PCnn). *IEEE Transactions on Image Processing*, 20(9):2554–2564, Sep 2011.

[45] D. Coeurjolly. Fast and accurate approximation of digital shape thickness distribution in arbitrary dimension. *Computer Vision and Image Understanding*, 116(12):1159–1167, Dec 2012.

[46] T. Coffey, S. G Urquhart, and H. Ade. Characterization of the effects of soft x-ray irradiation on polymers. *Journal of Electron Spectroscopy and Related Phenomena*, 122(1):65–78, 2002.

[47] D. Comaniciu and P. Meer. Mean shift: a robust approach toward feature space analysis. *IEEE Trans. Pattern Anal. Machine Intell.*, 24(5):603–619, May 2002.

[48] W. D. Coolidge. *Vacuum Tube*, 1916.

[49] A. M. Cormack. Representation of a function by its line integrals, with some radiological applications. *J. Appl. Phys.*, 34(2722), 1963.

[50] F. Cosmi, A. Bernasconi, and N. Sodini. Phase contrast micro-tomography and morphological analysis of a short carbon fibre reinforced polyamide. *Composites Science and Technology*, 71(1):23–30, Jan 2011.

[51] P-E. Danielsson. Euclidean distance mapping. *Computer Graphics and Image Processing*, 14(3):227–248, Nov 1980.

[52] R. Dass, Priyanka, and S. Devi. Image segmentation techniques. *International Journal of Electronics & Communication Technology*, 3(1), March 2012.

[53] A. A. de Moura Meneses, C. J. G. Pinheiro, R. Schirru, R. C. Barroso, D. Braz, and L. F. Oliveira. Artificial neural networks applied to bone recognition in x-ray computer microtomography imaging for histomorphometric analysis. *2008 IEEE Nuclear Science Symposium Conference Record*, Oct 2008.

[54] F. Debaste, A. Léonard, V. Halloin, and B. Haut. Microtomographic investigation of a yeast grain porous structure. *Journal of Food Engineering*, 97(4):526–532, 2010.

[55] M. Descoteaux, M. Audette, K. Chinzei, and K. Siddiqi. Bone enhancement filtering: application to sinus bone segmentation and simulation of pituitary surgery. *Comput Aided Surg*, 11(5):247–255, Sep 2006.

[56] S. Dietrich, J. M. Gebert, G. Stasiuk, A. Wanner, K. A. Weidenmann, O. Deutschmann, I. Tsukrov, and R. Piat. Microstructure characterization of cvi-densified carbon/carbon composites with various fiber distributions. *Composites Science and Technology*, 72(15):1892–1900, 2012.

[57] T. E. Dufresne, P. A. Chmielewski, M. D. Manhart, T. D. Johnson, and B. Borah. Risedronate preserves bone architecture in early postmenopausal women in 1 year as measured by three-dimensional microcomputed tomography. *Calcified Tissue International*, 73:423–432, October 2003.

[58] J. H. Dunsmuir, S. Bennett, L. Fareria, A. Mingino, and M. Sansone. X-ray microtomographic imaging and analysis for basic research. *Powder Diffraction*, 21:125–131, 6 2006.

[59] A. Ekman, A. Miettinen, T. Turpeinen, K. Backfolk, and J. Timonen. The number of contacts in random fibre networks. *Nordic Pulp and Paper Research Journal*, 27(2), 2012.

[60] M. Faessel and D. Jeulin. Segmentation of 3D microtomographic images of granular materials with the stochastic watershed. *Journal of Microscopy*, 239(1):17–31, Jul 2010.

[61] A. G. Farman and T. T. Farman. A comparison of 18 different x-ray detectors currently used in dentistry. *Oral Surg Oral Med Oral Pathol Oral Radiol Endod*, 99(4):485–489, Apr 2005.

[62] R. Farnoosh, Y. Gholamhossein, and Z. Behnam. Image segmentation using gaussian mixture models, 2008.

[63] E. Ferrié, J. Buffière, W. Ludwig, A. Gravouil, and L. Edwards. Fatigue crack propagation: In situ visualization using x-ray microtomography and 3D simulation using the extended finite element method. *Acta Materialia*, 54(4):1111–1122, 2006.

[64] A. Foi, V. Katkovnik, and K. Egiazarian. Pointwise shape-adaptive dct for high-quality deblocking of compressed color images. In *EUSIPCO 2006*, pages 1395–1411, 2006.

[65] Foley and Feiner. *Computer Graphics*. Addison-Wesley, 1996.

[66] J. Fonseca, P. Bésuelle, and G. Viggiani. Micromechanisms of inelastic deformation in sandstones: an insight using x-ray micro-tomography. *Géotechnique Letters*, 3(2):78–83, 2013.

[67] F. Forsberg and C. R. Siviour. 3d deformation and strain analysis in compacted sugar using x-ray microtomography and digital volume correlation. *Measurement Science and Technology*, 20(9), 2009.

[68] A. F. Frangi, W. J. Niessen, K. L. Vincken, and M. A. Viergever. Multiscale vessel enhancement filtering. In *Lecture Notes in Computer Science*, 1998.

[69] N. Friel and I. S. Molchanov. A new thresholding technique based on random sets. *Pattern Recognition*, 32(9):1507–1517, Sep 1999.

[70] M. Frigo and S. G. Johnson. The design and implementation of FFTw3. *Proceedings of the IEEE*, 93(2):216–231, Feb 2005.

[71] P. Frisullo, F. Licciardello, G. Muratore, and M. A. Del Nobile. Microstructural characterization of multiphase chocolate using x-ray microtomography. *Journal of Food Science*, 75(7):469–476, 2010.

[72] T. Fröba and J. P. Steffen. Assessing the effect of focal spot movement on the accuracy of CT results by using a simulation technique. *NDT.net Issue*, February 2011.

[73] J. Fu, X. Hu, A. Velroyen, M. Bech, M. Jiang, and F. Pfeiffer. 3D algebraic iterative reconstruction for cone-beam x-ray differential phase-contrast computed tomography. *PLOS ONE*, 10(3), Mar 2015.

[74] D. Garcia, C. L. Lin, and J. D. Miller. Quantitative analysis of grain boundary fracture in the breakage of single multiphase particles using x-ray microtomography procedures. *Minerals Engineering*, 22(3):236–243, 2009.

[75] B. Gartner. Fast and robust smallest enclosing balls. In *Proceedings of Seventh Annual European Symposium on Algorithms (ESA), Lecture notes in computer science*, volume 1643, pages 325–338, 1999.

[76] C. A. Glasbey. An analysis of histogram-based thresholding algorithms. *CVGIP: Graphical Models and Image Processing*, 55(6):532–537, 1993.

[77] A. Glassner. Fill 'er up! [graphics filling algorithms]. *Computer Graphics and Applications, IEEE*, 21(1):78–85, 2001.

[78] R. Glowinski, T. Kärkkäinen, Valkonen, T., and A. Ivannikov. Nonsmooth SOR for L^1-fitting: Convergence study and discussion of related issues. *Journal of Scientific Computing*, 37(2):103–138, 2008.

[79] R. Glowinski, T. Kärkkäinen, T. Valkonen, and A. Ivannikov. Non-smooth sor for l 1-Fitting: Convergence study and discussion of related issues. *Journal of Scientific Computing*, 37(2):103–138, Aug 2008.

[80] R. C. Gonzalez and R. E. Woods. *Digital Image Processing*. Addison-Wesley Longman Publishing Co., Inc., Boston, MA, USA, 2nd edition, 2001.

[81] R. Gordon, R. Bender, and G. T. Herman. Algebraic reconstruction techniques (art) for three-dimensional electron microscopy and x-ray photography. *Journal of Theoretical Biology*, 29(3):471–481, 1970.

[82] P. Gouze and L. Luquot. X-ray microtomography characterization of porosity, permeability and reactive surface changes during dissolution. *Journal of Contaminant Hydrology*, 120–121(0):45–55, 2011. Reactive Transport in the Subsurface: Mixing, Spreading and Reaction in Heterogeneous Media.

[83] L. Grodzins. Optimum energies for x-ray transmission tomography of small samples: Applications of synchrotron radiation to computerized tomography i. *Nuclear Instruments and Methods in Physics Research*, 206(3):541–545, 1983.

[84] Hamamatsu. Microfocus x-ray sources. http://www.hamamatsu.com/jp/en/3028.html.

[85] U. Hampel, A. Bieberle, D. Hoppe, E. Kronenberg, J.and Schleicher, T. Sühnel, F. Zimmermann, and C. Zippe. High resolution gamma ray tomography scanner for flow measurement and non-destructive testing applications. *Review of Scientific Instruments*, 78(10), 2007.

[86] J. Han. *Data Mining: Concepts and Techniques*. Morgan Kaufmann Publishers Inc., San Francisco, CA, USA, 2005.

[87] G. E. Healey and R. Kondepudy. Radiometric CCD camera calibration and noise estimation. *IEEE Transactions on Pattern Analysis and Machine Intelligence*, 16(3):267–276, Mar 1994.

[88] O. Hemberg, M. Otendal, and H. M. Hertz. Liquid-metal-jet anode electron-impact x-ray source. *Applied Physics Letters*, 83(7):1483–1485, 2003.

[89] T. Hildebrand, A. Laib, R. Müller, J. Dequeker, and P. Rüegsegger. Direct three-dimensional morphometric analysis of human cancellous bone: Microstructural data from spine, femur, iliac crest, and calcaneus. *Journal of Bone and Mineral Research*, 14(7):1167–1174, July 1999.

[90] T. Hildebrand and P. Rüegsegger. A new method for the model-independent assessment of thickness in three-dimensional images. *Journal of Microscopy*, 185(1):67–75, 1997.

[91] M. Hilts. X-ray computed tomography imaging of polymer gel dosimeters. *Journal of Physics, Conference Series 56*, 2006.

[92] D. C. Hoaglin, F. Mosteller, and J. W. Tukey, editors. *Understanding Robust and Exploratory Data Analysis (Wiley Series in Probability and Statistics)*. Wiley, 1982.

[93] A. Holmberg, J. Reinspach, M. Lindblom, E. Chubarova, M. Bertilson, O. von Hofsten, D. Nilsson, M. Selin, D. Larsson, P. Skoglund, U. Lundström, P. Takman, U. Vogt, and H. M. Hertz. Towards 10-nm soft x-ray zone plate fabrication. In *The 10th International Conference on X-ray Microscopy*, 2011.

[94] C. Holzner, M. Feser, S. Vogt, B. Hornberger, S. B. Baines, and C. Jacobsen. Zernike phase contrast in scanning microscopy with x-rays. *Nat Phys*, 6:883–887, 2010.

[95] L. Huang and M. J. Wang. Image thresholding by minimizing the measures of fuzziness. *Pattern Recognition*, 28(1):41–51, 1995.

[96] T. Huang, G. Yang, and G. Tang. A fast two-dimensional median filtering algorithm. *IEEE Transactions on Acoustics, Speech, and Signal Processing*, 27(1):13–18, Feb 1979.

[97] M. M. Hytros, I. M. Jureidini, J. Chun, R. C. Lanza, and N. Saka. High-energy x-ray computed tomography of the progression of the solidification front in pure aluminum. *Metallurgical and Materials Transactions A*, 30(5):1403–1409, 1999.

[98] J. Hyväluoma, M. Thapaliya, J. Alaraudanjoki, T. Siren, K. Mattila, J. Timonen, and E. Turtola. Using microtomography, image analysis and flow simulations to characterize soil surface seals. *Computers & Geosciences*, 48(0):93–101, 2012.

[99] J. Hyväluoma, T. Turpeinen, P. Raiskinmäki, A. Jäsberg, A. Koponen, M. Kataja, J. Timonen, and S. Ramaswamy. Intrusion of nonwetting liquid in paper. *Phys. Rev. E*, 75, Mar 2007.

[100] P. Iassonov, T. Gebrenegus, and M. Tuller. Segmentation of x-ray computed tomography images of porous materials: A crucial step for characterization and quantitative analysis of pore structures. *Water Resources Research*, 45(9), Sep 2009.

[101] ID19. Id19 - high-resolution diffraction topography beamline.

[102] Encyclopaedia Britannica Inc. scientific method.

[103] O. M. Jensen, P. Lura, and K. Kovler, editors. *Four-Dimensional X-ray Microtomography Study of Water Movement during Internal Curing*, Bagneux, France, 2006. RILEM Publications S.A.R.L.

[104] W. Jikun, C. Laigao, G. A. Sandison, L. Yun, and L.X. Xu. X-ray CT high-density artefact suppression in the presence of bones. *Physica in medicine & biology*, 2004.

[105] M. Joachimiak, D. Rusanovskyy, M. Hannuksela, and M. Gabbouj. Multiview 3d video denoising in sliding 3d dct domain. In *20th European Signal Processing Conference, EUSIPCO*, pages 1109–1113. European Signal Processing Conference (EUSIPCO), Institute of Electrical and Electronics Engineers IEEE, August 2012.

[106] T. Joffre, A. Miettinen, F. Berthold, and E. K. Gamstedt. X-ray micro-computed tomography investigation of fibre length degradation during the processing steps of short-fibre composites. *Composites Science and Technology*, 105:127–133, Dec 2014.

[107] W. Kabsch. A solution for the best rotation to relate two sets of vectors. *Acta Crystallogr Sect A Cryst Phys Diffr Theor Gen Crystallogr'*, 32(5):922–923, Sep 1976.

[108] A. C. Kak and M. Slaney. *Principles of Computerized Tomographic Imaging*. IEEE Press, New York, 1988.

[109] J. N. Kapur, P. K. Sahoo, and A. K. C. Wong. A new method for gray-level picture thresholding using the entropy of the histogram. *Computer Vision, Graphics, and Image Processing*, 29(3):273–285, 1985.

[110] T. Kärkkäinen, K. Kunisch, and K. Majava. Denoising of smooth images using L^1-fitting. *Computing*, 74(4):353–376, 2005.

[111] T. Kärkkäinen and K. Majava. Nonmonotone and monotone active-set methods for image restoration, part 1: Convergence analysis. *Journal of Optimization Theory and Applications*, 106:61–80, 2000.

[112] T. Kärkkäinen and K. Majava. Nonmonotone and monotone active-set methods for image restoration, part 2: Numerical results. *Journal of Optimization Theory and Applications*, 106:81–105, 2000.

[113] T. Kärkkäinen and K. Majava. Semi-adaptive, convex optimization methodology for image denoising. *IEE Proceedings - Vision, Image and Signal Processing*, 152(5):553–560, 2005.

[114] T. Kärkkäinen, K. Majava, and M. M. Mäkelä. Comparison of formulations and solution methods for image restoration problems. *Inverse Problems*, 17:1977–1995, 2001.

[115] M. Kass, A. Witkin, and D. Terzopoulos. Snakes: Active contour models. *International Journal of Computer Vision*, 1(4):321–331, Jan 1988.

[116] R. Keys. Cubic convolution interpolation for digital image processing. *Acoustics, Speech and Signal Processing, IEEE Transactions on*, 29(6):1153–1160, December 1981.

[117] M. Kiderlen and J. Ziegel. Estimation of the surface area of a three-dimensional set from digitizations. Presentation in 3rd Workshop on 3D Imaging, Analysis, Modeling and Simulation, April 2010.

[118] J. Kittler and J. Illingworth. Minimum error thresholding. *Pattern Recognition*, 19(1):41–47, 1986.

[119] V. Koivu, R. Seppänen, T. Turpeinen, K. Mattila, J. Hyväluoma, and M. Kataja. Combining x-ray micro-tomography and image analysis to study imbibition and void space in liquid packaging board. *J. Pulp Pap. Sci. 36(3-4)*, 2010.

[120] V. Koivu and T. Turpeinen. The effect of tomography imaging artefacts on structural analysis and numerical permeability simulations. *Computational Simulations and Applications*, Oct 2011.

[121] V. Koivu, T. Turpeinen, and M. Kataja. X-ray micro-tomographic study of papermaking fabrics. In *in Proceedings of Progress in Paper Physics Seminar 2008*, 2008.

[122] V. Koivu, T. Turpeinen, M. Myllys, and M. Kataja. Validation of lattice-boltzmann numerical simulations for fluid flow through compressed paper board samples. Technical report, VTT research notes 2048, 2008.

[123] T. Y. Kong and A. Rosenfeld. Digital topology: Introduction and survey. *Computer Vision, Graphics, and Image Processing*, 48(3):357–393, Dec 1989.

[124] C. Kottler, V. Revol, R. Kaufmann, C. Urban, K. Knop, U. Sennhauser, I. Jerjen, T. Lüthi, F. Cardot, P. Niedermann, J-P. Morel, C. Maake, H. Walt, E. Knop, and N. Blanc. Phase sensitive x-ray imaging: Towards its interdisciplinary applications. In P.K. Rastogi and E. Hack, editors, *Proceedings of Intercational Conference on Adcanced Phase Measurement Methdos in Optics and Imaging*, pages 213–218. American Institute of Physics, 2010.

[125] M. Krause, J. M. Hausherr, B. Burgeth, C. Herrmann, and W. Krenkel. Determination of the fibre orientation in composites using the structure tensor and local x-ray transform. *Journal of Materials Science*, 45:888–896, 2010.

[126] K. Krissian. Flux-based anisotropic diffusion applied to enhancement of 3-D angiogram. *IEEE Trans. Med. Imag. 11*, 2002.

[127] M. Krumm, K. Kasperl, and M. Franz. Reducing non-linear artifacts of multi-material objects in industrial 3D computed tomography. *NDT & E International*, 2008.

[128] A. J. Kubis, G. J. Shiflet, R. Hull, and D. N. Dunn. Focused ion-beam tomography. *Metallurgical and Materials Transactions A*, 35(7):1935–1943, 2004.

[129] J. Kuva, M. Siitari-Kauppi, A. Lindberg, I. Aaltonen, T. Turpeinen, M. Myllys, and J. Timonen. Microstructure, porosity and mineralogy around fractures in olkiluoto bedrock. *Engineering Geology*, 139-140:28–37, Jun 2012.

[130] T. Lahdemäki, M. Kelokaski, M. Siitari-Kauppi, M. Voutilainen, M. Myllys, T. Turpeinen, J. Timonen, F. Mateos, and M. Montoto. Characterizing low-permeable granitic rock from micrometer to centimeter scale: X-ray microcomputed tomography. In *Confocal Laser Scanning Microscopy and 14C-PMMA Method*. MRS Symp. Proc., 2007.

[131] M. Lak, G. Fleck, D. Azar, M. S. Engel, H. F. Kaddumi, D. Neraudeau, P. Tafforeau, and A. Nel. Phase contrast x-ray synchrotron microtomography and the oldest damselflies in amber (odonata: Zygoptera: Hemiphlebiidae). *Zoological Journal of the Linnean Society*, 156:913–923, 2009.

[132] G. Landrot, J. B. Ajo-Franklin, L. Yang, S. Cabrini, and C. I. Steefel. Measurement of accessible reactive surface area in a sandstone, with application to CO2 mineralization. *Chemical Geology*, 318-319:113–125, Jul 2012.

[133] T. Lehmann, A. Sovakar, W. Schmiti, and R. Repges. A comparison of similarity measures for digital subtraction radiography. *Computers in Biology and Medicine*, 27(2):151–167, 1997.

[134] F. Lekien and J. Marsden. Tricubic interpolation in three dimensions. *Journal of Numerical Methods and Engineering*, 63:455–471, 2005.

[135] M. Levoy. Area flooding algorithms. Hanna-Barbera Productions, June 1981.

[136] C. H. Li and C. K. Lee. Minimum cross entropy thresholding. *Pattern Recognition*, 26(4):617–625, 1993.

[137] N. Limodin, J. Réthoré, J. Buffière, A. Gravouil, F. Hild, and S. Roux. Crack closure and stress intensity factor measurements in nodular graphite cast iron using three-dimensional correlation of laboratory x-ray microtomography images. *Acta Materialia*, 57(14):4090–4101, 2009.

[138] N. Limodin, L. Salvo, E. Boller, M. Suery, M. Felberbaum, S. Gailliegue, and K. Madi. In situ and real-time 3-D microtomography investigation of dendritic solidification in an Al-10wt.% cu alloy. *Acta Materialia*, 57:2300–2310, 2009.

[139] C. L. Lin, A. R. Videla, and J. D. Miller. Advanced three-dimensional multiphase flow simulation in porous media reconstructed from x-ray microtomography using the he-chen-zhang lattice boltzmann model. *Flow Measurement and Instrumentation*, 21(3):255–261, 2010. Special Issue: Validation and Data Fusion for Process Tomographic Flow Measurements.

[140] J. Lindblad. Surface area estimation of digitized 3D objects using weighted local configurations. *Image and Vision Computing*, 2005.

[141] T. Lindeberg. Edge detection and ridge detection with automatic scale selection. Technical report, Department of Numerical Analysis and Computing Science, Royal Institute of Technology, S-100 44 Stockholm, Sweden, 1996.

[142] W. B. Lindquist, S. Lee, D. A. Coker, K. W. Jones, and P. Spanne. Medial axis analysis of void structure in three-dimensional tomographic images of porous media. *Journal of Geophysical Research*, 101(B4), 1996.

[143] J. J. Liu, S. R. Watt-Smith, and S. M. Smith. CT reconstruction using fbp with sinusoidal amendment for metal artefact reduction. In *Proc. VIIth Digital Image Computing: Techniques and Applications*, 2004.

[144] Y. Liu, J. Yi, H. Zhang, Q. Zheng, and J. Paul. Surface area estimation of digitized 3D objects using quasi-Monte Carlo methods. *Pattern Recogn.*, 43(11):3900–3909, November 2010.

[145] W. E. Lorensen and H. E. Cline. Marching cubes: A high resolution 3D surface construction algorithm. *SIGGRAPH Comput. Graph. 21*, 1987.

[146] S. Lublinsky, E. Ozcivici, and S. Judex. An automated algorithm to detect the trabecular-cortical bone interface in micro-computed tomographic images. *Calcified Tissue International*, 81:285–293, 2007.

[147] O. Ludwig, M. Dimichiel, L. Salvo, M. Suéry, and P. Falus. In-situ three-dimensional microstructural investigation of solidification of an al-cu alloy by ultrafast x-ray microtomography. *Metallurgical and Materials Transactions A*, 36(6):1515–1523, 2005.

[148] C. L. Luengo Hendriks. Constrained and dimensionality-independent path openings. *IEEE Transactions on Image Processing*, 19(6):1587–1595, Jun 2010.

[149] A. Lukin. Tips & tricks: Fast image filtering algorithms. In *GraphiCon'2007 Russia,*, 2007.

[150] J. Lux, C. Delisée, and X. Thibault. 3D characterication of wood based fibrous materials: an application. *Image Analysis & Stereology*, 25(1), 2011.

[151] H. Ma, T. Turpeinen, S. Silvennoinen, M. Torvinen, R. Rinnankoski-Tuikka, H. Kainulainen, J. Timonen, Rahkila Kujala, U., P., and H Suominen. Effects of diet-induced obesity and voluntary wheel running on the microstructure of the murine distal femur. *Nutrition and Metabolism*, 2011.

[152] M. Maggioni, V. Katkovnik, K. Egiazarian, and A. Foi. Nonlocal transform-domain filter for volumetric data denoising and reconstruction. *IEEE Trans. on Image Process.*, 22(1):119–133, Jan 2013.

[153] E. Maire, O. Bouaziz, M. Di Michiel, and C. Verdu. Initiation and growth of damage in a dual-phase steel observed by x-ray microtomography. *Acta Materialia*, 56(18):4954–4964, 2008.

[154] J. V. Manjón, P. Coupé, A. Buades, D. L. Collins, and R. Montserrat. New methods for MRI denoising based on sparseness and self-similarity. *Medical Image Analysis*, 16(1):18–27, Jan 2012.

[155] K. V. Mardia and T. J. Hainsworth. A spatial thresholding method for image segmentation. *IEEE Trans. Pattern Anal. Mach. Intell.*, 10(6):919–927, November 1988.

[156] J. Martín-Herrero and Ch. Germain. Microstructure reconstruction of fibrous c/c composites from x-ray microtomography. *Carbon*, 45(6):1242–1253, 2007.

[157] M. Matrecano, M. Poderico, G. Poggi, M. Romano, and M. Cesarelli. *Application of denoising techniques to micro-tomographic images*, pages 1–4. Institute of Electrical and Electronics Engineers, Nov 2010.

[158] S. A. McDonald, N. Ravirala, P. J. Withers, and A. Alderson. In situ three-dimensional x-ray microtomography of an auxetic foam under tension. *Scripta Materialia*, 60(4):232–235, 2009.

[159] E. Meijering. A chronology of interpolation: From ancient astronomy to modern signal and image processing. In *Proceedings of the IEEE*, pages 319–342, 2002.

[160] M. Meyer, M. Desbrun, P. Schröder, and A. H. Barr. Discrete differential-geometry operators for triangulated 2-manifolds. *Visualization and Mathematics III*, pages 35–57, 2003.

[161] Microsoft. *Coordinate Systems (Direct3D 10)*. Microsoft, http://msdn.microsoft.com/en-us/library/windows/desktop/cc3080492.3 edition.

[162] P. A. Midgley and M. Weyland. 3D electron microscopy in the physical sciences: the development of z-contrast and {EFTEM} tomography. *Ultramicroscopy*, 96(3–4):413–431, 2003. Proceedings of the International Workshop on Strategies and Advances in Atomic Level Spectroscopy and Analysis.

[163] A. Miettinen, C. L. Luengo Hendriks, G. Chinga-Carrasco, E. K. Gamstedt, and M. Kataja. A non-destructive x-ray microtomography approach for measuring fibre length in short-fibre composites. *Composites Science and Technology*, 72(15):1901–1908, Oct 2012.

[164] L. Miettinen, P. Kekäläinen, T. Turpeinen, J. Hyväluoma, J. Merikoski, and J. Timonen. Dependence of thermal conductivity on structural parameters in porous samples. *AIP Advances*, 2(1):012101, 2012.

[165] K. Mikolajczyk and C. Schmid. A performance evaluation of local descriptors. *IEEE Transactions on Pattern Analysis and Machine Intelligence*, 27(10):1615–1630, 2002.

[166] A. C. Moreira, C. R. Appoloni, Iara F. Mantovani, J. S. Fernandes, L. C. Marques, R. Nagata, and C. P. Fernandes. Effects of manual threshold setting on image analysis results of a sandstone sample structural characterization by x-ray microtomography. *Applied Radiation and Isotopes*, 70(6):937–941, 2012.

[167] R. Moreno-Atanasio, R. A. Williams, and X. Jia. Combining x-ray microtomography with computer simulation for analysis of granular and porous materials. *Particuology*, 8(2):81–99, 2010.

[168] M. Myllykoski, R. Glowinski, T. Kärkkäinen, and T. Rossi. A new augmented Lagrangian approach for the L^1-mean curvature image denoising. *SIAM Journal on Imaging Sciences*, 8(1):95–125, 2015.

[169] F. Natterer. *The Mathematics of Computerized Tomography*. Wiley, 1986.

[170] M. S. Naumann, W. Niggl, C. Laforsch, C. Glaser, and C. Wild. Coral surface area quantification-evaluation of established techniques by comparison with computer tomography. *Coral Reefs*, 28(1):109–117, Jan 2009.

[171] W. W. Nicholas. Efficiency of production of x rays. *BUR. STAN. J. RES.*, 5(4):843, Oct 1930.

[172] J. Nielsen. *Usability Engineering*. Morgan Kaufmann Publishers Inc., San Francisco, CA, USA, 1993.

[173] L. P. Nogueira, D. Braz, and R. C. Barroso. Dependence of threshold variations on the assessment of histomorphometric indices from computed microtomography using synchrotron radiation. *Micron*, 43(6):739–745, 2012.

[174] L. P. Nogueira, D. Braz, R. C. Barroso, L. F. Oliveira, C. J. G. Pinheiro, D. Dreossi, and G. Tromba. 3D histomorphometric quantification of trabecular bones by computed microtomography using synchrotron radiation. *Micron*, 41(8):990–996, December 2010.

[175] L. Olmos, C. L. Martin, D. Bouvard, D. Bellet, and M. Di Michiel. Investigation of the sintering of heterogeneous powder systems by synchrotron microtomography and discrete element simulation. *Journal of the American Ceramic Society*, 92(7):1492–1499, 2009.

[176] Oracle. The java tutorials, 2013.

[177] N. Otsu. A threshold selection method from gray-level histograms. *IEEE Transactions on Systems, Man and Cybernetics*, 9(1):62–66, January 1979.

[178] N. Pan. *Design & Nature II*, chapter On uniqueness of fibrous materials, pages 493–502. WIT press, 2004.

[179] S. C. Park, M. K. Park, and M. G. Kang. Super-resolution image reconstruction: a technical overview. *IEEE Signal Processing Magazine*, 20(3):21–36, May 2003.

[180] K. Pearson. Contributions to the mathematical theory of evolution. *Philosophical Transactions of the Royal Society A: Mathematical, Physical and Engineering Sciences*, 185(0):71–110, Jan 1894.

[181] G. P. Penney, J. Weese, J. A. Little, P. Desmedt, D. L. G. Hill, and D. J. Hawkes. A comparison of similarity measures for use in 2D-3D medical image registration. *Medical Image Computing and Computer-Assisted Interventation — MICCAI'98*, pages 1153–1161, 1998.

[182] P. Perona and J. Malik. Scale-space and edge detection using anisotropic diffusion. In *Proceedings of IEEE Computer Society Workshop on Computer Vision*, 1987.

[183] Z. Peter, V. Bousson, C. Bergot, and F. Peyrin. A constrained region growing approach based on watershed for the segmentation of low contrast structures in bone micro-CT images. *Pattern Recognition*, 41(7):2358–2368, 2008.

[184] F. Peyrin, Z. Peter, A. Larrue, A. Bonnassie, and D. Attali. Local geometrical analysis of 3D porous networks based on the medial axis: Application to bone microarchitechture microtomography images. *Image Anal Stereol*, 26(3):179–185, Nov 2007.

[185] F. Pfeiffer, T. Weitkamp, O. Bunk, and C. David. Phase retrieval and differential phase-contrast imaging with low-brilliance x-ray sources. *Nature Physics*, 2(4):258–261, Mar 2006.

[186] J. R. Price, D. Aykac, and J. Wall. A 3D level sets method for segmenting the mouse spleen and follicles in volumetric microct images. *2006 International Conference of the IEEE Engineering in Medicine and Biology Society*, Aug 2006.

[187] M. A. B. Promentilla, T. Sugiyama, T. Hitomi, and N. Takeda. Quantification of tortuosity in hardened cement pastes using synchrotron-based x-ray computed microtomography. *Cement and Concrete Research*, 39(6):548–557, 2009.

[188] E. Quan. *Imaging Properties of a Rotation-Free, Arrayed-Source Micro-Computed Tomography System.* PhD thesis, North Carolina State University, 2009.

[189] J. Radon. Uber die bestimmung von funktionen durch ihre integralwerte langs gewisser mannigfaltigkeiten. *Berichte SÄber die Verhandlungen der Sächsische Akademie der Wissenschaften*, 1917.

[190] G. N. Ramanchandran and A. V. Lakshminarayanan. Three dimensional reconstruc-tions from radiographs and electron micrographs: Application of convolution instead of fourier transforms. In *Proceedings of the National Academy of Sciences*, 1971.

[191] N. Ramesh. Thresholding based on histogram approximation. *IEE Proceedings - Vision, Image, and Signal Processing*, 142(5):271, 1995.

[192] P. Rüegsegger, B. Koller, and R. Müller. A microtomographic system for the nondestructive evaluation of bone architecture. *Calcified Tissue International*, 58:24–29, 1996.

[193] T. W. Ridler and S. Calvard. Picture thresholding using an iterative selection method. *Systems, Man and Cybernetics, IEEE Transactions on*, 8(8):630–632, August 1978.

[194] G. Rizzo, D. Tresoldi, E. Scalco, M. Mendez, A. M. Bianchi, G. L. Moro, and A. Rubinacci. Automatic segmentation of cortical and trabecular components of bone specimens acquired by pqct. In *Engineering in Medicine and Biology Society, 2008. EMBS 2008. 30th Annual International Conference of the IEEE*, pages 486–489, August 2008.

[195] C. Robertson and S. C. George. Theory and practical recommendations for autocorrelation-based image correlation spectroscopy. *J Biomed Opt*, 8(17), 2012.

[196] S Rolland du Roscoat, J-F Bloch, and X. Thibault. Synchrotron radiation microtomography applied to investigation of paper. *Journal of Physics D: Applied Physics*, 38(10A):A78, 2005.

[197] W. K. Röntgen. On a new kind of rays. *Nature*, 53:274–276, 1896.

[198] A. Rosenfeld and P. De La Torre. Histogram concavity analysis as an aid in threshold selection. *IEEE Transactions on Systems, Man, and Cybernetics*, SMC-13(2):231–235, 2012.

[199] L. I. Rudin, S. Osher, and E. Fatemi. Nonlinear total variation based noise removal algorithms. *Physica D: Nonlinear Phenomena*, 60(1-4):259–268, Nov 1992.

[200] P. Ruëgsegger, B. Koller, and R. Müller. A microtomographic system for the non-destructive evaluation of bone architecture. *Calcif Tissue Int*, 1(58):24–29, 1996.

[201] D. Rusanovskyy and K. Egiazarian. Video denoising algorithm in sliding 3d dct domain. In Jacques Blanc-Talon, Wilfried Philips, Dan Popescu, and Paul Scheunders, editors, *Advanced Concepts for Intelligent Vision Systems*, volume 3708 of *Lecture Notes in Computer Science*, pages 618–625. Springer Berlin Heidelberg, 2005.

[202] J. C. Russ. *The Image Processing Handbook (Image Processing Handbook*. CRC Press, Inc., 2006.

[203] M. Saarela and T. Kärkkäinen. Analyzing student performance using sparse data of core bachelor courses. *Journal of Educational Data Mining*, 7(1):3–32, 2015.

[204] B. Sankur and M. Sezgin. Survey over image thresholding techniques and quantitative performance evaluation. *Journal of Electronic Imaging*, 13(1), Jan 2004.

[205] A. Sasov, X. Liu, and P. Salmon. Compensation of mechanical inaccuracies in micro-CT and nano-CT. In *Proc of Spie*, volume 7078, 2008.

[206] A. Sasov and D. Van Dyck. Desktop x-ray microscopy and microtomography. *Journal of Microscopy*, 191:151–158, August 1997.

[207] T. Sato, O. Ikeda, Y. Yamakoshi, and M. Tsubouchi. X-ray tomography for microstructural objects. *Appl. Opt.*, 20(22):3880–3883, November 1981.

[208] K. Schladitz. Quantitative micro-CT. *Journal of Microscopy*, 243(2):111–117, 2011.

[209] C. A. Schneider, W. S. Rasband, and K. W. Eliceiri. Nih image to imagej: 25 years of image analysis. *Nature Methods*, 9:671–675, 2012.

[210] R. Schulze, U. Heil, D. Gross, D. D. Bruellmann, E. Dranischnikow, U. Schwanecke, and E. Schoemer. Artefacts in cbct: a review. *Dentomaxillofacial Radiology*, 40(5):265–273, Jul 2011.

[211] A. E. Scott, M. Mavrogordato, P. Wright, I. Sinclair, and S. M. Spearing. In situ fibre fracture measurement in carbon-epoxy laminates using high resolution computed tomography. *Composites Science and Technology*, 71(12):1471–1477, 2011.

[212] J. A. Sethian. A fast marching level set method for monotonically advancing fronts. In *Proc. Nat. Acad. Sci*, pages 1591–1595, 1995.

[213] A. Setiawan, T. Suekane, Y. Deguchi, and K. Kusano. Three-dimensional imaging of pore-scale water flooding phenomena in water-wet and oil-wet porous media. *Journal of Flow Control, Measurement & Visualization*, 02(02):25–31, 2014.

[214] B. Shackel. *Usability - context, framework, definition, design and evaluation*. Human factors for informatics usability. Cambridge University Press, 2001.

[215] V. Shatokha, I. Korobeynikov, and E. Maire. On the application of 3D x-ray microtomography for studies in the field of iron ore sintering technology. *Sintering - Methods and Products*, Mar 2012.

[216] J. Shena, W. Shenb, S. Castanc, and T. Zhang. Sum-box technique for fast linear filtering. *Signal Processing*, 2002.

[217] M. Siitari-Kauppi, M. Kelokaski, M. Voutilainen, M. Myllys, T. Turpeinen, J. Timonen, F. Mateos, and M. Montoto. Characterizing low-permeable granitic rock from micrometer to centimeter scale: X-ray microcomputed tomography, confocal laser scanning microscopy and 14c-pmma method. In *Symposium NN - Scientific Basis for Nuclear Waste Management XXX*, volume 985 of *MRS Proceedings*, 2006.

[218] J. Sijbers and A. Postnov. Compensation of ring artefacts insynchrotron tomographic images. *Phys. Med. Biol.*, 2004.

[219] S. Siltanen, V. Kolehmainen, S. Järvenpää, J. P. Kaipio, P. Koistinen, M. Lassas, J. Pirttilä, and E. Somersalo. Statistical inversion for medical x-ray tomography with few radiographs: I. general theory. *Physics in Medicine and Biology*, 48(10):1437–1463, May 2003.

[220] G. D. Smith. *Numerical Solution of Partial Differential Equations: Finite Difference Methods (Oxford Applied Mathematics & Computing Science Series)*. Oxford University Press, USA, 1986.

[221] O. K. Smith. Eigenvalues of a symmetric 3×3 matrix. *Communications of the ACM*, 1961.

[222] S. M. Smith. Susan – a new approach to low level image processing. Technical report, Oxford Centre for Functional Magnetic Resonance Imaging of the Brain (FMRIB), 1995.

[223] S. W. Smith. *The Scientist & Engineer's Guide to Digital Signal Processing*. California Technical Pub, 1997.

[224] M. Sofka and C. V. Stewart. Retinal vessel centerline extraction using multiscale matched filters, confidence and edge measures. *IEEE Transactions on Medical Imaging*, 2006.

[225] J. P. Steffen and T. Fröba. Reducing the focal spot shift of microfocus x-ray tubes to increase the accuracy of CT-based dimensional measurement. In *DIR 2011 - X-ray Sources*. International Symposium on Digital Industrial Radiology and Computed Tomography, 2011.

[226] S. R. Sternberg. Biomedical image processing. *Computer*, 16(1):22–34, January 1983.

[227] S. R. Stock. *MicroComputed Tomography: Methodology and Applications*. CRC Press, 2008.

[228] C. Sun. Fast optical flow using 3D shortest path techniques. *Image and Vision Computing*, 20(13-14):981–991, Dec 2002.

[229] S. Svensson and M. Aronsson. Using distance transform based algorithms for extracting measures of the fiber network in volume images of paper. *IEEE Trans. Syst., Man, Cybern. B*, 33(4):562–571, Aug 2003.

[230] S. Svensson and G. Borgefors. Digital distance transforms in 3D images using information from neighbourhoods up to 5×5×5. *Computer Vision and Image Understanding*, 88(1):24–53, Oct 2002.

[231] P. Tafforeau, R. Boistel, E. Boller, A. Bravin, M. Brunet, Y. Chaimanee, P. Cloetens, M. Feist, J. Hoszowska, J.-J. Jaeger, R.F. Kay, V. Lazzari, L. Marivaux, A. Nel, C. Nemoz, X. Thibault, P. Vignaud, and S. Zabler. Applications of x-ray synchrotron microtomography for non-destructive 3D studies of paleontological specimens. *Applied Physics A*, 83(2):195–202, 2006.

[232] Andor Technology. X-ray CCD detectors, 2002.

[233] T. Thüring, M. Abis, Z. Wang, C. David, and M. Stampanoni. X-ray phase-contrast imaging at 100 keV on a conventional source. *Scientific Reports*, 4, Jun 2014.

[234] C. Tomasi and R. Manduchi. Bilateral filtering for gray and color images. In *Computer Vision, 1998. Sixth International Conference on*, pages 839–846, 1998.

[235] T. Topolinski, A. Cichanski, A. Mazurkiewicz, and K. Nowicki. The relationship between trabecular bone structure modeling methods and the elastic modulus as calculated by FEM. *ScientificWorldJournal*, 2012.

[236] E. L. Trong, O. Rozenbaum, J. Rouet, and A. Bruand. A simple methodology to segment x-ray tomographic images of a multiphasic building stone. *Image Anal Stereol*, 27(3):175–182, Nov 2008.

[237] W. Tsai. Moment-preserving thresolding: A new approach. *Computer Vision, Graphics, and Image Processing*, 29(3):377–393, Mar 1985.

[238] C. Tsiotsios and M. Petrou. On the choice of the parameters for anisotropic diffusion in image processing. *Pattern Recognition*, 46(5):1369–1381, May 2013.

[239] H. Turbell. *Cone-Beam Reconstruction Using Filtered Backprojection*. PhD thesis, Linköping University, 2001.

[240] T. Turpeinen, A. Lähteelä, M. Myllys, M. Kataja, and J. Timonen. Computerized tomographic imaging of paper coating layers. In *Proceedings of 22nd coating Symposium*, 2005.

[241] T. Turpeinen, M. Myllys, P. Kekälainen, and J. Timonen. Interface detection using a quenched-noise version of the edwards-wilkinson equation. *IEEE Trans. on Image Process.*, 2015.

[242] T. Turpeinen, M. Myllys, V. Koivu, K. Mattila, M. Kataja, and J. Timonen. Structure and transport properties of fibre material based on micro-tomographic and nano-tomographic imaging. In *Abstract book of 2nd Conference on 3D-Imaging of Materials and Systems*, 2010.

[243] T. Turpeinen, M. Myllys, V. Koivu, K. Mattila, M. Kataja, and J. Timonen. Structure and transport properties of fibre material based on micro-tomographic and nano-tomographic imaging. In *Abstract book of Skyscan user meeting*, 2011.

[244] T. Turpeinen, S. Svensson, C. Östlund, J. Hyväluoma, and J. Timonen. Using image analysis to model 3d liquid-paper interaction. In *in Proceedings of Progress in Paper Physics*, 2008.

[245] H. K. Tuy. An inversion formula for cone-beam reconstruction. *SIAM Journal on Applied Mathematics*, 43(3):546–552, Jun 1983.

[246] D. Ushizima, D. Parkinson, P. Nico, J. Ajo-Franklin, A. MacDowell, B. Kocar, W. Bethel, and J. Sethian. *Statistical segmentation and porosity quantification of 3D x-ray microtomography*, pages 813502–813502–14. SPIE - International Society for Optical Engineering, Sep 2011.

[247] A. Vagnon, J. P. Riviare, J. M. Missiaen, D. Bellet, M. Di Michiel, C. Josserond, and D. Bouvard. 3D statistical analysis of a copper powder sintering observed in situ by synchrotron microtomography. *Acta Materialia*, 56(5):1084–1093, 2008.

[248] E. Van de Casteele, D Van Dyck, J. Sijbers, and E. Raman. A model-based correction method for beam hardening artefacts in x-ray microtomography. *J. X-Ray Sci. Technol.*, 2004.

[249] G. M. P. Van Kempen, N. van den Brink, L. J. van Vliet, M. Van Ginkel, P. W. Verbeek, and H Blonk. The application of a local dimensionality estimator to the analysis of 3-d microscopic network structures. In *in: SCIA 99, Proceedings of the 11th Scandinavian Conference on Image Analysis (Kangerlussuaq*, pages 447–455, 1999.

[250] L. J. van Vliet and F. G. A. Faas. Multi-orientation analysis by decomposing the structure tensor and clustering. *18th International Conference on Pattern Recognition (ICPR 2006)*, 2006.

[251] N. Vanderesse, É. Maire, A. Chabod, and J.-Y. Buffière. Microtomographic study and finite element analysis of the porosity harmfulness in a cast aluminium alloy. *International Journal of Fatigue*, 33(12):1514–1525, 2011.

[252] A. R. Videla, C. L. Lin, and J. D. Miller. 3D characterization of individual multiphase particles in packed particle beds by x-ray microtomography (xmt). *International Journal of Mineral Processing*, 84(14):321–326, 2007. Special Issue To Honor The Late Professor R. Peter King.

[253] L. Vincent. Morphological grayscale reconstruction in image analysis: applications and efficient algorithms. *IEEE Transactions on Image Processing*, 2(2):176–201, Apr 1993.

[254] L. Vincent and P. Soille. Watersheds in digital spaces: an efficient algorithm based on immersion simulations. *IEEE Transactions on Pattern Analysis and Machine Intelligence*, 13(6):583–598, Jun 1991.

[255] P. Viot, E. Plougonven, and D. Bernard. Microtomography on polypropylene foam under dynamic loading: 3D analysis of bead morphology evolution. *Composites Part A: Applied Science and Manufacturing*, 39(8):1266–1281, 2008. Full-field Measurements in Composites Testing and Analysis.

[256] W. Wang, A.N. Kravchenko, A. J. M. Smucker, and M. L. Rivers. Comparison of image segmentation methods in simulated 2D and 3D microtomographic images of soil aggregates. *Geoderma*, 162(34):231–241, 2011.

[257] J. Weickert. *Anisotropic Diffusion In Image Processing*. B.G. Teubner, 1996.

[258] D. J. Wells. *Computer Concepts Basics*. Cram101, 2012.

[259] E. L. Wernersson, A. Brun, and C. L. Luengo Hendriks. Segmentation of wood fibres in 3D CT images using graph cuts. In *Proceedings of the 15th International Conference on Image Analysis and Processing*, ICIAP '09, pages 92–102, Berlin, Heidelberg, 2009. Springer-Verlag.

[260] D. Wildenschild and A. P. Sheppard. X-ray imaging and analysis techniques for quantifying pore-scale structure and processes in subsurface porous medium systems. *Advances in Water Resources*, 2012.

[261] W. Wilkins, T. E. Gureyev, D. Gao, A. Pogany, and A.W. Stevenson. Phase-contrast imaging using polychromatic hard x-rays. *Nature*, 384(2):335–338, 1996.

[262] O. Wirjadi. Survey of 3d image segmentation methods. Technical report, Fraunhofer ITWM, 2007.

[263] P. J. Withagen, F. C. A. Groen, and K. Schutte. CCD color camera characterization for image measurements. *IEEE Transactions on Instrumentation and Measurement*, 56(1):199–203, Feb 2007.

[264] D. J. Withey and Z. J. Koles. Three generations of medical image segmentation: Methods and available software. *International Journal of Bioelectromagnetism*, 9(2), 2007.

[265] A. Witkowska, A. Alibhai, C. Hughes, J. Price, K. Klisch, C. J. Sturrock, and C. S. Rutland. Computed tomography analysis of guinea pig bone: architecture, bone thickness and dimensions throughout development. *PeerJ*, 2, 2014.

[266] J. Wu, H. Duan, and Q Zhong. 3D image skeleton algorithms. *2011 IEEE International Conference on Anti-Counterfeiting, Security and Identification*, Jun 2011.

[267] X-ray lab. About CT, mar 2013.

[268] W. Xu, S. A. Amin, O. C. L. Haas, K. J. Burnham, and J. A. Mills. *Contour detection by using radial searching for CT images*. IEEE, April 2003.

[269] H. Yang. *A Geometric and Statistical Analysis of Fibrous Materials from Three-dimensional High Resolution Images*. State University of New York at Stony Brook, 2001.

[270] Q. Yang, N. Maass, M. Tian, M. Elter, I. Schasiepen, A. Maier, and Hornegger J. Multi-material beam hardening correction (mmbhc) in computed tomography . In *Proceedings of the 12th International Meeting on Fully Three-Dimensional Image Reconstruction in Radiology and Nuclear Medicine*, 2013.

[271] I. T. Young, J. J. Gerbrands, and L. J. van Vliet. *Fundamentals of Image Processing*. Delft University of Technology, 2.3 edition, 1995.

[272] Y. Zhang, H. Chan, B. Sahiner, J. Wei, M. M. Goodsitt, L. M. Hadjiiski, J. Ge, and C. Zhou. A comparative study of limited-angle cone-beam reconstruction methods for breast tomosynthesis. *Med. Phys.*, 33(10), 2006.

[273] S. Zhao, W. Jakob, S. Marschner, and K. Bala. Building volumetric appearance models of fabric using micro CT imaging. *Communications of the ACM*, 57(11):98–105, Oct 2014.

[274] T. Zuva, O. O. Olugbara, S. O. Ojo, and S. M. Ngwira. Image segmentation, available techniques, developments and open issues. *Canadian Journal on Image Processing and Computer Vision*, 2(3), March 2011.

APPENDIX 1 COMPUTATIONAL TESTS

Following c++ code

```
bool boolvariable = false;
cout << "Size of boolvariable: " <<
sizeof(boolvariable) << "bytes \n";
```

ran on a 64-bit windows 7 returns

```
Size of boolvariable: 1 bytes
```

meaning that the size of Boolean in C++ is 1 byte. This is true, for example, in Java and C++, where every variable needs to be addressable and the memory is divided into 8-bit (byte) sized blocks. Java documentation [176] states that the size of boolean ”isn’t something that is precisely defined,” meaning meaning that it can be something other than a 1-bit. However, Boolean data can be compressed efficiently, or a special image type can be defined using binary shifting and masking operations of for addressing individual bits in memory. For example, in C++:

```
void setBit(int x, int y, int z, bool value) {
     //Data is stored into 1-dimensional array, here
     //we find the index to given coordinates
    int coord = z*x_size*y_size + y*x_size + x;
    //This is the address to the correct byte
    int byteCoord = coord/8;
    //This is the bit index at the byte
    int bitIndex = (coord%8);

    //The assignment operations
    if (value) image[byteCoord] |= (1 << bitIndex);
    else image[byteCoord] &= ~(1 << bitIndex);
}
```

table 13 contains a comparison of the basic arithmetic operations for the four data types. It can be seen here that the division operation with the double type is significantly slower than the other types of operations.

TABLE 13 The time it took to perform 1000000000 rounds of given operations with different data types.

Data Type	Add./Subtr.	Div./Mult.
Integer	2062 ms	3859 ms
Short	2061 ms	3836 ms
Float	2089	3834
Double	2116	6012

APPENDIX 2 SEGMENTATION RESULTS FOR ALL DENOISING METHODS

TABLE 14 The percentage of voxels belonging to the contact area for all denoising methods.

AD	BF	DCT	Gaussian	Mean	Median	MS	VaWe
0,08	0,15	0,08	0,22	0,37	0,19	0,09	0,09

TABLE 15 The average thickness of the lead pieces analysed by local thickness transform for all denoising methods.

AD	BF	DCT	Gaussian	Mean	Median	MS	VaWe
705.4 µm	706.3 µm	706,8 µm	704,8 µm	702,8 µm	707,2 µm	700,6 µm	705,6 µm

TABLE 16 The number of individual graphite particles found for all denoising methods. The real number of particles (108) was determined manually.

AD	BF	DCT	Gaussian	Mean	Median	MS	VaWe
110	111	109	108	108	109	109	111

TABLE 17 The number of particles found using a watershed for particle separation.

AD	BF	DCT	Gaussian	Mean	Median	MS	VaWe
7816	18517	20017	7198	19876	22337	12012	57592

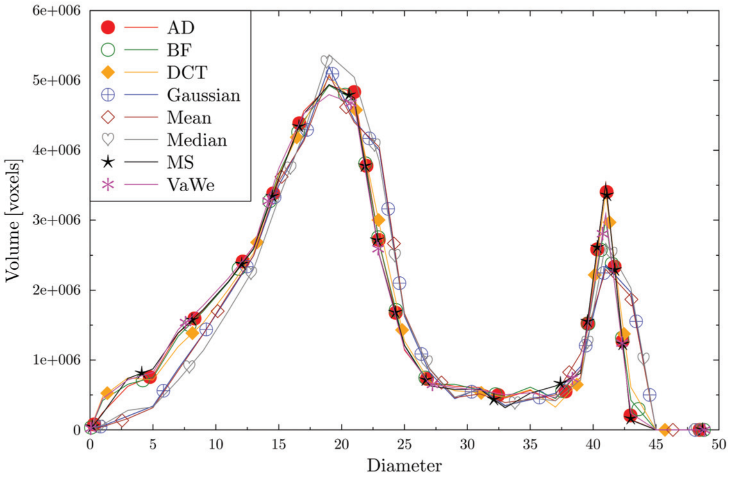

FIGURE 86 The volume of particles as a function of particle diameter.

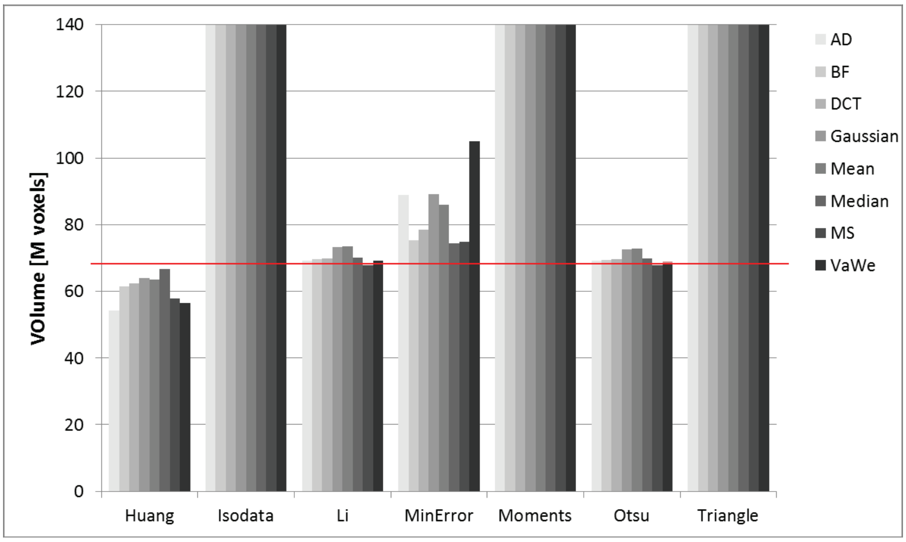

FIGURE 87 The volume determined using some automatic threshold selection methods for simple material from section 5.2.1. The red lines indicate the measured volume.

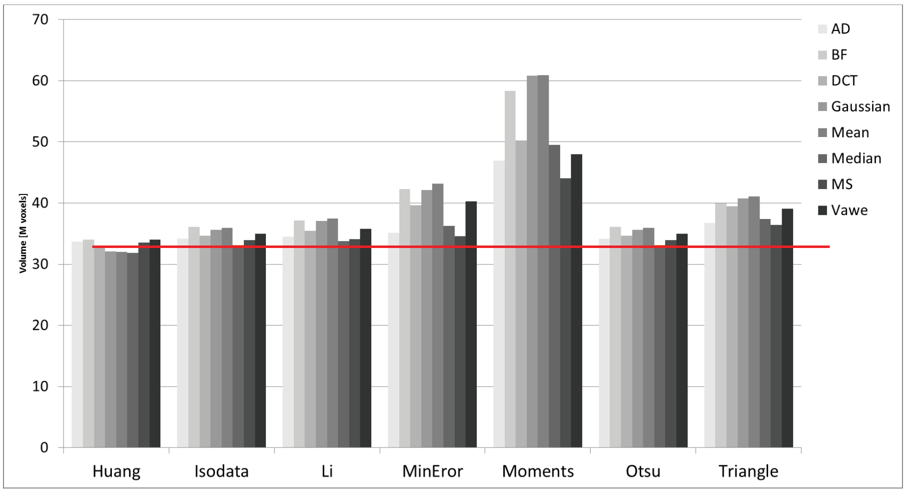

FIGURE 88 The volume determined using some automatic threshold selection methods for grainy material from section 5.2.1. The red lines indicate the measured volume.

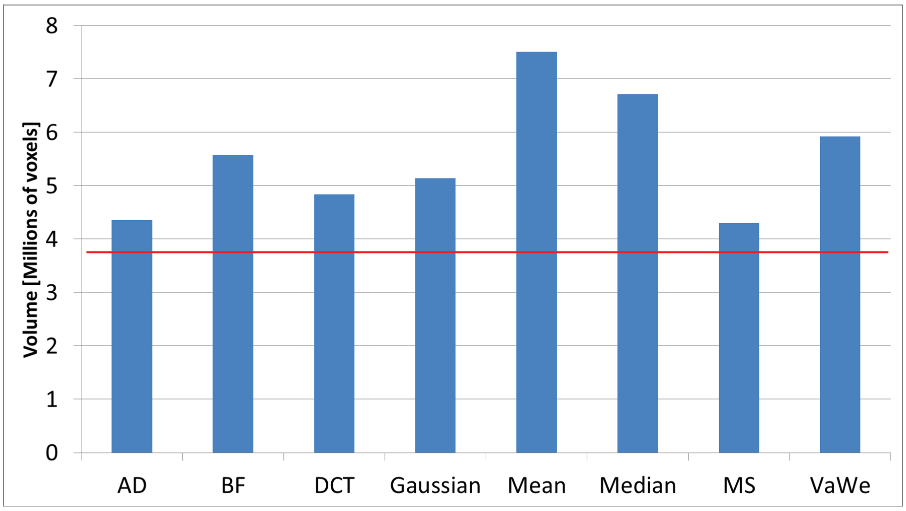

FIGURE 89 The volume graphite phase with different denoising methods for the multiphase sample.

TABLE 18 The volume of different materials in voxels, obtained from the labelled data and for all denoising methods.

Method	Measured	AD	BF	DCT	Gaussian	Mean	Median	MS	VaWe
Eraser	78731127	79977147	80097431	79957865	79474590	79384370	80037341	80066684	79946446
		101,6%	101,7%	101,6%	100,9%	100,8%	101,7%	101,7%	101,5%
Rubberband	15109399	14837686	14754959	14908909	15270660	15300550	14830590	14771824	14869336
		98,2%	97,7%	98,7%	101,1%	101,3%	98,2%	97,8%	98,4%
Graphite	4236882	4353979	5578354	4841576	5139303	7506863	6718069	4301361	5927249
		102,8%	131,7%	114,3%	121,3%	177,2%	158,6%	101,5%	139,9%